Low-mass Dark Matter search with the XENON100 experiment

Tiseni, A.

Publication date
2018

Document Version
Final published version

License
Other

[Link to publication](#)

Citation for published version (APA):
Tiseni, A. (2018). *Low-mass Dark Matter search with the XENON100 experiment*. [Thesis, fully internal, Universiteit van Amsterdam].

Andrea Tiseni

Low-mass Dark Matter search
with the xenon100 experiment

Low-mass Dark Matter search with the XENON100 experiment

Andrea Tiseni

Low-mass Dark Matter search with the XENON100 experiment

ACADEMISCH PROEFSCHRIFT

ter verkrijging van de graad van doctor
aan de Universiteit van Amsterdam
op gezag van de Rector Magnificus
Prof. dr. ir. K.I.J. Maex
ten overstaan van een door het College voor Promoties ingestelde commissie,
in het openbaar te verdedigen in de Aula der Universiteit
op vrijdag 12 januari 2018, te 13:00 uur

door

Andrea Tiseni

geboren te Loreto, Italië

Ai miei genitori

Contents

1

The Dark Matter evidence and the WIMP hypothesis

1.1 Introduction

The standard model of particle physics [1] describes elementary particles and their interactions. The discovery of the Higgs boson in 2012 by the ATLAS and CMS experiment at the Large Hadron Collider (LHC) [2] completes the standard model. However, we have at least two reasons to believe that this theory is incomplete. Indeed the standard model of particle physics is able to explain only 5% of the universe's mass and energy content, leaving the remaining 95% still to be explored. Dark Matter should account for 26% of the universe's mass and energy content while Dark Energy should account for 69%. Dark Energy is thought to be responsible for the accelerated expansion of the universe. Dark Matter is a hypothetical kind of matter that does not interact electromagnetically or strongly but its gravitational effect on the universe is visible. Its origin and its possible composition will be discussed in the following.

In this chapter we will describe the main experimental evidence for and properties of Dark Matter. Amongst the plethora of subatomic particles proposed to explain the Dark Matter content in our universe, one category stands out: the Weakly Interacting Massive Particle (WIMP), arising for instance naturally in supersymmetric extensions of the standard model of particle physics. We will also discuss two of the three methods to detect WIMPs namely the collider and indirect searches. In chapter 2 we will introduce the direct detection searches for WIMPs. If WIMPs interact through the weak interaction we can measure the recoil energy transferred to a nucleus. We will review the possible WIMP signatures and the current experimental results focusing on

the low-mass (below $20\,\mathrm{GeV}$) region. In chapter 3 we will describe the XENON100 experiment, a dual phase Time Projection Chamber (TPC) that we use to search for WIMPs. The main characteristics, the working principle, and the backgrounds will be described. In chapter 4 we will present the XENON100 Dark Matter results when relaxing the assumption that the backgrounds can be understood, modelled and subtracted. In this way, we will calculate the XENON100 results without background subtraction. Then, we will compare our results with the results published in [3] where it is assumed that the backgrounds can be modelled and subtracted. In chapter 5 we will describe a method that allows us to enhance the sensitivity of the XENON100 experiment for low-mass WIMPs. In this way we can verify (or falsify) the long standing DAMA/LIBRA claim of low-mass WIMP detection. The results were published in [4]. In the outlook we briefly reflect on the Dark Matter detection field focusing on the XENON1T experiment and the next-generation experiments.

1.2   The ΛCDM model

The ΛCDM model [5] - popularly known as the Big Bang model [6] - is used for the description of the origin and evolution of the universe. It provides a coherent explanation for plenty of experimental observations. Regarding the nomenclature, Λ stands for the cosmological constant associated with Dark Energy that is responsible for the accelerated expansion of the universe, DM stands for Dark Matter, the main topic of this thesis, and C stands for cold since this model assumes that Dark Matter particles are non-relativistic. The main ingredients of this model will be analyzed briefly in this section.

The ΛCDM model describes the universe from its very early phase, when the universe was in a very hot and dense state, to its current state with galaxies like the Milky Way (for a concise review see [7] and [8]). During this evolution the universe expanded and cooled down to a temperature - today - of about $2.7\,\mathrm{K}$. Fig. 1.1 shows a cartoon of the Big Bang model and highlights the key phases in the history of the universe:

- **Time $t < 10^{-12}\,\mathrm{s}$ (energy $E > 10^4\,\mathrm{GeV}$, temperature $T > 10^{17}\,\mathrm{K}$).**
  The lower energy bound is the current experimental energy reach of the Large Hadron Collider. Beyond this value experimental data is not available. Different theories attempt to describe the universe for $t < 10^{-12}\,\mathrm{s}$. The early phase of the universe, $t \simeq 10^{-44}\,\mathrm{s}$ ($E \simeq 10^{19}\,\mathrm{GeV}$, $T \simeq 10^{32}\,\mathrm{K}$), is called the Planck epoch. A coherent description of the Planck epoch will require a quantum theory of gravity, e.g. string theory. Around $t = 10^{-37}\,\mathrm{s}$ ($E \simeq 10^{15}\,\mathrm{GeV}$, $T \simeq 10^{28}\,\mathrm{K}$) the

strong interaction probably separated from the weak and electromagnetic interactions, according to grand unified theories [9]. After that the universe probably underwent an exponential expansion, called inflation [10].

- **$10^{-12} < t < 10^{-5}$ s ($10^{-1} < E < 10^4$ GeV, $10^{12} < T < 10^{17}$ K).**
  At $t \simeq 10^{-12}$ s ($E \simeq 10^4$ GeV, $T \simeq 10^{17}$ K) the electromagnetic interaction separates from the weak interaction: the Higgs field causes the electroweak symmetry breaking. This is a crucial moment in the history of the universe because all the standard model particles would be massless without the Higgs mechanism. However, the temperature is still too high to allow quarks to form hadrons. At $t \simeq 10^{-10}$ s ($E \simeq 10^2$ GeV, $T \simeq 10^{15}$ K), Dark Matter particles probably decouple from standard model particles. Under the assumption that Dark Matter is a WIMP, we will see that the number of WIMPs remained approximately constant in the universe after this moment (see section 1.4.2).

- **$10^{-5} < t < 10^2$ s ($10^{-4} < E < 10^{-1}$ GeV, $10^9 < T < 10^{12}$ K).**
  At $t \simeq 10^{-5}$ s ($E \simeq 10^{-1}$ GeV, $T \simeq 10^{12}$ K) the universe is sufficiently cool such that protons and neutrons can form, while the temperature is still high enough to maintain chemical equilibrium between protons and neutrons. After $t \simeq 1$ s ($E \simeq 1$ MeV, $T \simeq 10^{10}$ K), the universe has cooled down enough to allow the decoupling of neutrinos from the other standard model particles. As a result, protons and neutrons are not in equilibrium anymore, and the universe becomes transparent to neutrinos [7]. At $t \simeq 100$ s ($E \simeq 0.1$ MeV, $T \simeq 10^9$ K) nuclei such as ^{2}D, ^{3}He, ^{4}He and ^{7}Li are formed without being photo-dissociated [8].

- **10^2 s $< t < 3 \times 10^5$ y ($3 \times 10^{-10} < E < 10^{-4}$ GeV, $3 \times 10^3 < T < 10^9$ K).**
  The universe continued to cool down but neutral atoms were not formed as long as the energy/temperature was above the ionization energy of the hydrogen atom (13.6 eV). When the universe reached this energy/temperature - about 380.000 years after the Big Bang - the negatively charged electrons and the positively charged nuclei combined to form neutral atoms, and as a result photons decoupled from matter. Because the universe continued to expand since the decoupling, these photons are observable today at a temperature of only 2.725 K [11]. This relic thermal radiation is called the cosmic microwave background (CMB), and it was observed for the first time in 1965 disproving the steady state theory of the universe [12].

- $3 \times 10^5 < t < 10^{10}$ y $(2.3 \times 10^{-13} < E < 3 \times 10^{-10}$ GeV, $2.7 < T < 3.000$ K).
  The time between recombination and the formation of the first objects (galaxies, stars) is called the dark age of the universe. The 21 cm line of hydrogen molecules is the only radiation emitted in this period since photons do not have enough energy to ionize atoms. For $t > 1.5 \times 10^8$ y (re-ionization epoch), objects were energetic enough to radiate photons able to re-ionize hydrogen atoms. Other galaxies began their formation in this period with smaller structures forming before the bigger ones. The solar system began its formation 4.6×10^9 y ago and Homo Sapiens made its appearance about 200.000 years ago.
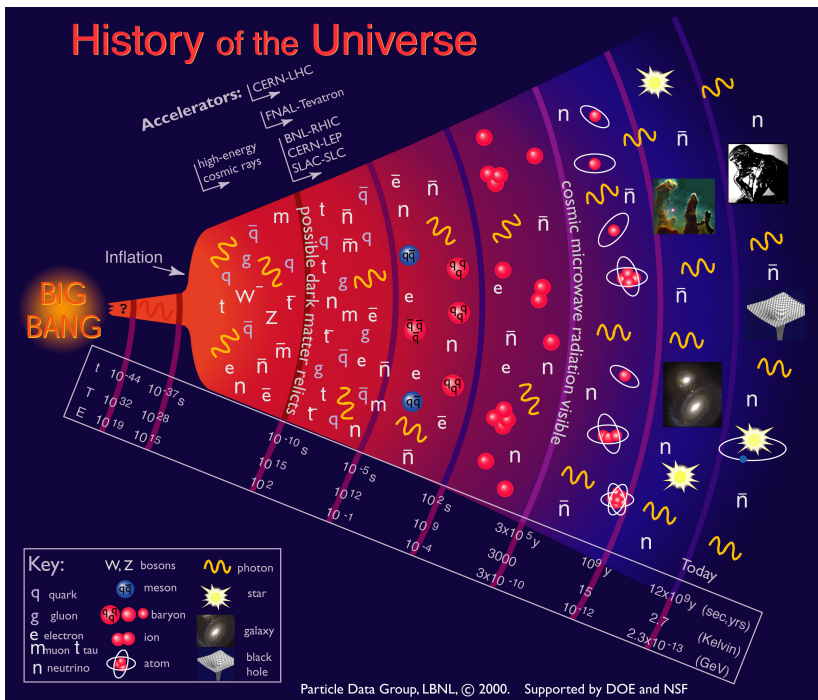
Figure 1.1: *Timeline of the universe, from its origin to the present day. Figure from [13].*

The Big Bang model is the foundation for the ΛCDM model together with the following principles:

1. **The cosmological principle:** the matter distribution is isotropic and homogeneous if we look at the universe on a large scale. The universe looks the same to any observer at any location.

2. **The equivalence principle:** the equivalence between gravitational and inertial mass. This principle is the foundation of the theory of general relativity.

The cosmological principle and Einstein's field equation [14] lead to the Friedmann – Lemaitre – Robertson metric [15] for the description of the universe:

$$ds^2 = -dt^2 + a^2 \left[\frac{dr^2}{1 - kr^2} + r^2(d\theta^2 + \sin^2\theta d\phi^2) \right]. \qquad (1.1)$$

Where ds^2 is the invariant element, t is time, a is the time-dependent scale factor of the universe, r, θ, ϕ, are polar coordinates, which are adjusted in order that k, the curvature of the universe, takes the values 0, -1, or +1 for a flat, open, or closed space. Using this choice of k, r is unitless, and a has dimension of length. Describing the universe as a perfect fluid, the combination of the metric equation (1.1) and Einstein's field equation [14] gives the Friedmann equation [16]:

$$H^2 \equiv (\frac{\dot{a}}{a})^2 = \frac{8\pi G}{3}\rho - \frac{k}{a^2}. \qquad (1.2)$$

Where ρ is the density of the fluid, H is the Hubble parameter, G is the gravitational constant and the dots are used for time derivatives.

Before going into the interpretation of the Friedmann equation, it should be noted that the universe can expand in an accelerated, decelerated or steady way, and this changes the density ρ in equation 1.2. In 1999 two different studies found that the expansion was accelerated, analyzing data from type Ia supernovae [17] [18]. These supernovae have similar masses and their light curves (luminosity as a function of the time after the explosion) are well known, so they serve as standard candles. In this way we can calculate the distance from the observed luminosities. The redshift can be measured independently and from the red shift we can calculate the scale factor of the universe at the time when the supernova exploded. Using both the redshift and the distance of the supernova, the experimental observations support the hypothesis of an accelerated expansion of the universe.

Another method to asses the accelerated expansion of the universe is the measurement of the size of objects. This method is often referred to as a standard ruler in analogy to the supernovae measurements (standard candles). Before the decoupling of photons, small initial perturbations in the gravitational potential of CMB caused oscillation in the photon-baryon fluid, called baryon acoustic oscillation (BAO). These led to anisotropies in the clustering of matter and galaxies at present days. The expected signature is an excess of galaxies separated by a characteristic length scale (500 million light-years). This length scale constitutes a standard ruler, which allows the measurement of the distance. These measurements were performed by the Sloan Digital Sky

Survey [19], and they are in agreement with an accelerated expansion of the universe. The initial perturbations in the photon-baryon fluid also led to anisotropies in the CMB temperature measured today (see section 1.3.3). The anisotropies in the CMB temperature constitute another verification of the accelerated expansion of the universe, giving rise to a cosmological constant (Λ) into the Einstein's field equation.
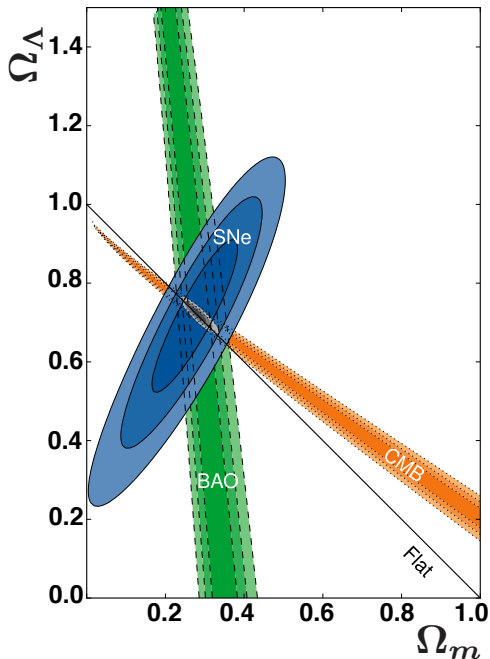
Figure 1.2: *The density parameter of Dark Energy (Ω_Λ) versus the density parameter of matter (Dark Matter + baryonic matter, Ω_m). The blue contours indicate the parameter space allowed by the supernovae measurements (SNe). The orange contours indicate the parameter space allowed by the cosmic microwave background measurements (CMB). The green contours indicate the parameter space allowed by baryon acoustic oscillation measurements (BAO). Figure from [20].*

The Friedmann equation can be used to describe the accelerated expansion of the universe considering an isotropic and homogeneous space. We introduce the definition of critical density ρ_c, that can be calculated from equation 1.2 under the condition of a flat universe ($k = 0$):

$$\rho_c = \frac{3H^2}{8\pi G}.$$
(1.3)

Using this critical density, we can introduce the density parameter Ω, defined as $\Omega = \dfrac{\rho}{\rho_c}$.

In this way equation 1.2 can be written as [16]:

$$\Omega \equiv \frac{\rho}{\rho_c} \equiv \Omega_R + \Omega_m + \Omega_\Lambda = 1 + \frac{k}{a^2 H^2} \, . \tag{1.4}$$

Where the different Ω_i are the contributions to the density of the universe: Ω_R is the radiation component ($\Omega_R \simeq 10^{-4}$ at present time), Ω_m is the density parameter of the matter and Ω_Λ is the density parameter of the cosmological constant. Experimental observations [21] [11] indicate that we live in a nearly flat universe with $k \simeq 0$ and $\Omega \simeq 1$. Under the assumption of a flat universe Fig. 1.2 shows the experimental allowed regions for Ω_Λ and Ω_m based on constraints from supernovae, CMB and BAO. The results indicate that Ω_Λ accounts for about 69% of the universe's mass and energy content while Ω_m accounts for the remaining 31%. Normal matter accounts only for 5%. The remaining 26% goes under the name of Dark Matter, a form of matter that does not interact through the electromagnetic and the strong nuclear forces.

1.3 Astrophysical evidence for Dark Matter

In this section the astrophysical evidence that supports the Dark Matter hypothesis is presented. Dark Matter does not emit light but from astronomical observations like the rotation curves of spiral galaxies, the dynamics of the galaxy clusters, the gravitational lensing of light and the temperature power spectrum of the cosmic microwave background we conclude that there must be Dark Matter.

1.3.1 Rotation curves and gravitationally bound systems

The rotation curve of a galaxy is a measurement of the velocities of stars and gas in the galaxy as a function of the distance from the galactic center. From classical mechanics, balancing the centripetal and the gravitational force, one would expect a velocity $v(r)$ given by:

$$v(r) = \sqrt{\frac{GM(r)}{r}} \, . \tag{1.5}$$

Where G is the gravitational constant, r is the distance and $M(r) = \int_V \rho(r) dV$ is the mass contained within a sphere of volume V for a mass density $\rho(r)$.

Most of the visible matter in a galaxy is contained within a certain radius (about 3-4 kpc for the M33 galaxy, which is shown in Fig. 1.3). As long as the star or gas is inside this radius, the velocity increases, while beyond this radius it should decrease as $r^{-1/2}$, just like the velocities of planets in the solar system, where the Sun constitutes about 99.9% of the total mass. In 1970 Rubin et al. [22] studied the rotation curve

of the Andromeda galaxy. The velocity profile is measured using the red shift of the 21 cm emission line of hydrogen in the interstellar gas. The mass of a galaxy can be determined from the observed luminosity and the distance of the galaxy. Rubin et al. found a strong discrepancy from the expected rotation curve based on the observed mass: after an initial rise the velocity does not decrease as a function of the radius as shown for the M33 galaxy in Fig. 1.3.
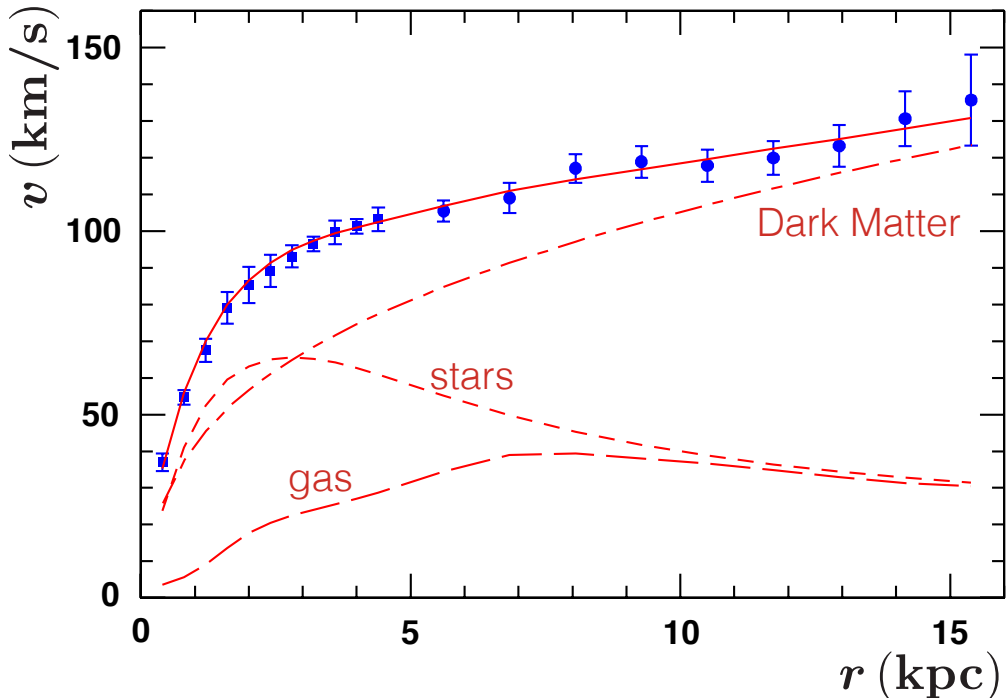
Figure 1.3: *Rotation curve of the M33 galaxy. The dots indicate the experimental measurements and the solid red line is the total fit considering the contribution to the velocity (v) of the gas (long dashed line), the stars (short dashed line) and Dark Matter (dashed dotted line). The contribution of Dark Matter can reconcile experiments with Newtonian dynamics. Figure from [23].*

One possible way to explain this discrepancy is to assume that the mass estimated from luminosity measurement is underestimated and that the majority of the mass in the galaxy does not emit light. If we assume that the galaxy is submerged in a large halo of invisible particles with a mass $M(r) \propto r$, the rotation curve can be reconciled with observations. Assuming spherical symmetry, the mass can be related to the mass

density as:

$$M(r) = 4\pi \int_0^r r'^2 \rho(r') dr', \tag{1.6}$$

and to have $M(r) \propto r$, we need a density $\rho(r) \propto r^{-2}$. We will use equation 1.6 to calculate the Dark Matter velocity distribution in section 1.4.1.

A second indication for the existence of Dark Matter comes from the study of the dynamics of galaxy clusters that is similar to the rotation curve method [24]. Stars move in galaxies and galaxies move in clusters and their orbital velocities are counterbalanced by the gravitational field. We assume that the galaxy cluster consists of N galaxies, and we define the average mass m and the average orbital velocity v. The total kinetic energy (E_k) is then given by:

$$E_k = \frac{1}{2} N m v^2, \tag{1.7}$$

while the gravitational energy (U), if the average separation between galaxies is R, is given by:

$$U \simeq -\frac{1}{2} N^2 \frac{G m^2}{R}. \tag{1.8}$$

From the virial theorem we have $E_k = -U/2$, and so:

$$M \equiv N m \simeq \frac{2 R v^2}{G}. \tag{1.9}$$

In 1933 Zwicky used the virial theorem to find evidence for Dark Matter while he was studying the Coma galaxy cluster. Zwicky calculated that the galaxies in this cluster were moving too fast according to the visible matter, inferring the existence of missing matter: the calculation indicated that the missing matter mass was about a factor 200 greater than the luminous matter mass [24]. In 1932 Jan Oort, a Dutch astronomer, had already arrived at the same conclusion [25].

1.3.2 Gravitational lensing

Gravitational lensing provides a method to measure the mass of objects: in the presence of a gravitational field, the light travels along a geodesic according to the theory of general relativity.

The Bullet Cluster (1E0657-56, Fig. 1.4) is an example of two clusters of galaxies, that underwent a collision $100\,\text{My}$ ago [26]. Assuming that Dark Matter is not present, the collision would cause the separation of the intracluster gas and of the stars of the galaxies. The stars of the galaxies are not largely affected by the collision, while the intracluster gas in the cluster is affected by friction. As a consequence, the gas heats up, and it emits X-ray. In this system the intracluster gas represents most of the baryonic

matter. If Dark Matter is present, it would not be affected by the collision and it would separate from the intracluster gas.

The light distortion of background galaxies caused by the cluster can be used to create a gravitational potential map [26]. The gravitational map would be different depending on the presence or the absence of Dark Matter. Without Dark Matter the gravitational potential map will trace the X-ray plasma being the dominant mass component as indicated in purple in Fig. 1.4. However, the measured gravitational potential map does not match the distribution of the X-ray plasma [26] as shown in blue in Fig. 1.4. This can be explained by invoking the existence of non electromagnetically interacting particles, Dark Matter, that are largely un-affected by the cluster collision.
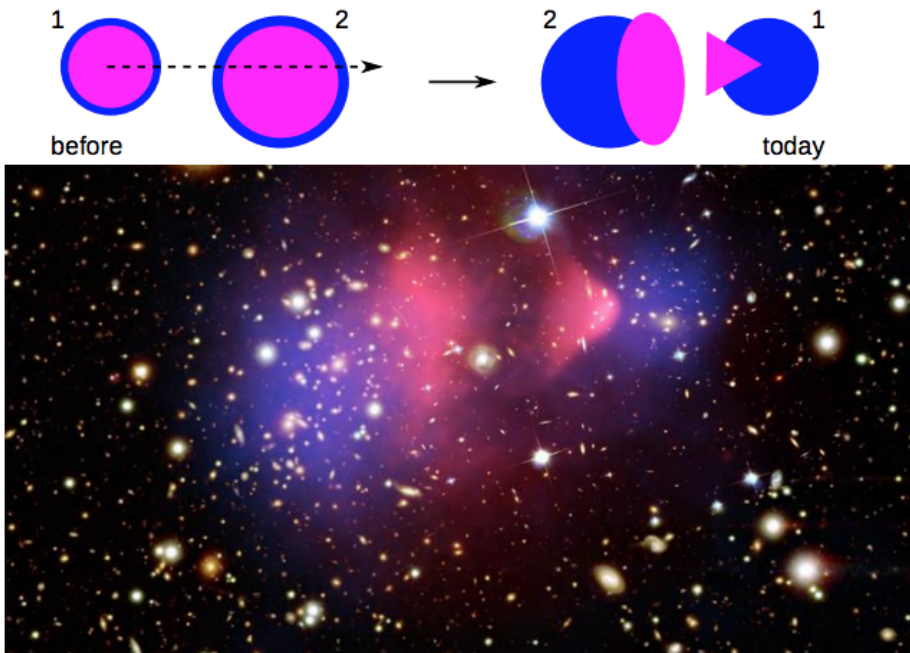
Figure 1.4: *Image of the system 1E0657-56 known as the Bullet Cluster. The X-ray emission of the plasma is shown in purple and does not match the mass distribution shown in blue. Besides the visible matter, another component - dubbed Dark Matter - is needed to explain this difference. The cartoon on top shows the passage of cluster 1 through cluster 2. Figure from [27].*

1.3.3   Cosmic microwave background

The radiation energy content of the universe is dominated by the cosmic microwave background (CMB), a relic of the Big Bang. The CMB radiation is almost perfectly isotropic, meaning that the energy (temperature) from each direction of the sky is the same (approximately $2.725\,$K). However, small temperature fluctuations of about $200\,\mu$K are observed (Fig 1.5).
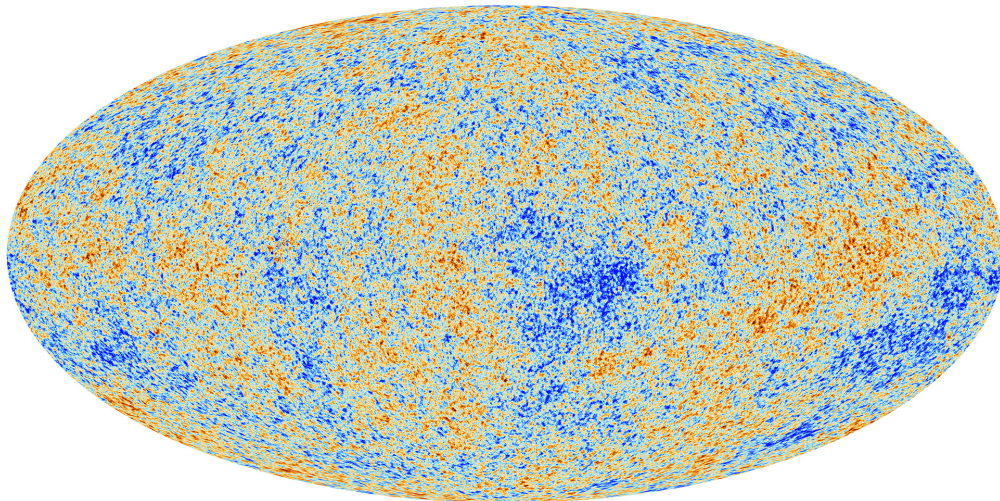
Figure 1.5: *A map of the temperature fluctuations from Planck data [11]. The colour differences show the temperature fluctuations: the red regions are 200 μK hotter than the blue regions. Figure from [28].*

Before inflation, random quantum fluctuations were probably present in the universe. Inflation probably caused these fluctuations to be amplified to cosmological distances. Therefore, after inflation, the universe was composed of regions with slightly different properties from each other, e.g. the density of matter was slightly higher in some regions compared to others. These small perturbations in the gravitational potential were steadily evolving while the universe was expanding. Before the atoms were formed, the proton-electron plasma was coupled to photons, forming the baryon-photon fluid. The gravitational perturbations were causing oscillation in this fluid, but, as long as photons were coupled to matter, their radiation pressure were counteracting these oscillations [29]. When the photons decoupled from the matter these perturbations were frozen-in, and they can be observed as temperature fluctuations today.

The temperature fluctuations are usually analyzed using a spherical harmonic ex-

pansion of the CMB sky [29]:

$$T(\theta, \phi) = \sum_{\ell m} a_{\ell m} Y_{\ell m}(\theta, \phi). \tag{1.10}$$

Where θ and ϕ are the polar coordinates and $Y_{\ell m}$ are the spherical harmonics with amplitudes $a_{\ell m}$. For example, $a_{00} = 2.725\,\mathrm{K}$ is the monopole component of the CMB and it corresponds to the mean temperature. Under the assumptions of a statistically isotropic sky (no preferred direction), and assuming that the temperature fluctuations are normally distributed, all the information about the temperature anisotropies can be extracted from the power spectrum. Fig. 1.6 shows the temperature power spectrum as measured by the Planck experiment [11].
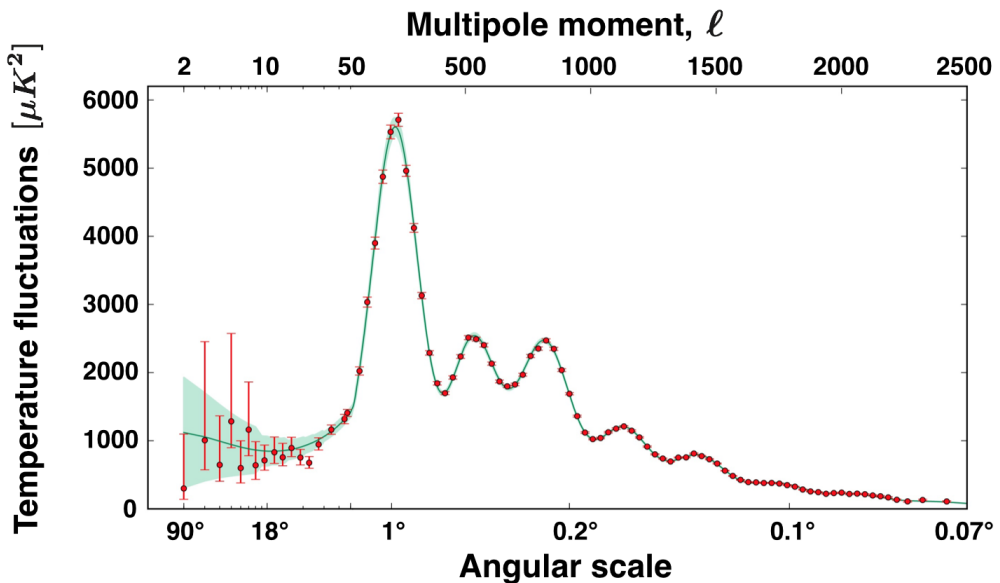
Figure 1.6: *The temperature power spectrum of the cosmic microwave background at different angular scales in the sky (bottom x-axis) and in terms of the multipole moment ℓ (top x-axis). The red dots are the measurements by Planck while the green line is the best fit based on the standard model of cosmology. Figure from [30].*

The three peaks are related to the density parameters (section 1.2) of Dark Energy, Dark Matter and normal matter, and to the curvature of the universe. Variations in these quantities change the absolute amplitude and the positions of the peaks. The ΛCDM model is used to fit the temperature power spectrum finding the best-fit density parameters that agree with the data [11] [31]: for Dark Energy $\Omega_\Lambda = 0.687 \pm 0.013$ for

Dark Matter we have $\Omega_{DM} = 0.264 \pm 0.011$ and $\Omega_m = 0.049 \pm 0.002$ for the standard model particles.

1.4 The WIMP hypothesis

Even though we can see its gravitational evidence, the nature of Dark Matter is still unknown. For the work presented throughout this thesis the Dark Matter is hypothesised to consist of yet to be identified elementary particles. These particles should have the following properties: they participate in the gravitational interaction, but not in the electromagnetic and strong interactions. Furthermore it is assumed that these particles participate in the weak interactions. We need a non-baryonic (no strong interaction) electrically neutral particle (no electromagnetic interaction), stable over the age of the universe and with the right abundance to reproduce the experimental evidence described above. None of the standard model particles have these properties except for neutrinos. However their density is insufficient to account for the observed Dark Matter. A general class of Dark Matter candidates that could explain the aforementioned gravitational effects in a coherent way is the Weakly Interactive Massive Particle (WIMP) [32]. Supersymmetric extensions to the standard model predict WIMPs with masses of around $100\,\mathrm{GeV}$ and with exactly the right properties to account for Dark Matter.

In this section we will focus on the standard halo model, on the thermal WIMP production and on the WIMP candidates. From now on we are going to assume that Dark Matter is made of WIMPs.

1.4.1 The WIMP Dark Matter halo

In section 1.3.1 it was shown that a Dark Matter density profile $\rho(r) \propto r^{-2}$ is needed to explain the experimentally observed rotation curves of spiral galaxies. In this section it will be shown, with a few assumptions, that WIMPs naturally have this required density profile. We will start assuming that Dark Matter consists of particles behaving like an ideal gas. In this case, we can relate the mean kinetic energy $< E_k >$ to the temperature, T, using:

$$< E_k >= \frac{1}{2}m_\chi < v^2 >= \frac{3}{2}k_b T, \tag{1.11}$$

and hence:

$$< v^2 >= \frac{3k_b T}{m_\chi}. \tag{1.12}$$

Where $<v^2>$ is the mean squared velocity, k_b is the Boltzmann constant and m_χ is the mass of the Dark Matter particle.

The next step is the derivation of the mass density profile as a function of the radial distance to the center of the spiral galaxy, $\rho(r)$. Starting from the ideal gas equation, we have:

$$PV = Nk_bT, \tag{1.13}$$

where P is the pressure and N is the number of Dark Matter particles in a volume V. Equation 1.13 can be re-written as:

$$P(r) = \rho(r)\frac{k_bT}{m_\chi}, \tag{1.14}$$

where we use $N/V = \rho(r)/m_\chi$. To calculate $\rho(r)$, we assume spherical symmetry, and that the collisionless gas is supported by hydrostatic pressure against the gravitational collapse, a condition called hydrostatic equilibrium.
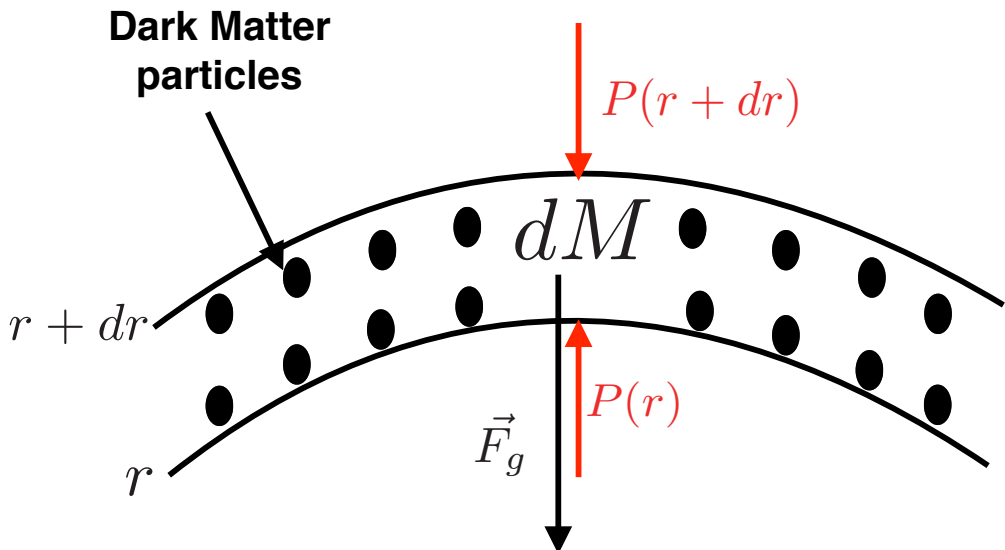
Figure 1.7: *Sketch of the hydrostatic equilibrium condition. The gravitational force ($\vec{F_g}$) is balanced by the force due to the hydrostatic pressure ($P(r)$). The forces are applied to a spherical shell with thickness dr and surface $4\pi r^2$.*

If we consider a spherical shell at radius r with thickness dr and hence an inner surface $4\pi r^2$ (Fig. 1.7), the mass dM contained in this shell is given by:

$$dM = \rho(r)4\pi r^2 dr. \tag{1.15}$$

The gravitational force ($\vec{F_g}$) on this shell can be expressed as:

$$\vec{F_g} = -\frac{GM(r)dM}{r^2}\hat{r} = -\rho(r)\frac{GM(r)}{r^2}4\pi r^2 dr\,\hat{r}, \tag{1.16}$$

where G is the gravitational constant, $\hat{r}$ is the unit vector in the radial direction, and $M(r)$ was introduced in equation 1.6. The net force ($\vec{F_p}$) on this spherical shell due to the pressure difference between the outer and the inner surfaces of the shell is given by:

$$\vec{F_p} = -\frac{dP}{dr}dr4\pi r^2\,\hat{r}. \tag{1.17}$$

In the case of equilibrium, the total force must be equal to zero:

$$\vec{F_p} + \vec{F_g} = \vec{0} \rightarrow \frac{dP}{dr} = -\rho(r)\frac{GM(r)}{r^2}\,. \tag{1.18}$$

Using equation 1.14, we can rewrite equation 1.18:

$$\frac{k_b T}{m_\chi}\frac{d\rho}{dr} = -\rho(r)\frac{GM(r)}{r^2}. \tag{1.19}$$

The solution of 1.19 is given by [33]:

$$\rho(r) = \frac{k_b T}{m_\chi}\frac{1}{r^2 2\pi G}\,. \tag{1.20}$$

This equation shows that $\rho(r) \propto r^{-2}$ follows from assuming spherical symmetry and an isotropic Dark Matter halo in hydrostatic equilibrium with gravity.

In the previous calculations we relate the density $\rho(r)$ to the ideal gas properties. In the following calculations we will relate the velocity from the rotation curves (see section 1.3.1, equation 1.5) to the ideal gas properties. Using equation 1.6 we can write:

$$\frac{dM(r)}{dr} = 4\pi r^2\rho(r), \tag{1.21}$$

hence, taking the derivative of both sides of equation 1.5, we have:

$$2v(r)\frac{dv(r)}{dr}r + v^2(r) = G\frac{dM(r)}{dr}, \tag{1.22}$$

and using equation 1.21 we can write:

$$2v(r)\frac{dv(r)}{dr}r + v^2(r) = G4\pi r^2\rho(r), \tag{1.23}$$

If we consider the Milky Way's rotation curve, a very good approximation is to consider that, at the Sun's distance, we are in the flat region of the rotation curve (Fig. 1.3).

This means that the speed has reached a constant value ($v(r) = v_0 \simeq 220\,\text{km/s}$). Therefore, we have $\dfrac{dv(r)}{dr} = 0$, and equation 1.23 can be written as:

$$\rho(r) = \frac{v_0^2}{4\pi G}\frac{1}{r^2}.$$
(1.24)

Using equations 1.20 and 1.24, we can derive the following equation that relates our ideal gas with the density profile from rotation curves:

$$\frac{k_b T}{m_\chi} = \frac{1}{2}v_0^2,$$
(1.25)

and we will use this equation to characterize the Dark Matter velocity distribution.

The final step is the calculation of the velocity distribution for the Dark Matter particles. If the Dark Matter halo of the galaxy is described as a single-component isothermal sphere, the velocity distribution is a Maxwellian [33], which can be expressed as:

$$f(v) = \left(\frac{1}{\sqrt{2\pi\sigma^2}}\right)^3 e^{-\frac{v^2}{2\sigma^2}}.$$
(1.26)

In this equation v is the velocity, σ is the velocity dispersion and the term within round brackets is the normalization constant. The mean squared velocity of the Maxwellian is given by:

$$<v^2> = \int_0^\infty v^2 4\pi v^2 f(v)dv = 3\sigma^2.$$
(1.27)

Equation 1.12 relates $<v^2>$ to the temperature and the mass. Using equation 1.27 we can write:

$$\sigma^2 = \frac{k_b T}{m_\chi},$$
(1.28)

and using equation 1.25 we obtain:

$$\sigma^2 = \frac{1}{2}v_0^2.$$
(1.29)

Therefore, the Maxwellian distribution (equation 1.26) is rewritten as:

$$f(v) = \left(\frac{1}{\sqrt{\pi v_0^2}}\right)^3 e^{-\frac{v^2}{v_0^2}}.$$
(1.30)

Fig. 1.8 shows the differential number of WIMPs with velocity between $\vec{v}$ and $\vec{v} + d\vec{v}$, $dN = 4\pi v^2 f(v)dv$. The number of particles has a maximum for $v = v_0$, meaning that the most probable WIMP velocity is v_0.

Using the assumptions of this subsection, equation 1.30 gives us a model to describe the velocity distribution of the Dark Matter particles: the Maxwellian distribution. In chapter 2, we will use this distribution to calculate the Dark Matter interaction rate for direct detection experiments.
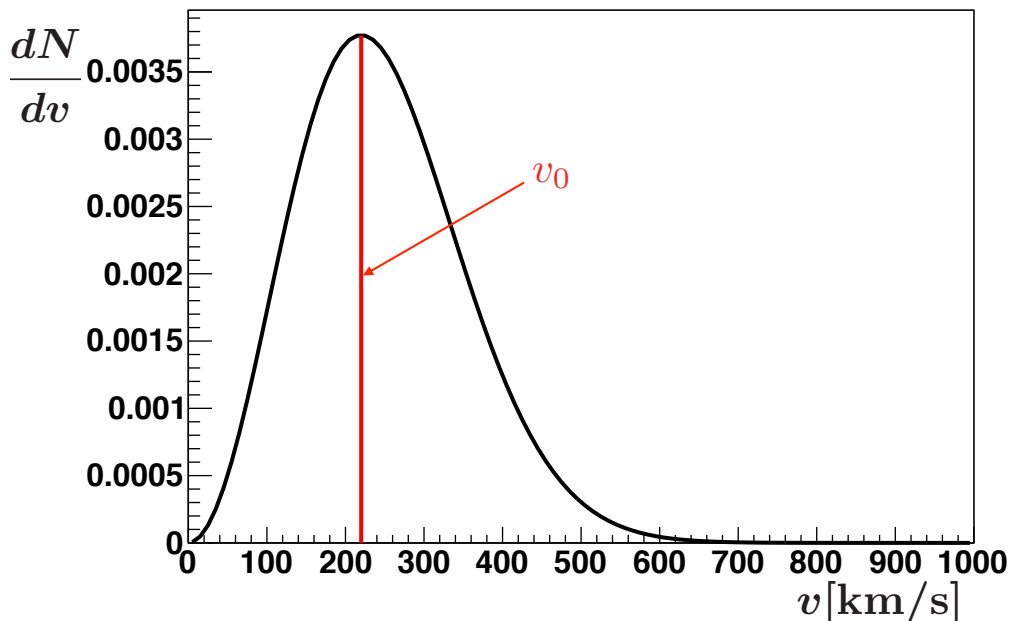
Figure 1.8: $dN/dv = 4\pi v^2 f(v)$, with $f(v)$ a Maxwellian. The most probable velocity ($v_0 = 220\,km/s$) is indicated.

1.4.2 WIMP production

In the early universe, WIMPs may be produced as a thermal relic of the Big Bang [34]. At the beginning, the universe is dense and sufficiently hot that WIMPs and standard model particles are in thermal and chemical equilibrium [35] [34]. Annihilation and creation of WIMPs is given by [35] [36]:

$$\chi\bar{\chi} \longleftrightarrow e^+e^-, \mu^+\mu^-, \tau^+\tau^-, q\bar{q}, W^+W^-, ZZ, HH, \nu\bar{\nu}.... \tag{1.31}$$
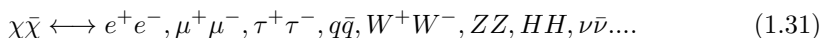
Where on the left hand side we have WIMPs (χ) and on the right hand side standard model particles.

So, as long as the temperature is larger than the WIMP mass, chemical and thermal equilibrium between standard model particles and WIMPs is maintained. For chemical equilibrium, the annihilation (Γ_{ann}) and the production rate (Γ_{cr}) is the same, and it is given by [35]:

$$\Gamma_{ann} = \Gamma_{cr} = <\sigma_{ann}v> n_\chi^{eq}. \tag{1.32}$$

Where n_χ^{eq} is the number density of WIMPs in chemical equilibrium and $<\sigma_{ann}v>$ is the thermally averaged annihilation cross section. However, the universe is expanding,

and the temperature is decreasing. As the universe cools down the number of produced WIMPs decreases because standard model particles do not have any longer sufficient energy to produce WIMPs. The number of produced WIMPs becomes exponentially suppressed dropping as $e^{-\frac{m_\chi}{k_b T}}$ [35] [34]. Since the universe is expanding, the number density of WIMPs also decreases. So, naively speaking, WIMPs cannot find each other anymore to annihilate. Therefore, the annihilation rate decreases. As a consequence of the expansion of the universe, both the production and the annihilation rate of WIMPs decrease. The net effect is that WIMPs freeze-out to a thermal relic density that is constant in a co-moving coordinate system [34] [36].

Under the assumption that the WIMP is its own antiparticle, the variation of the WIMP number density over time $(\frac{dn_\chi}{dt})$ is quantitatively described by the Boltzmann equation [36] [35]:

$$\frac{dn_\chi}{dt} + 3Hn_\chi = - <\sigma_{ann}v> ((n_\chi)^2 - (n_\chi^{eq})^2). \tag{1.33}$$

Where n_χ is the number density of WIMPs, H is the Hubble parameter (equation 1.2), t is the time, and the other terms were introduced in equation 1.32. On the right hand side the rate of WIMP annihilation per unit volume is expressed by $<\sigma_{ann}v> (n_\chi)^2$, while the rate of WIMP production per unit volume is expressed by $<\sigma_{ann}v> (n_\chi^{eq})^2$ [34]. On the left hand side, the term $3Hn_\chi$ expresses that the WIMP number density scales as the third power of the scale factor ($n_\chi \propto a^{-3}$): after the freeze-out the number of WIMPs is constant and the annihilation and production of WIMPs do not play a role anymore.

We define the comoving number density of WIMPs as the number density of WIMPs in a volume that expands at the same pace of the universe. This definition implies that the comoving number density is constant if the number of WIMPs does not change with time as it happens after the freeze-out. Fig. 1.9 shows the evolution of the comoving number density of WIMPs as a function of the energy/time. Initially, we see that the comoving number density decreases: standard model particles do not have enough energy to produce WIMPs. As the universe expanses, WIMPs do not annihilate anymore and their comoving number density stays constants.

The freeze-out condition is realised when the annihilation rate is roughly equal to the expansion rate of the universe. Using this condition, the density parameter of WIMPs can be approximated as [34]:

$$\Omega_\chi \simeq \frac{m_\chi T_0^3}{\rho_c M_{pl} T_f} (<\sigma_{ann}v>)^{-1} \simeq \frac{6 \times 10^{-27} cm^3 s^{-1}}{<\sigma_{ann}v>}. \tag{1.34}$$

Where m_χ is the WIMP mass, T_0 is the temperature at the present day, T_f is the temperature at the freeze-out, M_{pl} is the planck mass, and ρ_c is the critical density (equation 1.3). The literature often assumes $m_\chi/T_f \simeq 20$ [34]. Using equation 1.34, we can calculate a rough value for the thermally averaged annihilation cross section: to obtain $\Omega_\chi \simeq 0.3$, a thermally averaged annihilation cross section $< \sigma_{ann}v > \simeq 2 \times 10^{-26}$ cm^3 s^{-1} is necessary. This is approximately the thermally averaged annihilation cross section predicted by supersymmetric extension of the standard model, a fact that is often referred as the WIMP miracle. In Fig. 1.9 the freeze-out value depends on the thermally averaged cross section $< \sigma_{ann}v >$, as shown in equation 1.34: higher (lower) $< \sigma_{ann}v >$ values imply lower (higher) WIMP density values (Ω_χ).
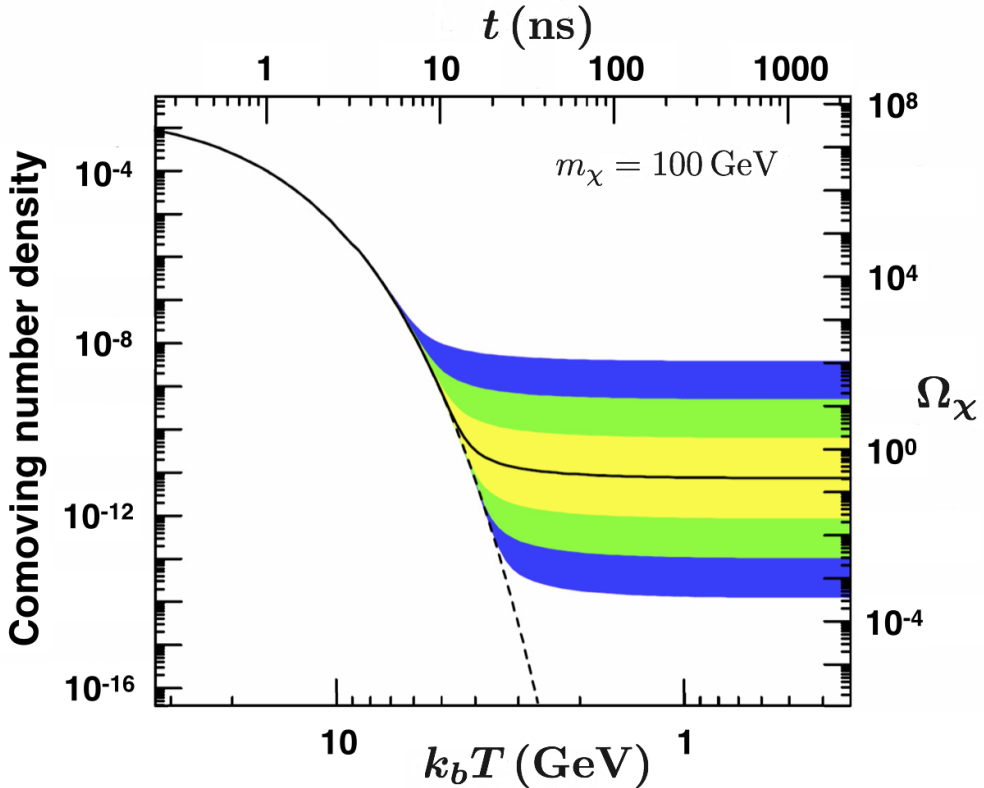
Figure 1.9: *WIMP comoving number density as a function of the temperature for a 100 GeV WIMP. The solid line indicates a WIMP with the right relic density. The coloured area shows a WIMP with a relic density a factor 10, 100, 1000 different from the required relic density. The dashed line indicates a WIMP that remains in thermal equilibrium. Figure from [34].*

1.4.3 WIMP candidates

WIMP candidates arise in theories beyond the standard model of particle physics which predicts particles with the properties described in section 1.4.2. These theories are able to explain the experimental evidence described in section 1.3. However, it should be noted that none of these particles have so far been observed in experiments. One of the extensions of the standard model is the supersymmetric theory (SUSY) [37] [35]. Even though a full description of SUSY theories is beyond the scope of this thesis, some of its basic concepts are explained.

SUSY introduces a new symmetry that relates bosons and fermions, and, as a consequence, some of the standard model problems can be solved, e.g. the so-called hierarchy problem [34]. The hierarchy problem affects the calculation of the Higgs boson mass. The quantum corrections ΔM_H^2 to the Higgs boson mass M_H are of the order of [34]:

$$\Delta M_H^2 = \frac{\lambda^2 \Lambda^2}{16\pi^2} \, . \tag{1.35}$$

Where λ is a dimensionless coupling and Λ is the energy scale above which the standard model is not anymore valid [34]. If $\Lambda \simeq M_{pl}$, where M_{pl} is the Planck mass, the correction to the Higgs mass becomes large. Instead, if $\Lambda \simeq 0.1$-10 TeV the hierarchy problem can be mitigated because the quantum corrections determined by supersymmetrical particles cancel out the standard model corrections. Supersymmetrical theories usually impose the conservation of a discrete symmetry called R-Parity which states that the total number of SUSY and standard model particles is conserved. Under this assumption the lightest supersymmetrical particle (LSP) cannot decay into standard model particles making the LSP a natural WIMP candidate because it is a non baryonic stable particle.

1.5 WIMP detection techniques

Assuming that the Dark Matter is a WIMP, it is possible to observe its coupling to standard model particles. Three possible processes are highlighted in Fig. 1.10:

1. **Collider searches:** the creation of WIMPs via the collision of standard model particles at colliders (section 1.5.1).

2. **Indirect searches:** the annihilation of WIMPs into standard model particles in relatively high-density Dark Matter regions in the universe (section 1.5.2).

3. **Direct searches:** the scattering of WIMPs with standard model particles, which is typically studied by extremely low-background experiments, and therefore located in deep-underground laboratories. This will be presented in chapter 2 as it is the subject of this thesis.
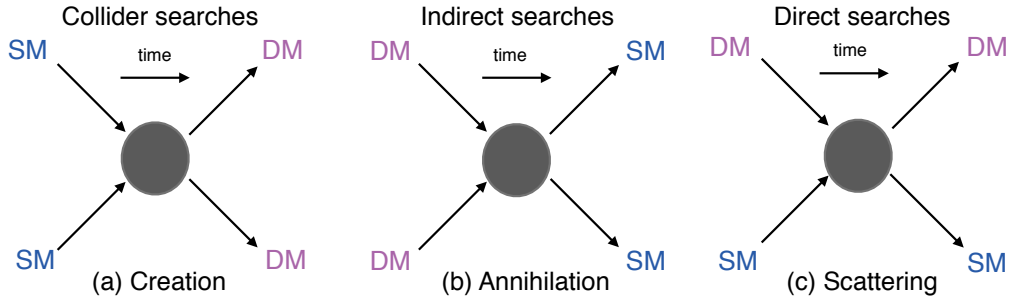
Figure 1.10: *Possible interaction processes for Dark Matter (DM) and standard model particles (SM).*

1.5.1 Collider searches

In collider experiments, WIMPs may be produced from standard model particle annihilation. Currently the most promising collider to achieve this goal is the Large Hadron Collider. Fig. 1.11 (a) shows an artist impression of the 27 km tunnel (about 150 m underground near Geneva) where protons collide with a center of mass energy up to 14 TeV. Fig. 1.11 (b) shows a potential way to produce WIMPs: an antiquark annihilates with a quark, and WIMPs are produced in the final state. The antiquark also radiates an object X, e.g. an hadronic jet [38], a photon [39], a Z [40], a H [41], a W [42], which interacts[1] in the detector and serves as a tag to identify the WIMP pair: these events will show missing transverse momentum measured with respect to the beam line because the WIMPs will leave no traces in the detector.

The transverse momentum of the object X can be measured. So, assuming that the WIMPs recoil against the object X, the WIMP missing energy can be inferred as well. Fig. 1.11 (c) shows a cartoon of the expected WIMP signature in this scenario: the distribution of the missing energy shows an excess compared to the standard model background. The ATLAS [43] and the CMS experiment [44] [45] did not find any evidence of WIMPs.

---

[1]The Z, H and, W bosons decay, and then the particles produced by the decay interact in the detector.
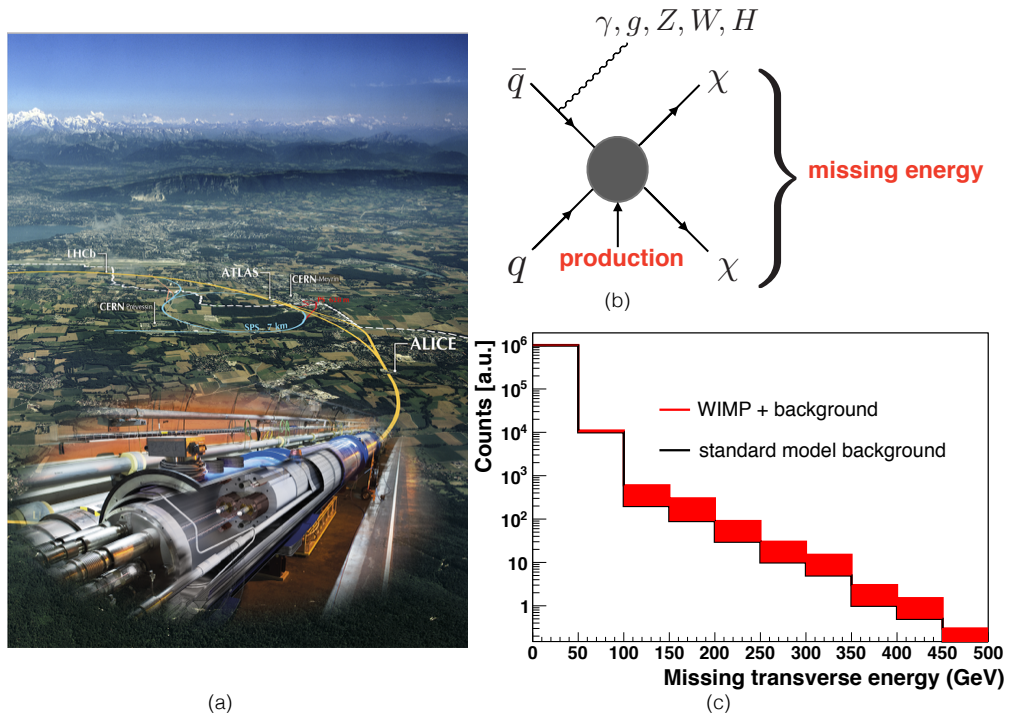
Figure 1.11: *(a) Artist view of the Large Hadron Collider. The ATLAS, LHCb and ALICE experiments are indicated. (b) Possible diagram of WIMP creation at the Large Hadron Collider. (c) Cartoon of the WIMP signature at colliders. The standard model background is given by the black line, while the tentative WIMP excess is given by the red shaded area.*

1.5.2 Indirect searches

In section 1.4.2 it was shown that the comoving number density of WIMPs is constant after the freeze-out. However, in the areas of the universe with higher density of Dark Matter, e.g. the stars or the galactic center, WIMP annihilation may still occur. For example, when WIMPs scatter off solar nuclei they can become gravitationally bound to the Sun. Once bound, WIMPs continue to lose energy becoming entrapped in the interior of the Sun and annihilating into standard model particles [46]. Of these particles, only neutrinos are able to escape from the star. Another possibility is that the annihilation of WIMPs takes place in the galactic center. In this case also an excess of γ-rays or antimatter particles could provide evidence for WIMPs. Therefore, WIMPs can be indirectly detected searching for particles produced from the WIMP annihilation in different ways, for example:

- **Enhancements in the neutrinos flux from the Sun.**
  WIMPs can scatter on nuclei in the Sun to become gravitationally bound if their velocity is thereby reduced below the solar escape velocity. Equilibrium can be established between the capture and the annihilation rate. WIMPs can annihilate directly into neutrinos or into standard model particles that might subsequently yield neutrinos as for example W, Z, b-quarks, τ and μ particles typically do [47]. Neutrinos can escape the Sun, and they can be detected on the Earth [47]. These searches are sensitive to the WIMP-proton spin-dependent cross section (section 2.2.2) that is responsible for the capture process in the Sun [48]. Neutrino searches are performed for example by IceCube [48] and Super-Kamiokande [49] and will be performed in the future by KM3NeT [50]. No evidence of WIMPs was found.

- **Enhancements in the γ-ray energy spectrum.**
  Due to energy-momentum conservation, the annihilating WIMPs can produce two back-to-back photons with energy $E_\gamma = m_\chi$, as shown in Fig. 1.12 (b). In this case the signature will be a mono energetic γ-ray line, as shown in Fig. 1.12 (c) where a hypothetical WIMP ($m_\chi = 300\,\text{GeV}$) excess in the γ-ray energy spectrum is illustrated. Another possibility is that the annihilation of WIMPs will produce standard model particles that might subsequently decay into photons, resulting in an enhancement over a continuous spectrum of energies. γ-ray searches are performed by, for example, the FERMI satellite experiment [51] (an artist impression of the FERMI satellite is shown in Fig. 1.12 (a)), and will be performed in the future by the ground-based CTA [52]. No conclusive evidence of WIMPs was found, although FERMI reported an enhancement in the gamma ray spectrum between 1-3 GeV that could be attributed to annihilation of a WIMP, but also to an underestimated background source.

- **Enhancements in the cosmic-ray antiparticle fluxes.**
  Cosmic-ray antiparticles like positrons and antiprotons are produced by the cosmic-ray spallation on the interstellar medium [35]. WIMPs can annihilate into standard model particles that can produce antiprotons and/or positrons. Therefore, WIMPs can cause an enhancement of the antiproton/positron flux compared to the cosmic-ray spallation contribution. No conclusive evidence of WIMPs was found, albeit intriguing results have been shown by the AMS experiment on the International Space Station.
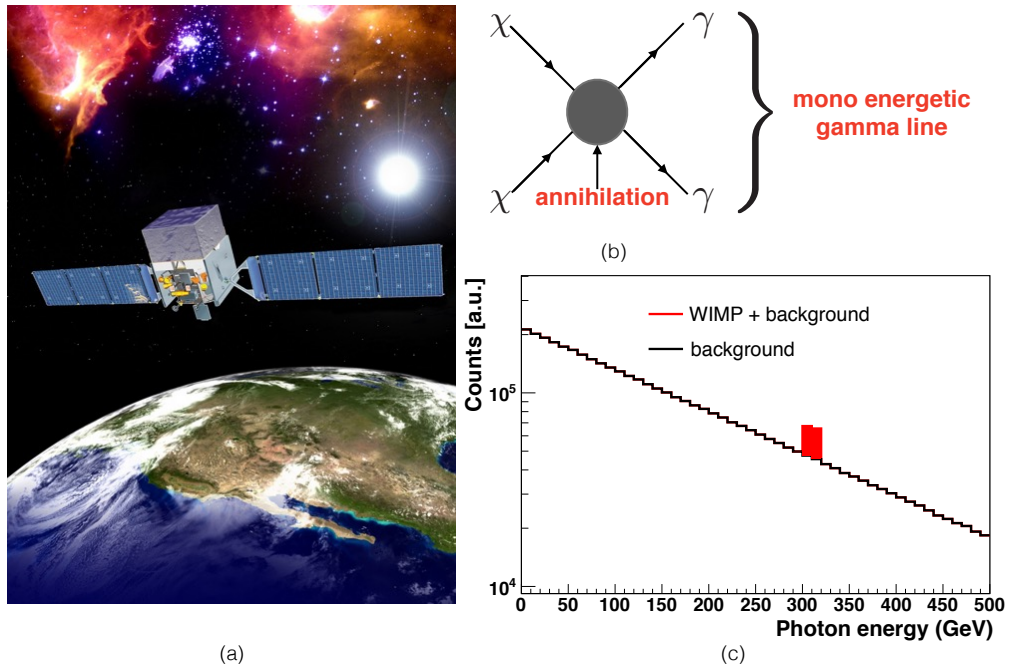
Figure 1.12: *(a) Artist impression of the FERMI satellite orbiting around the Earth. From [53]. (b) Possible diagram of WIMPs annihilation into two back-to-back photons. (c) Cartoon of a hypothetical excess in the γ-ray spectrum (black line) caused by a $300\,GeV$ WIMP annihilating into two back-to-back photons (red shaded area).*

1.6   Concluding remarks

In this chapter the main experimental evidence for Dark Matter was reviewed and discussed, and we postulated the existence of a Weakly Interactive Massive Particle (WIMP) to explain the observational data. We made two fundamental assumptions:

1. Dark Matter can be explained by a new massive subatomic particle.

2. This particle participates in gravity and in weak interaction and it does not have colour or electric charge.

Assuming the validity of the WIMP hypothesis, we could discover WIMP signatures in the direct, indirect and collider searches. Indirect and direct searches can prove that a WIMP particle constitutes also the Dark Matter content of the universe. For direct searches, if Dark Matter is made of WIMPs, about a billion of WIMPs should pass through our bodies every second. For indirect searches, WIMPs in the galactic center

can annihilate into standard model particles detectable on Earth. Collider searches can discover a new particle with the right properties to be a WIMP, but they will never be able to prove that this particle constitutes the Dark Matter content of the universe. However, the advantages of collider searches are that WIMPs are produced at the accelerators in a controlled laboratory environment and that the rates of the standard model processes, which constitute a background for WIMP searches, can be calculated from theory. Instead, the knowledge of astrophysical parameters, e.g. the local WIMP density for direct searches (section 2.1.2), is fundamental for the calculation of the Dark Matter rate in direct and indirect searches, and these parameters are often only known with large systematic uncertainty. Furthermore, the background estimation can be challenging in direct and indirect searches. If we will observe a WIMP in the next years we will need all the methods to compare and crosscheck the results. The discovery of WIMPs can be the next major milestone in particle physics after the gravitational waves and Higgs boson discoveries.

2

Direct Detection of Dark Matter

The aim of, so called, direct Dark Matter detection experiments is to discover Dark Matter through its interactions with standard model particles on Earth. If Dark Matter is constituted of WIMPs, there is a minute chance that a detectable scatter occurs. In this chapter we will describe the direct detection theory, and review the experimental techniques and the current status.

2.1 WIMP interactions with matter

To calculate the differential WIMP event rate, we need to understand the cross section and the kinematics of a WIMP-nucleus interaction. The WIMP-nucleus cross section will also be translated into a WIMP-nucleon cross section to allow comparison between experiments using different targets.

2.1.1 Kinematics of WIMP interactions

Here we consider the scattering of a WIMP with a nucleus. To calculate the recoil energy, we assume that:

- The scattering is elastic;

- The WIMP hits the nucleus with relative velocity $\vec{v}$ while neglecting the thermal motion of the nucleus. The laboratory frame is defined as the reference frame in which the target nucleus is at rest.

It was shown in section 1.4.1 that the expected WIMP velocity is of the order of hundreds of km/s, so a non-relativistic calculation will suffice.

Figure 2.1: *Sketch of the collision between a WIMP (χ) and a nucleus (N) in the laboratory frame (top) and in their center of mass frame (bottom).*

Fig. 2.1 shows a sketch of the collision between a WIMP and a nucleus in the laboratory frame and in their center of mass frame. In the center of mass frame, the initial momentum ($\vec{p}$) is expressed as:

$$\vec{p} = \frac{m_\chi m_N}{m_\chi + m_N}\vec{v} \equiv \mu\vec{v}. \tag{2.1}$$

Where m_χ is the WIMP mass, m_N is the nucleus mass, $\vec{v}$ is the WIMP velocity in the laboratory frame, and μ is the WIMP-nucleus reduced mass.

In the center of mass frame the WIMP and the nucleus are scattered over an angle θ. The momentum transfer is defined as $\vec{q} = \vec{k} - \vec{p}$, with $\vec{k}$ the momentum in the final state. Therefore, the square of the momentum transfer, $|\vec{q}|^2$, is given by:

$$|\vec{q}|^2 = |\vec{k}|^2 + |\vec{p}|^2 - 2|\vec{k}||\vec{p}|\cos\theta, \tag{2.2}$$

hence using equation 2.1 and $|\vec{k}| = |\vec{p}| = \mu v$, we find for $|\vec{q}|^2$:

$$|\vec{q}|^2 = 2\mu^2 v^2 (1 - \cos\theta). \tag{2.3}$$

Since $|\vec{q}|^2$ does not depend on the reference frame, the nucleus recoil energy (E_R) in the laboratory frame can be expressed as:

$$E_R = \frac{|\vec{q}|^2}{2m_N}. \tag{2.4}$$

Hence, using equation 2.3 we have:

$$E_R = \frac{\mu^2 v^2 (1 - \cos\theta)}{m_N}. \tag{2.5}$$

If we define r as:

$$r = \frac{4\mu^2}{m_\chi m_N}, \tag{2.6}$$

we can rewrite equation 2.5:

$$E_R = Er\frac{1 - \cos\theta}{2}. \tag{2.7}$$

Where E is the kinetic energy of the incoming WIMP, $E = \frac{1}{2}m_\chi v^2$.

We can observe that $0 < r \leq 1$ for every WIMP and nucleus mass. Using $m_\chi = 100\,\text{GeV}$, and $m_N = 122\,\text{GeV}$ (xenon nucleus mass) we obtain a value of r of about 1 from equation 2.6. Using equation 2.7, $v = v_0 = 220\,\text{km/s}$ and $m_\chi = 100\,\text{GeV}$ we can calculate the value of the recoil energy:

$$0 \leq E_R \leq Er \simeq 27\,\text{keV}. \tag{2.8}$$

Using the same numerical values as above, the momentum transfer can be calculated from equation 2.3:

$$0 \leq |\vec{q}| \leq 2\mu v \simeq 80\,\text{MeV}. \tag{2.9}$$

Hence, the shortest De Broglie wavelength (λ) for $q \approx 80$ MeV is given by:

$$\lambda = \frac{h}{q} \simeq 15\,\text{fm}. \tag{2.10}$$

Therefore, the momentum transfer is small enough that the corresponding De Broglie wavelength is larger than the size of most nuclei, meaning that the scatter between the nucleus and the WIMP is coherent.

It has to be noted that WIMPs could also scatter with electrons. Considering an electron at rest and neglecting its binding energy, we obtain a value of r of about 2×10^{-5} from equation 2.6. Therefore, the typical recoil energy for an electron is about $1\,\text{eV}$, which is far below the keV recoil energy of a WIMP-nucleus scattering, and below the threshold for most currently available detection techniques in particle physics [54]. Hence, we can safely ignore the WIMP-electron scattering process.

2.1.2 Derivation of the differential event rate

In this section we will calculate the differential WIMP interaction rate, $\dfrac{dR}{dE_R}$, as a function of the nucleus recoil energy E_R. We start assuming that WIMPs have a unique velocity v. In this case, the WIMP rate (R) normalized per gram of the target material is given by:

$$R = \frac{N_A}{A} \frac{\rho_\chi}{m_\chi} \sigma v = \frac{N_A}{A} \frac{\rho_\chi}{m_\chi} \sigma \sqrt{\frac{2E}{m_\chi}}, \tag{2.11}$$

where $E = \frac{1}{2} m_\chi v^2$ is the WIMP kinetic energy. Here the number of nuclei per gram of the target material is $\dfrac{N_A}{A}$, with N_A the Avogadro's number and A the atomic mass. The WIMP number density on Earth can be expressed as $\dfrac{\rho_\chi}{m_\chi}$, where ρ_χ is the local WIMP density, the average density of WIMPs in a volume of few hundred parsecs around the Sun [55]. In this work we use $\rho_\chi = 0.3\,\mathrm{GeV/cm^3}$, though it should be noted that the uncertainty on this parameter is large, and the typical interval is $[0.2,\ 0.5]\,\mathrm{GeV/cm^3}$ [55]. In this equation σ is the WIMP-nucleus cross section, discussed in section 2.2.

In reality, WIMPs do not all have the same velocity (energy). We showed in section 1.4.1 that the WIMP velocity distribution is a Maxwellian (equation 1.30). The corresponding differential number of WIMPs with speed between v and $v + dv$ (dN) is:

$$dN = 4\pi v^2 \frac{1}{\pi^{3/2} v_0^3} e^{-\frac{v^2}{v_0^2}} dv, \tag{2.12}$$

where v_0 is the most probable WIMP velocity, and has a value of about $220\,\mathrm{km/s}$. It is convenient to rewrite the right hand side of equation 2.12 in terms of the WIMP energy E. We use:

$$v = \sqrt{\frac{2E}{m_\chi}},$$
$$dv = \frac{1}{\sqrt{2m_\chi E}} dE, \tag{2.13}$$

and we rewrite the right hand side of equation 2.12 as:

$$dN = \frac{2}{\sqrt{\pi}} \frac{\sqrt{E}}{E_0^{3/2}} e^{-\frac{E}{E_0}} dE, \tag{2.14}$$

where we introduced the most probable WIMP energy $E_0 = \frac{1}{2} m_\chi v_0^2$.

Including the WIMP energy distribution, the differential rate, dR, can be written as:

$$dR = \frac{N_A}{A}\frac{\rho_\chi}{m_\chi}\sigma\sqrt{\frac{2E}{m_\chi}}dN = \sqrt{\frac{8}{m_\chi^{3/2}\pi}}\frac{N_A}{A}\rho_\chi\sigma\frac{E}{E_0^{3/2}}e^{-\frac{E}{E_0}}dE\,. \qquad (2.15)$$

Where we used equation 2.14. It is convenient to multiply and divide the right hand side of equation 2.15 by $\sqrt{E_0}$, and rewrite equation 2.15 as:

$$dR = R_0\frac{E}{E_0^2}e^{-\frac{E}{E_0}}dE, \qquad (2.16)$$

where we define R_0 as:

$$R_0 = \frac{2}{\sqrt{\pi}}\sqrt{\frac{2E_0}{m_\chi}}\frac{N_A}{A}\frac{\rho_\chi}{m_\chi}\sigma \equiv \frac{2}{\sqrt{\pi}}v_0\frac{N_A}{A}\frac{\rho_\chi}{m_\chi}\sigma\,. \qquad (2.17)$$

If we were able to directly measure the WIMP energy, then the WIMP event rate would be given by the integration of equation 2.16. However, WIMP experiments measure the recoil energy induced by a WIMP-nucleus scattering, and we need to express the differential WIMP event rate as a function of the recoil energy. In equation 2.7 we calculated the relation between the recoil energy and the incoming WIMP energy. Now, we additionally assume that the WIMP-nucleus scattering is isotropic, so there is no preferred value for the cosine of the scattering angle θ. Therefore, for a given WIMP energy E, the recoil energy E_R is uniformly distributed between 0 and Er. Using equation 2.16, the double differential rate, d^2R, can be written as:

$$d^2R = R_0\frac{E}{E_0^2}e^{-\frac{E}{E_0}}\frac{1}{Er}dEdE_R = \frac{R_0}{E_0r}\frac{1}{E_0}e^{-\frac{E}{E_0}}dEdE_R\,. \qquad (2.18)$$

Where the term Er comes from the uniform distribution of the recoil energy for a given WIMP energy. Since we can not directly measure the WIMP energy, we integrate it out. We write the differential WIMP event rate, $\frac{dR}{dE_R}$, as:

$$\frac{dR}{dE_R} = \frac{R_0}{E_0r}\int_{E_{min}}^{E_{max}}\frac{1}{E_0}e^{-\frac{E}{E_0}}dE\,. \qquad (2.19)$$

In the integral bounds, E_{min} is the minimum WIMP energy which can cause a recoil of energy E_R. E_{min} is calculated from equation 2.7: $E_{min} = \frac{E_R}{r}$, where we consider a scattering with $\cos(\theta) = -1$ [56]. So, the E_R dependence of equation 2.19 is hidden in the term E_{min}.

WIMPs with a velocity larger than the galactic escape velocity (v_{esc}) are not gravitationally bound to our galaxy. They do not contribute to the event rate observed on the Earth. Therefore, the maximum WIMP energy is given by $E_{max} = \frac{1}{2}m_\chi v_{esc}^2$.

The integration of equation 2.19 is straightforward. Assuming $v_{esc} = \infty \rightarrow E_{max} = \infty$ (we will comment at the end of the section on this assumption), we obtain:

$$\frac{dR}{dE_R} = \frac{R_0}{E_0 r} e^{-\frac{E_R}{E_0 r}}, \qquad (2.20)$$

while the WIMP rate is given by:

$$R = \int_0^\infty \frac{R_0}{E_0 r} e^{-\frac{E_R}{E_0 r}} dE_R = R_0 . \qquad (2.21)$$

R_0 gives the expected number of events per unit mass and unit time. Using $v_0 = 220\,\text{km/s}$, $\rho_\chi = 0.3\,\text{GeV/cm}^3$, $m_\chi = 100\,\text{GeV}$, $\sigma = 6 \times 10^{-38}\,\text{cm}^2$ and $A = 131.3\,\text{g/mol}$ (xenon target), we obtain a value of R_0 of about $0.6\,\text{kg}^{-1}\,\text{y}^{-1}$ from equation 2.17. This result shows that the expected rate is low and a WIMP experiment needs to be sensitive to very small rates (see also section 2.3). The WIMP-nucleus cross section, which we used in the calculation, is calculated from an excluded WIMP-nucleon cross section by direct detection experiments of about 10^{-45} cm^2 [57]. We will show in section 2.2 the relation between the WIMP-nucleus and the WIMP-nucleon cross section.

In addition, the average recoil energy ($< E_R >$) can be calculated as:

$$< E_R >= \frac{\int_0^\infty E_R \frac{dR}{dE_R} dE_R}{\int_0^\infty dE_R \frac{dR}{dE_R}} = E_0 r . \qquad (2.22)$$

Therefore, the most probable WIMP energy E_0 is also related to $< E_R >$. Using $m_\chi = 100\,\text{GeV}$ and $v_0 = 220\,\text{km/s}$, and considering a xenon target ($m_N = 122\,\text{GeV}$) we have $r \simeq 1$ and $< E_R > \simeq E_0 \simeq 27\,\text{keV}$.

The differential event rate is slightly modified when taking into account a finite escape velocity. The Maxwellian distribution is truncated for velocities larger than v_{esc}, resulting in a slightly different normalization constant for the Maxwellian. Considering a realistic escape velocity of $544\,\text{km/s}$, the hypothetical number of WIMPs with velocity higher than v_{esc} is less than 1%. The differential event rate including the effect of a finite escape velocity is expressed as [58]:

$$\frac{dR}{dE_R} = K \left[\frac{R_0}{E_0 r} \left(e^{-\frac{E_R}{E_0 r}} - e^{-\frac{v_{esc}^2}{v_0^2}} \right) \right] . \qquad (2.23)$$

Where K is a normalization constant given by $K = \left[\text{erf}(\frac{v_{esc}}{v_0}) - \frac{2}{\sqrt{\pi}} \frac{v_{esc}}{v_0} e^{-\frac{v_{esc}^2}{v_0^2}} \right]^{-1} \simeq 0.993$ and erf is the error function, $\text{erf}(x) = \frac{2}{\sqrt{\pi}} \int_0^x e^{-t^2} dt$.

Fig. 2.2 shows the differential event rate of equation 2.21 (black line) and equation 2.23 (red line), which is calculated with an escape velocity of $544\,km/s$ [56] [35]. The difference is about 10% for recoil energies of about $100\,keV$ and increasing with the energy due to the additional exponential in equation 2.23.
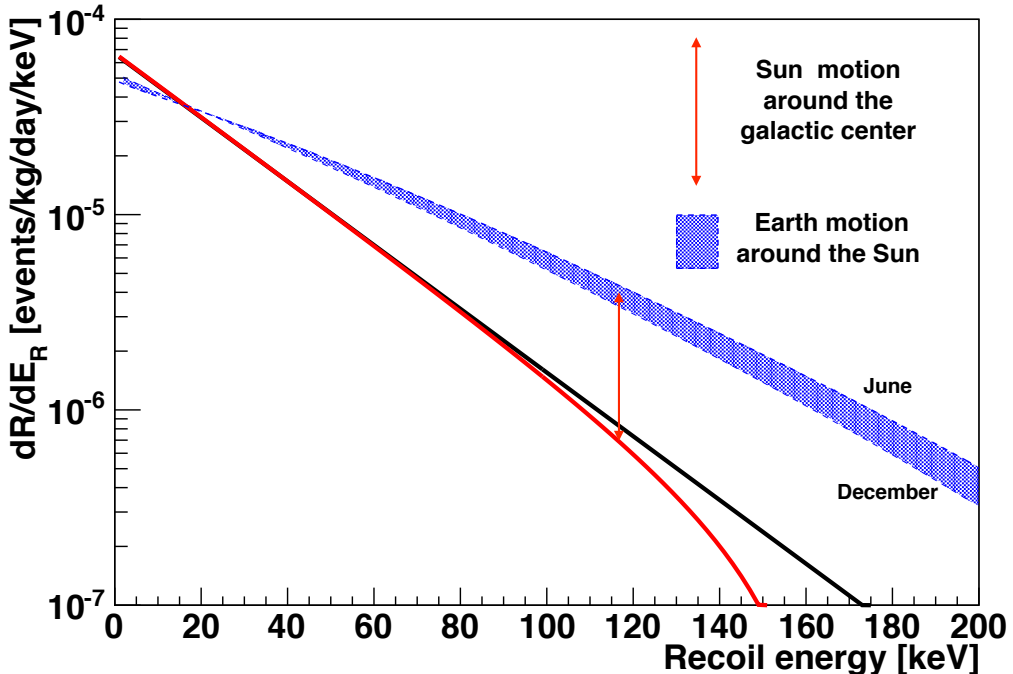
Figure 2.2: *Differential event rates calculated using $v_0 = 220\,km/s$, $\rho_\chi = 0.3\,GeV/cm^3$, $m_\chi = 100\,GeV$, $\sigma = 6 \times 10^{-38}\,cm^2$ (WIMP-nucleus cross section) and $A = 131.3\,g/mol$. The black line is the differential event rate assuming the Earth velocity in the galactic rest frame $v_E = 0$ and the galactic escape velocity $v_{esc} = \infty$. The red line is the differential event rate assuming $v_E = 0$ and $v_{esc} = 544\,km/s$. When considering the Earth velocity, the differential event rate is shifted to higher energies. The effect due to the Sun's rotation around the galactic center is indicated by the red double arrow. The differential event rate varies during the year due to the Earth's rotation around the Sun as indicated by the shaded blue area.*

2.1.3 Event rate including the Earth velocity

Thus far, we have assumed that the Earth is at rest in the galaxy and that the WIMP velocity distribution is given by the Maxwellian in equation 1.30. Therefore, we have neglected that the Sun is rotating around the galactic center and that the Earth is rotating around the Sun. The Maxwellian distribution is usually defined as the WIMP

velocity distribution in the galactic rest frame, which is the frame where the galactic center is at rest [59]. Fig. 2.3 shows a simplified view of the Earth's motion in the galactic rest frame. The Earth velocity in the galactic rest frame ($\vec{v}_E$) is given by the sum of Sun's motion around the galactic center and of the Earth's motion around the Sun:

$$\vec{v}_E = \vec{v}_S + \vec{v}_E^S. \tag{2.24}$$

Where $\vec{v}_S$ is the motion of the Sun with respect to the galactic rest frame.
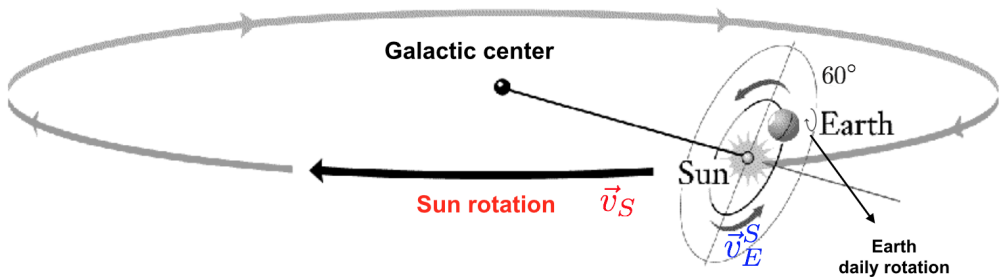
Figure 2.3: *A simplified view of the Earth's motion in the galactic rest frame. The Sun is rotating around the galactic center with a velocity v_S of about 220 km/s. The Earth is rotating around the Sun with a velocity v_E^S of about 30 km/s. The Earth's daily rotation is also indicated, even if the velocity (0.5 km/s) is a factor 60 smaller than v_E^S. The angle between the Earth's orbit plane and the galactic plane containing the orbit of the Sun is about 60°. Figure adapted from [60].*

We described in section 1.4.1 that the Sun is rotating around the galactic center with a velocity v_0 of about 220 km/s. Furthermore, the Sun has its own proper motion compared to nearby stars, which results approximately in a 5% correction to v_0. Therefore, we have $\vec{v}_S \simeq \vec{v}_0$. $\vec{v}_E^S$ is the Earth orbital velocity relative to the Sun. The Earth is rotating around the Sun with a velocity v_E^S of about 30 km/s. The Earth's orbit plane is about 60° tilted respect to the galactic plane containing the Sun's orbit. $\vec{v}_E^S$ has a time dependence because the direction of the Earth orbital velocity relative to the Sun's motion is changing during the year: the Earth has the highest relative speed with respect to the Sun's motion in the beginning of June and the lowest in the beginning of December.

The Earth is also daily rotating around its axis, but this rotational velocity is a about a factor 60 smaller than the rotational velocity around the Sun [59]. Therefore, the daily modulation is hard to experimentally detect due to the small value of the Earth's rotational velocity around its axis [59]. Instead, the motion of the Sun around

the galactic center and the rotation of the Earth around the Sun determine two peculiar WIMP signatures:

- **Cygnus direction.** As the Sun rotates around the galaxy, we expect to experience a WIMP wind opposite to the Sun's direction of motion through the galaxy. This direction points towards the Cygnus constellation [35].

- **Annual modulation.** In the galactic rest frame, the Earth velocity is changing during the year. The differential event rate is modulating according to [59]:

$$\frac{dR}{dE_R} \simeq S_0(E_R) + S_m(E_R) \cos\left(\frac{2\pi(t - t_0)}{T}\right).$$ (2.25)

Where $S_0(E_R)$ is the time-averaged rate, $S_m(E_R)$ is the modulation amplitude with $S_m(E_R) << S_0(E_R)$, t is the time in days, $t_0 = 152.5$ days corresponds to the period of the year when the Earth speed with respect to the Sun's motion is maximum. $T = 365.25$ days is the period of the Earth's rotation around the Sun. The quantity $S_m(E_R)/S_0(E_R)$ is defined as the fractional amplitude of the annual modulation. It is about 5%, and it depends on the considered recoil energy: the higher the energy, the higher is the modulation amplitude [35] [59].

The main characteristics of the WIMP signal can be found considering only the motion of the Sun and the time-dependent component of the Earth velocity in that direction [35]. In this way, the Earth velocity, v_E, is parameterized as [56]:

$$v_E \simeq v_0 \left[1.05 + 0.07 \cos\left(2\pi \frac{t - t_0}{T}\right)\right].$$ (2.26)

Where T and t_0 were introduced in equation 2.25. Here, the factor 1.05 is due to the 5% correction to v_0, while $\frac{v_E^S}{v_0} \cos(60°)\left(2\pi \frac{t - t_0}{T}\right) \simeq 0.07\left(2\pi \frac{t - t_0}{T}\right)$ is the component of the Earth velocity parallel to v_0. Implementing the Earth velocity changes the WIMP velocity distribution and, therefore, the differential event rate. The WIMP velocity distribution can be obtained through a Galilean velocity transformation [59]:

$$f(\vec{v'}) = f(\vec{v} + \vec{v}_E),$$ (2.27)

where $\vec{v}$ is the WIMP velocity in the galactic rest frame. The calculation of the differential event rate considering the aforementioned WIMP velocity distribution is done in [61]. Fig. 2.2 shows the differential event rate when including the Earth velocity in the WIMP velocity distribution (shaded blue area). The differential event rate is shifted to higher energies compared to $v_E = 0$ (equation 2.23). The most significant effect is caused by the motion of the Sun indicated by the red double arrows. Due to the Earth's motion, the differential event rate is slightly changing during the year with a maximum in June and a minimum in December.

2.2 WIMP-nucleus and WIMP-nucleon cross section

The WIMP-nucleus cross section is the measured cross section by WIMP experiments. However, to compare results of different experiments the WIMP-nucleon cross section is typically used in the direct detection field. The reason is straightforward: given a certain WIMP-nucleon cross section, the WIMP-nucleus cross section will be higher i.e. in xenon compared to germanium simply because xenon has an higher atomic mass number. To calculate the WIMP-nucleon cross we need to make assumptions about the underlying scattering mechanism, considering a spin-independent (SI) and a spin-dependent (SD) contribution.

Thus far, we have also assumed that the nucleus is small compared to the De Broglie wavelength corresponding to the momentum transfer. If this is not the case, a form factor correction must be included in the WIMP-nucleus cross section to account for the finite size of the nucleus. For example, for a xenon nucleus with a diameter of $\approx 13\,\mathrm{fm}$, which is comparable to the De Broglie wavelength, significant decoherence will take place, so the nuclear form factor can no longer be ignored. The form factor correction will be discussed separately for the spin-independent and spin-dependent cross section.

2.2.1 Spin-independent WIMP-nucleus cross section

For the spin-independent case, the WIMP-nucleus cross section is expressed as [56]:

$$\sigma^{SI} = \frac{4\mu^2}{\pi}(Zf_p + (A-Z)f_n)^2 . \tag{2.28}$$

Where μ is the WIMP-nucleus reduced mass, Z is the atomic number of the target, A is the mass number, and f_p (f_n) is the effective WIMP coupling to a proton (neutron). For the analysis presented here, as in most of the literature, it is assumed that the effective WIMP couplings are isospin independent, $f_n = f_p$. Under this assumption, the WIMP-nucleus cross section can be rewritten as:

$$\sigma^{SI} = \frac{4\mu^2}{\pi}f_p^2 A^2 \equiv \frac{4}{\pi}\mu_p^2 f_p^2 \frac{\mu^2 A^2}{\mu_p^2} \equiv \sigma_p^{SI}\frac{\mu^2 A^2}{\mu_p^2} . \tag{2.29}$$

Where μ_p is the reduced WIMP-proton mass and the WIMP-nucleon cross section is defined as $\sigma_p^{SI} = \frac{4}{\pi}\mu_p^2 f_p^2$. Equation 2.29 shows that the spin-independent WIMP-nucleus cross section scales proportionally to A^2. Hence it is crucial to select a target with the highest possible A.

As mentioned above, the WIMP-nucleus cross section must be corrected for the finite size of the nucleus. In the spin-independent case, the form factor correction can

be expressed using the formulation in [62]:

$$F_{SI}^2 = (3\frac{\sin(qr_n) - qr_n\cos(qr_n)}{(qr_n)^3})^2 e^{-q^2 s^2} . \tag{2.30}$$

In this equation, q is the momentum transfer, r_n is the effective nuclear radius for which we use the parametrization given in [58]. The nuclear density is assumed to be constant within the radius r_n. s is a measure of the nuclear skin thickness "the radial distance in which the density goes from 90% of its central value to 10% [56]", and it is about 1 fm. Fig. 2.4 shows the form factor for a xenon, germanium and argon target.
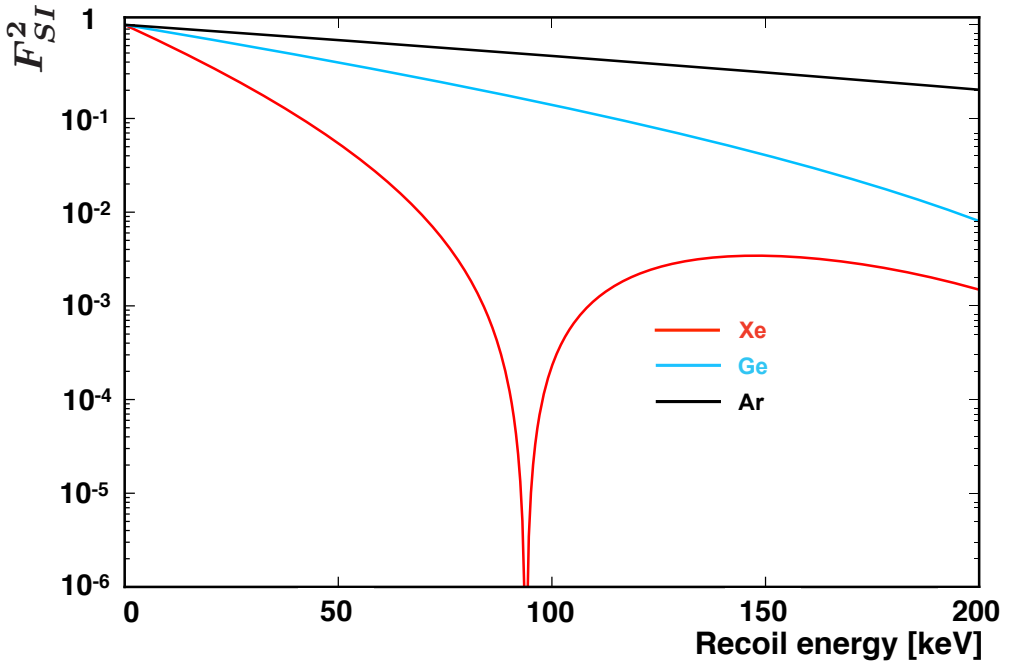
Figure 2.4: *Form factors for targets used in direct detection experiments. Red is used for a xenon target ($A = 131$), azure for a germanium target ($A = 70$) and black for an argon target ($A = 40$).*

For xenon, the form factor rapidly decreases because of the relatively large radius of the xenon nucleus of about 6 fm. At 50 keV the form factor correction decreases the WIMP-nucleus cross section of about 95%. The first minimum is located at recoil energies of about 90 keV where the scattering coherence is completely lost. For germanium and argon the form factor correction is less important compared to xenon because the radius of the nucleus is about 5 fm for germanium and 4 fm for argon. At

50 keV the form factor correction decreases the WIMP-nucleus cross section by 60% for germanium and 33% for argon.

The form factor is usually incorporated in the WIMP-nucleus spin-independent cross section as [58]:

$$\sigma^{SI}(q) = \sigma^{SI} F_{SI}^2(qr_n), \qquad (2.31)$$

with σ^{SI} given by equation 2.29.
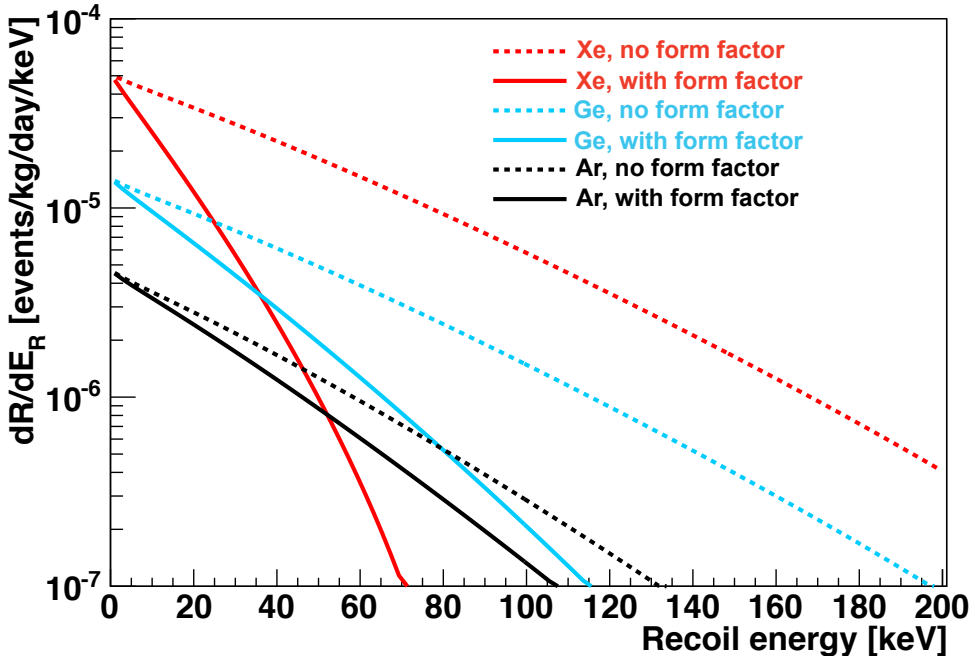
Figure 2.5: *Differential event rate for different direct detection targets with and without the form factor correction. The dashed lines are the differential event rates without the form factor correction. The solid lines are the differential event rates with the form factor correction. Red is used for a xenon target ($A = 131$), azure for a germanium target ($A = 70$) and black for an argon target ($A = 40$). The differential event rates are calculated assuming a WIMP-nucleon cross section of about 10^{-45} cm^2.*

Fig. 2.5 shows the differential event rate for a xenon target ($A = 131$), a germanium target ($A = 70$) and an argon target ($A = 40$), which are commonly used in WIMP experiments. The differential event rates scale as A^2 for the three targets at $E_R = 0$. Considering the form factor correction, the differential event rate is lower than the one without the form factor for the three targets. The difference increases as a function of energy since the De Broglie wavelength decreases as a function of energy (equation

2.10). The loss of coherence reduces the advantage of using a high A target for large recoil energies: the differential event rate for xenon is lower than the one in germanium (argon) for recoil energies larger than about $35\,\mathrm{keV}$ ($55\,\mathrm{keV}$).

2.2.2 Spin-dependent WIMP-nucleus cross section

For the spin-dependent case, the WIMP-nucleus cross section is expressed as [56]:

$$\sigma^{SD} = \frac{32}{\pi}\mu^2 G_F^2 \Lambda^2 J(J+1)\,. \tag{2.32}$$

Where G_F is the Fermi coupling constant, J is the total angular momentum of the nucleus, Λ is a linear combination of the expectation value of the spin content of protons and neutrons in the nucleus (S_p, S_n), $\Lambda = \frac{1}{J}(a_p < S_p > +a_n < S_n >)$. At first approximation, Λ can be calculated using the single-particle shell model, which assumes that the nuclear spin is due to an unpaired neutron or proton in the nucleus [35]. To compare different targets, we use the effective cross section of the interaction with a nucleon (σ_p^{SD} or σ_n^{SD}). For a proton (neutron) not bound in the nucleus, we have from equation 2.32:

$$\sigma_{p,n}^{SD} = \frac{32}{\pi}G_F^2 \mu_{p,n}^2 \frac{3}{4}a_{p,n}^2\,. \tag{2.33}$$

Where $\mu_{p,n}$ is the WIMP-nucleon reduced mass, and we use $< S_{p,n} >= 1/2$ and $J = 1/2$. Under the assumption that WIMPs couple only to protons or neutrons in the nucleus, we can relate the spin-dependent WIMP-nucleon cross section to the spin-dependent WIMP-nucleus cross section using equation 2.32 and 2.33:

$$\sigma_{p,n}^{SD} = \frac{3}{4}\frac{J}{J+1}\frac{\mu_{p,n}^2}{\mu^2}\frac{\sigma^{SD}}{< S_{p,n} >^2}\,. \tag{2.34}$$

Where we set respectively a_n or a_p to zero. $\sigma_{p,n}^{SD}$ is the cross section that is reported in direct detection results. Odd-numbered isotopes have a nuclear spin different than zero, being therefore sensitive to the spin-dependent coupling.

The form factor correction is incorporated in the cross section as in the spin-independent case:

$$\sigma^{SD}(q) = \sigma^{SD}F_{SD}^2(qr_n)\,. \tag{2.35}$$

The detailed calculation of the spin-dependent form factor can be done using the complete nuclear shell model and empirical parameterizations of the residual nuclear potential. A complete derivation is in [63] and [64], while an approximate expression is given in [56]:

$$F_{SD}(qr_n) = \frac{\sin(qr_n)}{qr_n}\,. \tag{2.36}$$

2.2.3   Comparison of SI and SD WIMP-nucleus cross sections

We briefly compare the spin-independent and spin-dependent WIMP-nucleus cross section. In minimal supersymmetric theories, the ratio of the spin-independent WIMP-proton cross section over the spin-dependent WIMP-proton cross section is about [36]:

$$10^{-4} < \frac{\sigma_p^{SI}}{\sigma_p^{SD}} < 10^{-2} \,. \tag{2.37}$$

Where the range of factors from 10^{-2} to 10^{-4} depends on the underlying assumption on the WIMP particle and on the WIMP effective couplings [36]. Based on equation 2.37 we would expect that the spin-dependent WIMP-nucleus cross section dominates over the spin-independent WIMP-nucleus cross section. But, the spin-independent WIMP-nucleus cross section is enhanced by a factor A^2 that is absent for the spin-dependent WIMP-nucleus cross section. The spin factors in equation 2.32 are of order of unity. So, the combination of equation 2.37 and the factor A^2 implies that the spin-independent WIMP-nucleus cross section is larger than the spin-dependent WIMP-nucleus cross section for $A \gtrsim 40$, depending on the underlying assumptions on $\frac{\sigma_p^{SI}}{\sigma_p^{SD}}$. Considering a xenon target ($A = 131$) and assuming $\frac{\sigma_p^{SI}}{\sigma_p^{SD}} \simeq 10^{-3}$, the ratio of the spin-independent WIMP-nucleus cross section over the spin-dependent WIMP-nucleus cross section is given by:

$$\frac{\sigma^{SI}}{\sigma^{SD}} \simeq A^2 \times \frac{\sigma_p^{SI}}{\sigma_p^{SD}} \simeq 18 \,. \tag{2.38}$$

Therefore, the spin-independent WIMP-nucleus cross section is expected to be about an order of magnitude larger than the spin-dependent one.

2.3   WIMP detectors

Due to the extremely low WIMP-nucleon cross section and the exponentially decreasing recoil energy spectrum, it is very hard to detect WIMP interactions. In order to have a chance to observe WIMPs, a detector needs:

- **A large exposure.** In section 2.1.2 we showed that a WIMP with a mass of $100 \, \text{GeV}$ and a WIMP-nucleon cross section of $10^{-45} \, \text{cm}^2$ (corresponding to a WIMP-nucleus cross section of $6 \times 10^{-38} \, \text{cm}^2$ in a xenon target) determines an event rate of about $0.6 \, \text{kg}^{-1} \, \text{y}^{-1}$. The number of events increases linearly with

the target mass and with the livetime of the experiment[1]. The product of the
target mass and of the livetime is defined as the exposure of a WIMP experiment.
The exposure should be as high as possible.

- **A low energy threshold.** The exponentially decreasing energy spectrum makes
  a low energy threshold mandatory to increase the sensitivity to WIMPs. If we
  consider a xenon target and WIMPs with a mass larger than $50\,\text{GeV}$, the mean
  recoil energy is of the order of tens of keV, whereas the mean recoil energy is
  of the order of few keV for WIMPs with a mass below $20\,\text{GeV}$. A low energy
  threshold is especially beneficial for the sensitivity[2] to low-mass WIMPs.
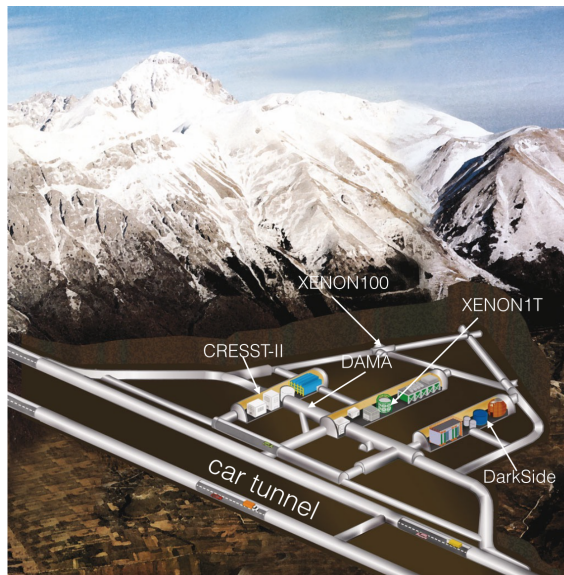
Figure 2.6: *Illustration of the deep-underground laboratory of Gran Sasso and of the WIMP experiments located there. The XENON100 experiment featured in this thesis is located in the laboratory of Gran Sasso. Figure adapted from [65].*

- **A low background.** Since the event rate is low, the sensitivity is higher for
  lower backgrounds. Common features of all the WIMP experiments are that they
  use materials with low radioactive contamination, and that they are located deep-
  underground because the rock surrounding underground laboratories significantly
  attenuates the cosmic-ray flux. Fig. 2.6 shows an illustration of the laboratory

---

[1]The time in which an experiment acquires data to search for WIMPs.
[2]The value of the excluded WIMP-nucleon cross section at a given WIMP mass. Higher (lower) sensitivity means a lower (higher) excluded WIMP-nucleon cross section.

of Gran Sasso and of the WIMP experiments located there. The laboratory is at a depth of about 3500 meter water equivalent. The XENON100 experiment featured in this thesis is located in the laboratory of Gran Sasso. The background rate can be further reduced using particle identification techniques and rejecting backgrounds towards the edge of the detector as will be described below.

Different technologies have been developed to fulfill the aforementioned requirements.
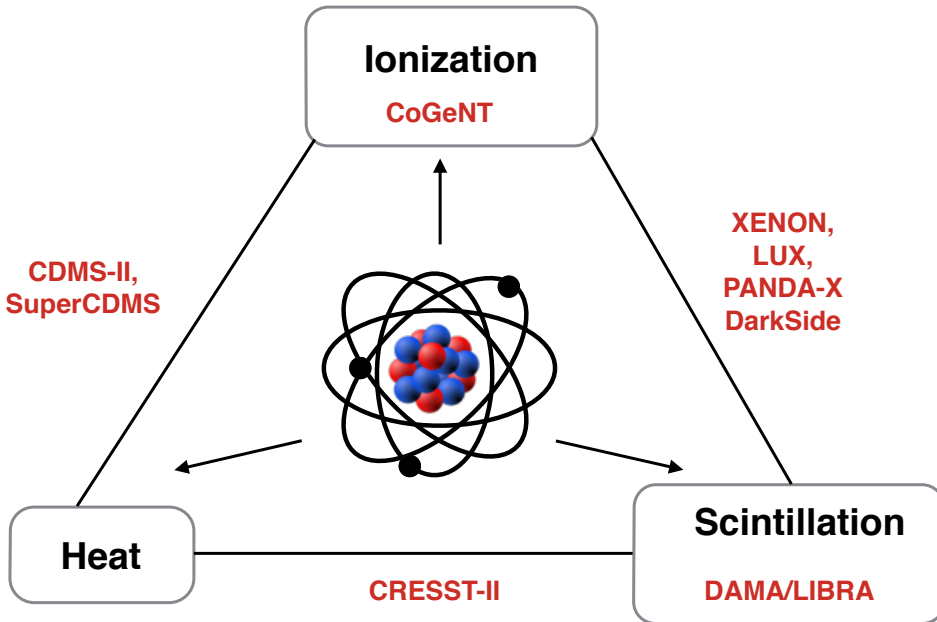
Figure 2.7: *The recoil energy caused by a WIMP interaction is dissipated in three ways: scintillation, ionization and heat. The names in the figure are WIMP experiments. Experiments between the boxes like SuperCDMS, XENON, LUX and CRESST-II are sensitive to two dissipation mechanisms. Experiments inside the boxes like CoGeNT and DAMA/LIBRA are sensitive to only one dissipation mechanism.*

As shown schematically in Fig. 2.7, the recoil energy deposited through a nuclear recoil can be dissipated in three different ways:

- **Heat.** The recoil energy of the nucleus is dissipated into heat, increasing the kinetic energy of the atoms of the target.

- **Scintillation.** The recoil energy of the nucleus excites the atoms of the target, that subsequentially de-excite emitting photons.

- **Ionization.** The recoil energy of the nucleus directly ionizes the atoms of the target, resulting in a production of free electric charge carriers and notably electrons.

All WIMP experiments observe either one or two of these dissipation mechanisms, which can be used to perform particle identification, to measure the recoil energy and to reconstruct the position of the interaction. Fig. 2.8 shows an illustration of a background-induced electronic recoil and a WIMP-induced nuclear recoil.
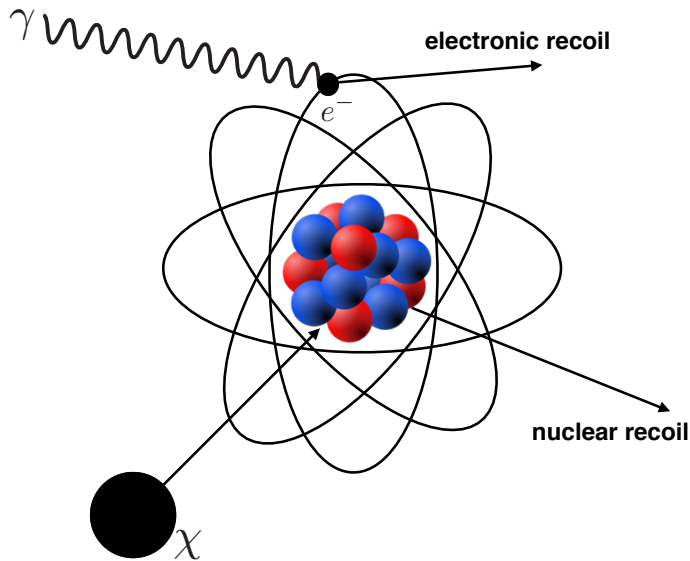
Figure 2.8: *Illustration of a background-induced electronic recoil and of a WIMP-induced nuclear recoil.*

Most backgrounds, e.g. γ-rays, induce electromagnetic interactions causing an electronic recoil, while WIMPs interact with the nucleus causing a nuclear recoil. The target response to an electronic recoil is different from the response to a nuclear recoil. The fraction of energy which is expended into the different dissipation mechanisms varies depending on the type of the interaction. Therefore, measuring at least two dissipation mechanisms potentially allows the rejection of a large fraction of background.

Another general feature of WIMP detectors is the reconstruction of the position of the interaction. A part of the background is coming from the residual radioactivity in the construction materials surrounding a detector. In the regions close to the edge of the active target volume, the backgrounds are dominant compared to a WIMP signal, which should be uniformly distributed. Therefore, the sensitivity of an experiment can

be increased rejecting events at the edges of the target volume. This feature is often referred to as fiducialization or as defining a fiducial volume.

Direct WIMP searches began in 1980 using high-purity germanium detectors, as still used today by, for example, the CoGeNT experiment [66]. High-purity germanium detectors can measure only the ionization caused by a WIMP interaction, and can achieve a low-energy threshold of about 1 keV. Since only the ionization can be detected a large fraction of the electronic recoil background can not be suppressed. Another technique uses highly radiopure thallium-doped sodium-iodide crystal scintillators, e.g. the DAMA/LIBRA experiment [67]. A low-energy threshold of about 2 keV is achievable. Only the scintillation can be measured, and also for this technology the electronic recoil background can not be rejected.

In order to discriminate between electronic recoils and nuclear recoils, different technologies have been developed. Cryogenic solid-state detectors can measure, for example, simultaneously the heat and the ionization, e.g. SuperCDMS [68], or the heat and the scintillation, e.g. CRESST-II [69]. They can achieve an energy threshold lower than 1 keV. Other types of detectors which are sensitive to both the ionization and the scintillation are the xenon dual-phase (liquid-gas) Time Projection Chambers (TPC), e.g. XENON1T, XENON100, LUX [70], PANDA-X [71]. This technology can be relatively easily scaled to ton-scale experiments because it mainly employs the liquid xenon phase. Xenon TPCs have a slightly higher energy threshold of about 5 keV. Therefore, the sensitivity to low-mass WIMPs is reduced compared to aforementioned experiments.

Experiments employing argon as a target, e.g. DarkSide [72], are similar to the xenon TPCs. However, argon detectors must be purified from an intrinsic radioactive isotope, ^{39}Ar, to be competitive for WIMP searches. After the removal of ^{39}Ar, argon does not contain odd isotopes, rendering these experiments insensitive to the spin-dependent WIMP-nucleus cross section. In argon, the scintillation light is produced after the decay of excited molecules. This mechanism is the same for xenon, and it will be explained in section 3.1.1. The excited molecules can exist in a singlet or a triplet state. Singlet states are more abundant in nuclear recoils, while triplet states are more abundant in electronic recoils [73]. Singlet and triplet states have different decay times to the ground state. In xenon, the singlet and triplet decay time are, respectively, 3 ns and 24 ns [74], so pulse shape discrimination techniques do not improve significantly the rejection of the electronic recoil background. Instead, in argon the singlet and triplet decay time are, respectively, 7 ns and 1600 ns [73]. Therefore, argon-based experiments can additionally employ pulse shape discrimination techniques to further reduce the

electronic recoil background by a factor of 1.5×10^7 or even higher using the different singlet and triplet decay times [72].

2.4 Direct Detection: Experimental results

Fig. 2.9 shows the exclusion limits and claims reported for the spin-independent WIMP-nucleon cross section as a function of the assumed WIMP mass, given at 90% confidence level[1].
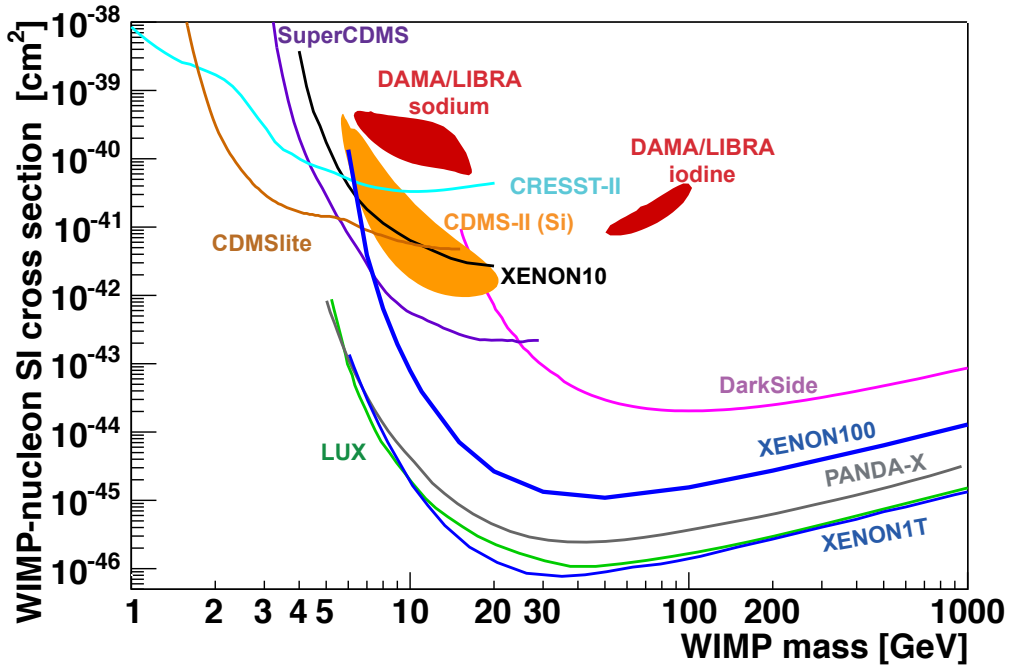
Figure 2.9: *Direct detection exclusion limits and claims of WIMPs as of at the end of August 2017. The results are plotted in the WIMP-nucleon spin-independent (SI) cross section versus the WIMP mass parameter space. The XENON1T collaboration sets the most stringent exclusion limit, ruling out a cross section of 7.7×10^{-47} cm^2 at a WIMP mass of 35 GeV. The WIMP observation claimed by the DAMA/LIBRA collaboration and the WIMP evidence from the CDMS-II collaboration (CDMS-II (Si)) are also shown.*

---

[1]One should note that the null results of the collider experiments can be interpreted in terms of an excluded WIMP-nucleon spin-independent cross section for a given WIMP mass. These results are model dependent, and they are generally weaker compared to WIMP experiments for all WIMP masses except for WIMPs with a mass below about 5 GeV. Therefore, the results from collider experiments are omitted for clarity in this figure.

WIMP experiments measure the event rate, which is a function of both the unknown WIMP-nucleon cross section and the unknown WIMP mass (equation 2.17). So, there is a degeneracy between the WIMP-nucleon cross section and the WIMP mass. In Fig. 2.9, an exclusion limit is drawn as a solid line. WIMP-nucleon spin-independent cross sections (σ_p^{SI}) and masses above the exclusion line are excluded, while cross sections and masses below the exclusion line are still allowed.

Above 10 GeV the most sensitive experiment is the XENON1T experiment, which uses a xenon TPC and has an exposure of 97.6 kg × year. The most stringent exclusion limit is reached for a WIMP with $\sigma_p^{SI} = 7.7 \times 10^{-47}\,\text{cm}^2$ at $m_\chi = 35$ GeV [75]. The main drivers of the XENON1T sensitivity are the lowest background level ever achieved in a WIMP experiment [75] and the large exposure. Between 6 GeV and 10 GeV, the LUX experiment has a better limit compared to the XENON1T experiment due to a better energy threshold. The LUX experiment uses a xenon TPC and has an exposure of 119.3 kg × year [57]. The most stringent exclusion limit[1] is reached for a WIMP with $\sigma_p^{SI} = 1.1 \times 10^{-46}\,\text{cm}^2$ at $m_\chi = 50$ GeV [57]. The PANDA-X experiment [71] also uses a xenon TPC and has an exposure of 89.0 kg × year. The most stringent exclusion limit is reached for a WIMP with $\sigma_p^{SI} = 2.5 \times 10^{-46}\,\text{cm}^2$ at $m_\chi = 40$ GeV [71]. The PANDA-X exclusion limit is slightly better compared to the LUX experiment for WIMPs with a mass between 5 and 6 GeV due to the slightly better energy threshold of the PANDA-X experiment compared to the LUX experiment.

The XENON100 experiment has an exposure of 48.3 kg × year. The most stringent exclusion limit is reached for a WIMP with $\sigma_p^{SI} = 1.1 \times 10^{-45}\,\text{cm}^2$ at $m_\chi = 50$ GeV [3]. The XENON1T exclusion limit is better by more than a factor of 10 compared to the XENON100 limit due mainly to the much lower background rate of the XENON1T experiment compared to the XENON100 experiment. A general feature of xenon detectors is that the cross section exclusion rapidly deteriorates for low-mass WIMPs due to the limited energy threshold of about 5 keV, it reaches the maximum exclusion for a WIMP with a mass of about 50 GeV, and subsequently it rises smoothly with the WIMP mass. A high WIMP mass implies a lower number density, since the number density of WIMPs is fixed by $n_\chi = \rho_\chi / m_\chi$.

The DarkSide experiment, which employs an argon TPC, has an exposure of 7.16 kg × year. The most stringent exclusion limit is reached for a WIMP with $\sigma_p^{SI} = 3 \times 10^{-44}\,\text{cm}^2$ at $m_\chi = 100$ GeV. The DarkSide experiment is, currently, approximately two

---

[1]Despite the larger exposure compared to the XENON1T experiment, the background rate in the LUX experiment is larger compared to the XENON1T experiment. The larger background level causes the slightly worse limit compared to XENON1T for WIMPs with a mass above 10 GeV.

order of magnitude less sensitive compared to the XENON1T and the LUX experiment. The reason is twofold:

- The exposure is more than a factor 10 lower compared to xenon-based experiments;

- The rejection of the electronic recoil background using pulse shape discrimination techniques reaches the maximum efficiency for recoil energies larger than about $40\,\text{keV}$, which can only be produced by high-mass WIMPs. Therefore, if the DarkSide experiment uses an exposure comparable to the aforementioned xenon-based experiments, the DarkSide collaboration will be potentially able to set competitive exclusion limits for high-mass WIMPs. However, the efficiency of the pulse shape discrimination technique drops sharply for low-mass WIMPs, due to the lower value of the induced recoil energy. Therefore, for low-mass WIMPs, argon-based experiments are not competitive compared to xenon-based experiments.

In Fig. 2.9, the dark-red contour regions are the claims of WIMPs made by the DAMA/LIBRA collaboration using sodium-iodide detectors [67]. Assuming that WIMPs interact only with sodium, the DAMA/LIBRA collaboration has reported the discovery of a WIMP with $\sigma_p^{SI} = 2 \times 10^{-40}\,\text{cm}^2$ at $m_\chi = 10\,\text{GeV}$. Instead, assuming that WIMPs interact only with iodine, the DAMA/LIBRA collaboration has reported the discovery of a WIMP with $\sigma_p^{SI} = 10^{-41}\,\text{cm}^2$ at $m_\chi = 70\,\text{GeV}$ [76]. We will focus on the DAMA/LIBRA claim in section 2.4.1.

Another experiment which has reported a 3σ evidence (orange contour region in Fig. 2.9) for low-mass WIMPs is the CDMS-II experiment, which uses a germanium and silicon cryogenic solid-state detector. Analysing only its silicon (Si) detectors, CDMS-II found three events with a background prediction of $0.41^{+0.48}_{-0.32}$ [77]. The background-only hypothesis was tested against the WIMP+background hypothesis resulting in a probability of 0.19% for the background-only hypothesis [77]. The best fit is found for a WIMP with $\sigma_p^{SI} = 1.9 \times 10^{-41}\,\text{cm}^2$ at $m_\chi = 8.6\,\text{GeV}$ [77]. This 3σ evidence was not confirmed by the CDMS upgrade, the SuperCDMS experiment. The SuperCDMS experiment has also operated its detector with a lower energy threshold for a dedicated low-mass WIMP search, called CDMSlite. This search has the best exclusion limit in the $2 < m_\chi < 5\,\text{GeV}$ mass region [78], ruling out a spin-independent WIMP-nucleon cross section of about $2 \times 10^{-41}\,\text{cm}^2$. For WIMPs with a mass below $2\,\text{GeV}$ the CRESST-II experiment has the best exclusion limit, ruling out a WIMP-nucleon cross section of about $3 \times 10^{-39}\,\text{cm}^2$. It should be noted that low-mass WIMP observations were made

also by the CoGeNT experiment in 2014 [66] and by the CRESST-II experiment in 2012 [79], but the excess of events were probably due to unaccounted backgrounds.

The black line in Fig. 2.9 is the exclusion limit by the XENON10 experiment [80]. XENON10 was the first phase of the XENON project, performing the first low-mass WIMP search with a xenon TPC. In this thesis (chapter 5) we will use a similar method to perform a low-mass WIMP search with the XENON100 experiment, lowering the energy threshold by about a factor of 10. In this way, we will improve the sensitivity of the XENON100 experiment for WIMPs with a mass below about 7 GeV.
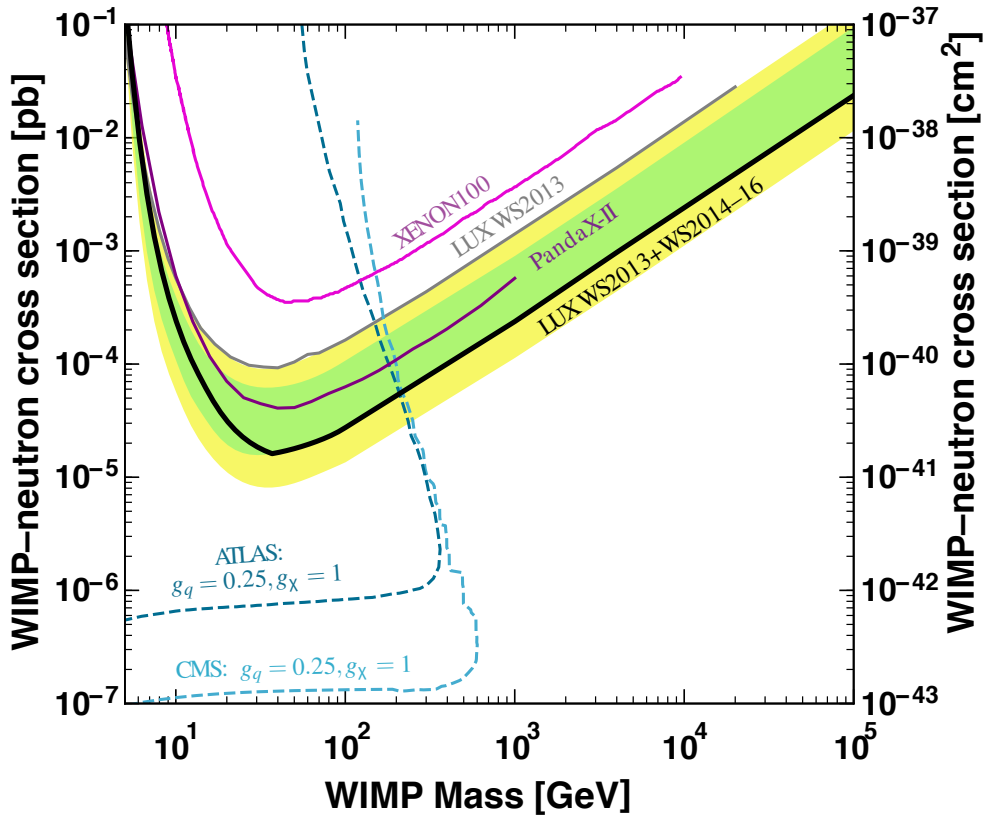
Figure 2.10: *WIMP-neutron spin-dependent (SD) cross section versus the WIMP mass as recently reported by the LUX collaboration. From [81].*

The null results previously interpreted in terms of the WIMP-nucleon spin-independent cross sections can also be interpreted in terms of the WIMP-nucleon spin-dependent cross section. The LUX collaboration has recently reported their results in terms of the spin-dependent WIMP-proton and WIMP-neutron cross section [81].

Fig. 2.10 shows the results for the spin-dependent WIMP-neutron cross section. The LUX experiment has the best sensitivity on the spin-dependent WIMP-neutron cross section among direct detection experiments excluding a spin-dependent WIMP-neutron cross section of 1.6×10^{-41} cm^2 at a WIMP mass of 35 GeV. Also collider experiments can interpret their null results in terms of the spin-dependent WIMP-neutron cross section assuming minimal simplified Dark Matter models [82] characterized by the Dark Matter and the mediator masses and by the mediator coupling to quarks (g_q) and WIMPs (g_χ). The exclusion limits set by collider experiments are more than a factor 10 better compared to the LUX exclusion limit below 300 GeV, even though one should also note that the exclusion limits set by collider experiments heavily rely on model assumptions.
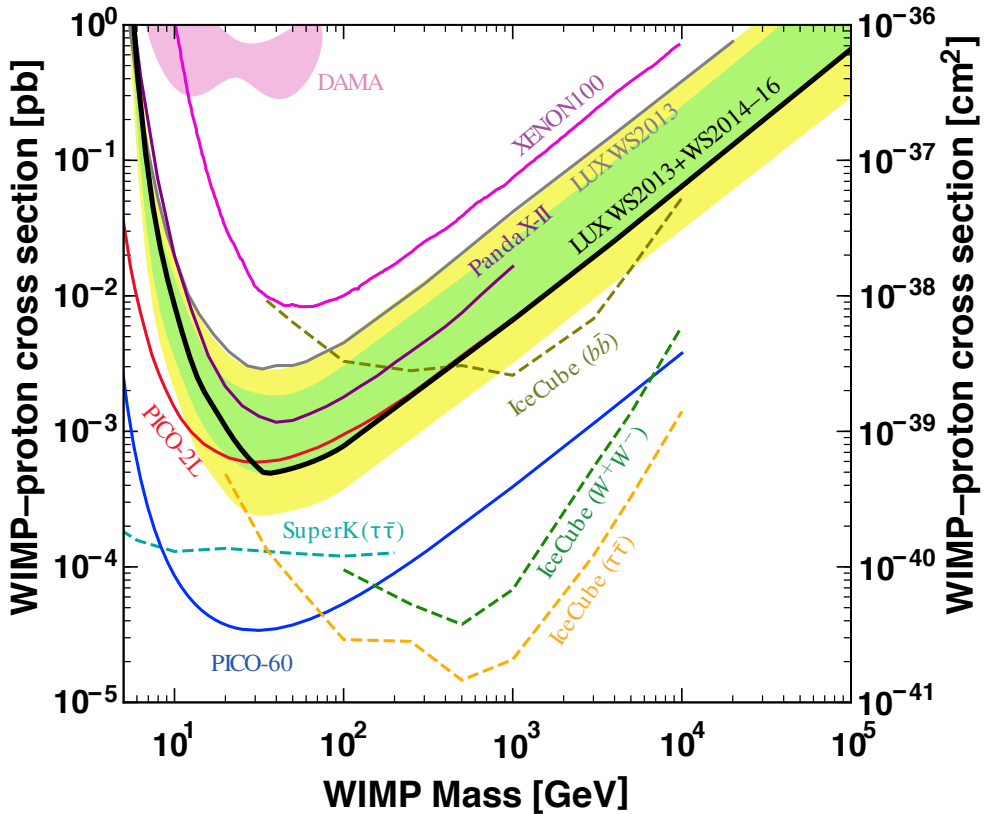

Figure 2.11: *WIMP-proton spin-dependent (SD) cross section versus the WIMP mass as recently reported by the LUX collaboration. From [81].*

Fig. 2.11 shows the results for the spin-dependent WIMP-proton cross section[1]. We can see that the spin-dependent WIMP-proton exclusion limit by the LUX collaboration is about a factor 40 worse than the WIMP-neutron one (the best exclusion is reached for a WIMP-proton spin-dependent cross section of $5 \times 10^{-40}\, \mathrm{cm^2}$ at a WIMP mass of $35\, \mathrm{GeV}$). This is a general feature of xenon-based detector because ^{129}Xe and ^{131}Xe - the two odd isotopes present in natural xenon - have an even number of protons and an odd number of neutrons. Since one neutron is unpaired, the sensitivity to spin-dependent WIMP-neutron cross section is much larger than the WIMP-proton one.

On the other hand, the PICO experiment uses ^{19}F nuclei which have an unpaired proton. Therefore, the PICO experiment is the most sensitive direct detection experiment to probe the spin-dependent WIMP-proton cross section excluding a spin-dependent WIMP-proton cross section of $3.4 \times 10^{-41}\, \mathrm{cm^2}$ at a WIMP mass of $30\, \mathrm{GeV}$ [83].

As described in section 1.5.2, indirect detection experiments are sensitive to the spin-dependent WIMP-proton cross section, The exclusion limit mainly depends on the state produced by the annihilation of WIMPs. Compared to the PICO experiment, indirect detection experiments are more sensitive for WIMPs with a mass above $100\, \mathrm{GeV}$.

2.4.1 The DAMA claim and its interpretation

The DAMA/LIBRA experiment [67] uses 25 highly radiopure thallium-doped sodium-iodide crystal scintillators. DAMA/LIBRA is sensitive only to the scintillation, so there is no discrimination between electronic and nuclear recoils. In addition, DAMA/LIBRA does not measure the location of an interaction inside a crystal, so the rejection of events near the edge of the detector, which are mostly induced by the residual radioactivity in the construction materials, is impossible. To search for WIMPs, DAMA/LIBRA defines as a possible WIMP candidate every single hit event where only one crystal records an interaction. Every multiple hit event, where more than one crystal records an interaction, is defined as background, because WIMPs are extremely unlikely to interact twice in the detector due to their minute cross section. DAMA/LIBRA claims a WIMP detection because an annual modulation in the rate of single hit events is observed. Between 1996 and 2003, the first phase DAMA/NaI experiment [84] already observed an annual modulation in the rate of single hit events.

Fig. 2.12 shows the measured rate of single hit events after subtracting the mean

---

[1]Assuming the universality of g_q, collider experiments set the same exclusion limits on the WIMP-neutron and WIMP-proton spin-dependent cross section. For clarity, the limits shown in Fig. 2.10 were omitted in this figure by [81].

value of the rate as a function of time [67]. DAMA/LIBRA and DAMA/NaI collected data for a period of about 13 years with a total exposure of $1.33 \, \text{ton} \times \text{year}$. The data shows an annual modulation in the rate of single hit events for energies between 2 and 6 keV. If the modulation is interpreted in terms of the Earth moving around the Sun causing a change in the WIMP rate, the modulation is consistent with a WIMP with $\sigma_p^{SI} = 2 \times 10^{-40} \, \text{cm}^2 \, (10^{-41} \, \text{cm}^2)$ at $m_\chi = 10 \, \text{GeV} \, (70 \, \text{GeV})$ assuming that WIMPs interact with sodium (iodine) [76]. Furthermore, the modulation is not observed in the multiple hit sample, rejecting the hypothesis that a background is artificially creating the modulation. The observed modulation by DAMA/LIBRA and DAMA/NaI has a significance larger than 9σ.
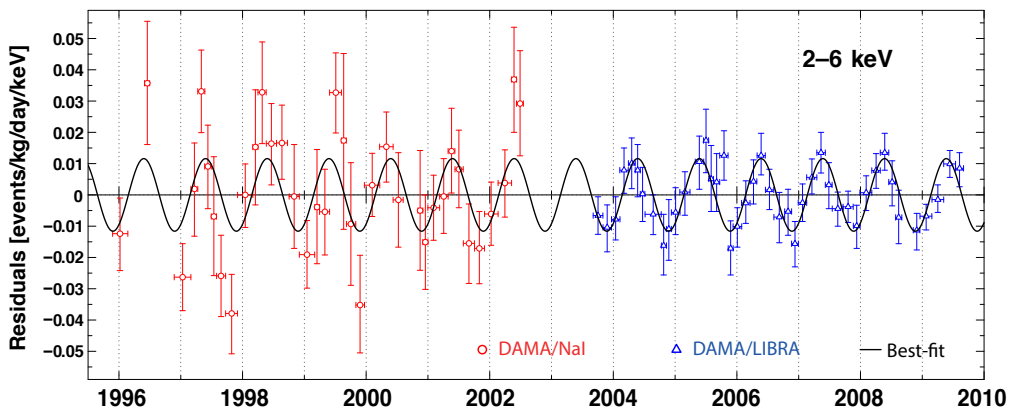
Figure 2.12: *DAMA/NaI (red points) and DAMA/LIBRA (blue points) annual modulation detection. The points are the measured rate of single hit events after subtracting the mean value of the rate (residuals, events/kg/day/keV) as a function of time. A cosine function is the best-fit to the data (black line). Figure from [59].*

However, only the DAMA/LIBRA collaboration has reported a WIMP claim, while many other collaborations exclude the DAMA/LIBRA claim. To reconcile the other WIMP experiments null results with DAMA/LIBRA, several hypotheses have been suggested. One of the assumptions is that the effective coupling of WIMPs with protons and neutrons is different [85] ($f_n \neq f_p$, section 2.2). However, given the XENON1T and LUX exclusion limits, an extreme fine tuning is needed to explain the null result in xenon experiments and an observation in DAMA/LIBRA.

The DAMA/LIBRA experiment can not distinguish between electronic and nuclear recoils. Therefore, another possibility is that WIMPs interact only with leptons (leptophilic Dark Matter), e.g. the electrons in the atom [86] [87]. In this case, if the atomic electron binding energy is smaller than the total energy deposited in the detector, then

the recoil will be completely absorbed by the atomic electron which will be kicked out of the atom to which it was bound [86]. Since an atomic electron is initially in a bound state, the electron has a fixed energy determined by the binding energy of the atomic shell. Furthermore, the electron momentum follows a distribution given by the square of the Fourier transform of the corresponding atomic shell wave function [86]. Therefore, there is a small probability that the electron has a high initial momentum [54]. In this case, keV recoil energies are possible if the electron has a momentum of order of MeVs, though it is unlikely [54].
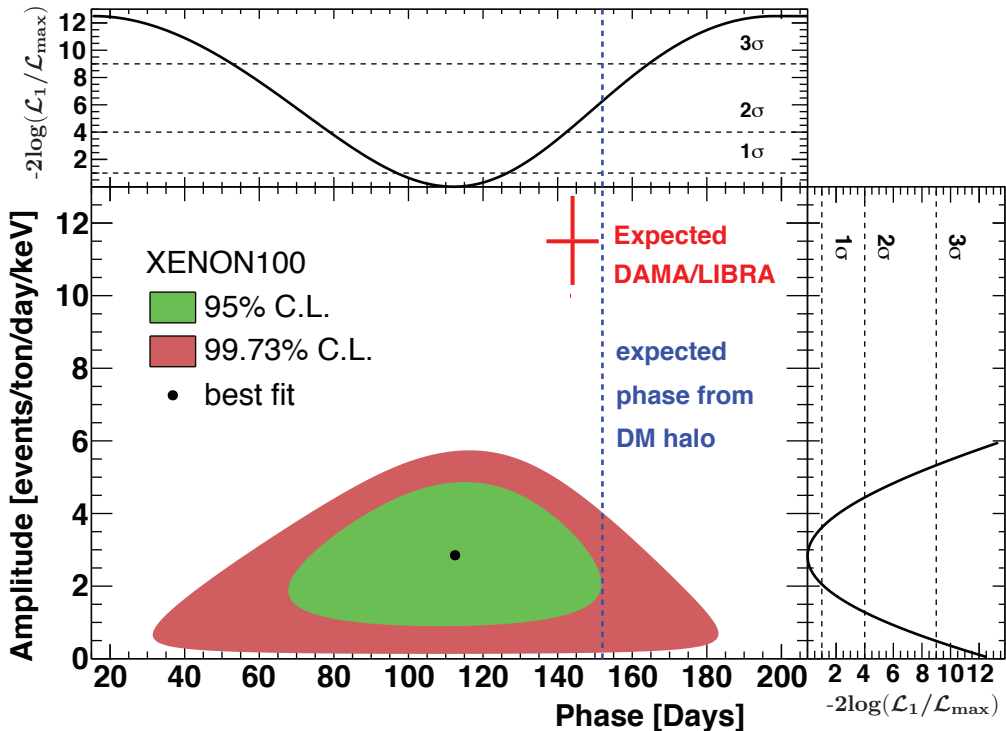
Figure 2.13: *XENON100 best fits at 95% and 99.73% confidence level of the observed modulation in the XENON100 electronic recoil data. The amplitude as events/ton/day/keV is plotted against the phase of the modulation in days. The log likelihood ratio (upper and side small boxes) is used as a test statistics to find the best fit values. The data disagree at 4.8σ level with the DAMA modulation indicated as a cross. Figure from [88].*

To study this possibility, XENON100 has looked for an event rate modulation in its electronic recoil data [88]. The electronic recoils are divided into two samples, as done in DAMA/LIBRA: single interactions, where WIMPs are eventually expected to be found, and multiple interactions, used as a background control sample [88]. Fig 2.13 shows

the results of an un-binned profile likelihood analysis for the single interaction sample. XENON100 found an annual modulation (2.8σ significance) in the electronic recoil data with a phase of 112 ± 15 days and an amplitude of 2.7 ± 0.8 events/ton/day/keV[1] [88]. The DAMA/LIBRA expected modulation (drawn as a cross) has an amplitude of about 11.5 events/ton/day/keV and a phase of about 144 days. Comparing the two modulations, XENON100 data disfavours the DAMA claim at 4.8σ significance [88]. Furthermore, the multiple interaction sample also shows a similar modulation, suggesting that backgrounds can cause the observed modulation in the single interaction sample [88].

One possible way to finally understand the DAMA/LIBRA claim is to build another DAMA-like detector in the southern hemisphere. If we observe a modulation with the same phase and amplitude, the Dark Matter origin would be the most probable hypothesis since in the southern hemisphere effects correlated with season are shifted by half a year [89]. On the other hand if we observe no modulation or a modulation with a different phase the non Dark Matter origin will be the most probable scenario.

2.5 Conclusions

In this chapter the kinematics of the WIMP interaction with a nucleus and the WIMP differential event rate have been calculated. WIMPs can be detected if we observe an excess of events compared to the estimated background. Additionally, if WIMPs are causing the excess, an annual modulation and a directional dependence of the event rate is expected due to the Earth's motion around the galactic center. Only the DAMA/LIBRA collaboration reports a WIMP observation while most other experiments exclude the WIMP claim by DAMA/LIBRA. In this thesis, we will analyse the XENON100 data with a lower energy threshold and improve the XENON100 sensitivity for WIMP masses below about $7\,\mathrm{GeV}$. In this way, we will provide another verification of the DAMA/LIBRA observation of a WIMP with a WIMP-nucleon cross section of $2 \times 10^{-40}\,\mathrm{cm}^2$ at a mass of $10\,\mathrm{GeV}$.

---

[1]The notation events/ton/day/keV is equivalent to events/(ton $\times$ day $\times$ keV).

3

The XENON100 experiment

The technology for WIMP detection with dual phase xenon Time Projection Chambers (TPC) has evolved over the past ten years, increasing the sensitivity by an order of magnitude approximately every two years. A detailed knowledge of the scintillation and ionization properties is required to use xenon as a target. Also the background contributions must be understood extremely well.

In this chapter we will describe the working principles of the XENON100 experiment. An illustration of the working principles of the XENON100 TPC is shown in Fig 3.1. The XENON100 detector uses liquid and gas xenon in a dual phase TPC. An interaction in the TPC produces scintillation photons and ionization electrons. The photons are detected within a few ns after their production by two arrays of Photo-Multiplier Tubes (PMTs) located below and above the liquid xenon target, and this signal is called S1 [90]. Electrons are drifted to the liquid-gas interface by an electric drift field. In a small volume around the liquid-gas interface an extraction electric field pulls the electrons from the liquid into the gas. After the electrons enter the gas region, proportional scintillation takes place causing a secondary scintillation signal - called S2 - that is also detected by the PMTs, albeit at a later time than the S1 signal. The detected signals are used to reconstruct the position and the energy of the interaction and to perform particle identification. Finally, the main backgrounds are described since, eventually, the sensitivity of the experiment will be dominated by the suppression and understanding of the extremely low background levels. XENON100 performed three Dark Matter searches referred in the following as Run-I, Run-II, and Run-III.
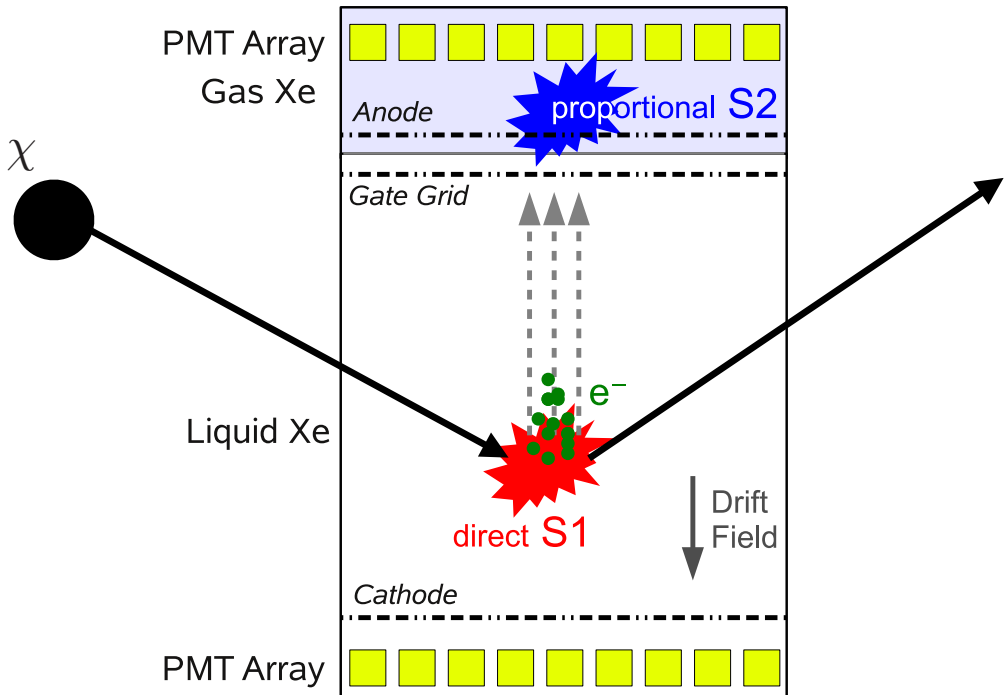
Figure 3.1: *Illustration of the working principles of the XENON100 TPC. Photons and electrons are released after the interaction of a WIMP with a xenon nucleus. Photons are detected within a few ns (S1 signal). Electrons drift to the liquid-gas interface where the extraction electric field extracts them into the gas phase. The extraction field accelerates electrons in the gas causing them to emit light, producing the so called S2 signal. From [90].*

3.1 Xenon as a detection medium

Xenon TPCs have become the most sensitive WIMP detectors for the following reasons [91]:

- WIMP-induced nuclear recoils can be distinguished from background-induced electronic recoils using the relative fraction of the S1 and the S2 signal measured for each interaction;

- External backgrounds mostly originate from the radioactivity of detector components at the edge of the xenon target. The majority of these radioactive decays will cause a signal near the edge of the xenon target, due to the short attenuation length in xenon i.e. for γ-rays and electrons. The position of the interaction can be reconstructed in three dimensions using the S1 and the S2 signal. In this

way, backgrounds towards the edge of the detector are rejected, leaving only a potential WIMP-induced signal in the central volume of the TPC (the so-called fiducial volume);

- The xenon technology is possible to scale to multi-ton masses. The PANDA-X experiment [71] is operating a xenon TPC containing about 600 kg of xenon in the sensitive volume, while the XENON1T experiment is operating a xenon TPC containing about 2000 kg of xenon;

- Natural xenon has an atomic number of 54 and a mean atomic mass number of 131.3. Compared to detectors which use lighter noble gases, xenon-based detectors have the major advantage that the WIMP-nucleus spin-independent cross section scales as A^2. Therefore, relatively low target masses are required to probe the same WIMP-nucleon cross section;

- Natural xenon contains a substantial fraction of odd-isotopes like ^{129}Xe ($J = 1/2$) and ^{131}Xe ($J = 3/2$), which enhance the sensitivity for the spin-dependent WIMP-nucleus scattering because they have a non-zero angular momentum.

Table 3.1: *Properties of xenon [92] [93] [74].*

Atomic number	54
Isotopes	^{124}Xe (0.09%), ^{126}Xe (0.09%), ^{128}Xe (1.92%), ^{129}Xe (26.44%), ^{130}Xe (4.08%), ^{131}Xe (21.18%), ^{132}Xe (26.89%), ^{134}Xe (10.44%), ^{136}Xe (8.87%)
Mean atomic mass number	131.3 g/mol
Liquid xenon temperature (XENON100)	182.5 K
Liquid xenon density at 182.5 K	2.8 g/cm^3
W value	13.7 ± 0.2 eV
Scintillation wavelength	178 nm
Singlet decay time	3.1 ± 0.7 ns
Triplet decay time	24.0 ± 1.0 ns

Table 3.1 summarizes the most important properties of xenon as a detection medium. Natural xenon contains different isotopes. The xenon isotopes are not radioactive with the notable exception of ^{136}Xe. ^{136}Xe exhibits double β decay to ^{136}Ba [94], inducing a

negligible electronic recoil background in XENON100 as we will show in section 3.7.1. [136]Xe can also be used to look for the neutrinoless double beta decay, which is predicted by theories beyond the standard model.
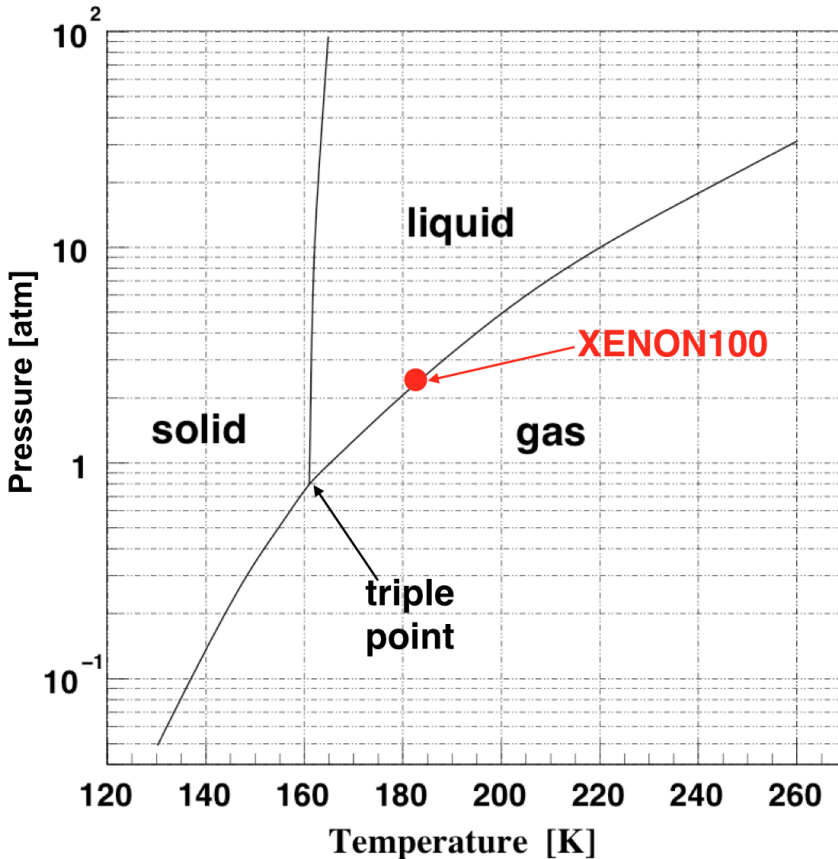
Figure 3.2: *Xenon phase diagram. In XENON100, the liquid xenon is kept at a temperature of 182.5 K and a pressure of 2.2 atm. Figure adapted from [93].*

Fig. 3.2 shows the phase diagram of xenon that indicates the values of the temperature and pressure at which the solid, liquid and gas xenon phases occur. The triple point is at a temperature of 161.3 K and at a pressure of 0.8 atm. In XENON100, the xenon is kept liquid at a temperature of 182.5 K, while the xenon vapour pressure is 2.2 atm. The liquid xenon density is $2.8 \, \text{g/cm}^3$ at 182.5 K. The mean energy (W value) required to create either an excited atom or an electron-ion pair is $13.7 \pm 0.2 \, \text{eV}$ [95]. The scintillation light spectrum has its peak in the ultraviolet electromagnetic region at 178 nm, and xenon is reasonably transparent to its scintillation light. The charac-

teristic decay times of the excited xenon molecules are about 3.1 ± 0.7 ns (singlet) and 24.0 ± 1.0 ns (triplet) [74].

3.1.1 Scintillation and ionization

Fig. 3.3 shows a cartoon of the creation of light, charge and heat after an incoming particle interacts with xenon. The recoil energy induced by an incoming particle is used for the production of a certain number of electron-ion pairs and excited atoms or molecules (excitons) [93]. A part of the recoil energy is also dissipated into heat which can not be detected in a xenon TPC[1].

The excited atoms Xe^* can form excited diatomic molecules Xe_2^* (excimers), when they combine with neutral atoms. Then, when the excimers decay, they produce scintillation light with a characteristic wavelength of 178 nm [91]. Xe_2^* can occupy a singlet or a triplet state, and decays to the ground state with two different decay times[2].

The recoil energy induced by the incoming particle also produces electrons and ionized atoms. Using an external electric drift field, a fraction of the electrons can be extracted from the interaction point producing the S2 signal. The Xe^+ ions can form charged molecules, Xe_2^+, when they combine with neutral atoms. In this way, Xe_2^+ and electrons, which are not extracted from the interaction point, can recombine. As a result, excimers are formed and their decay produces scintillation light as described above. Both the directly created excimers and the excimers produced by the recombination of electrons will contribute to the S1 signal.

---

[1]Here we present a simplified description, omitting some of the intermediate steps which lead to the creation of scintillation light. The complete description can be found for example in [92].

[2]As reported in section 2.3, the singlet and triplet decay time are, respectively, 7 ns and 1600 ns for argon.
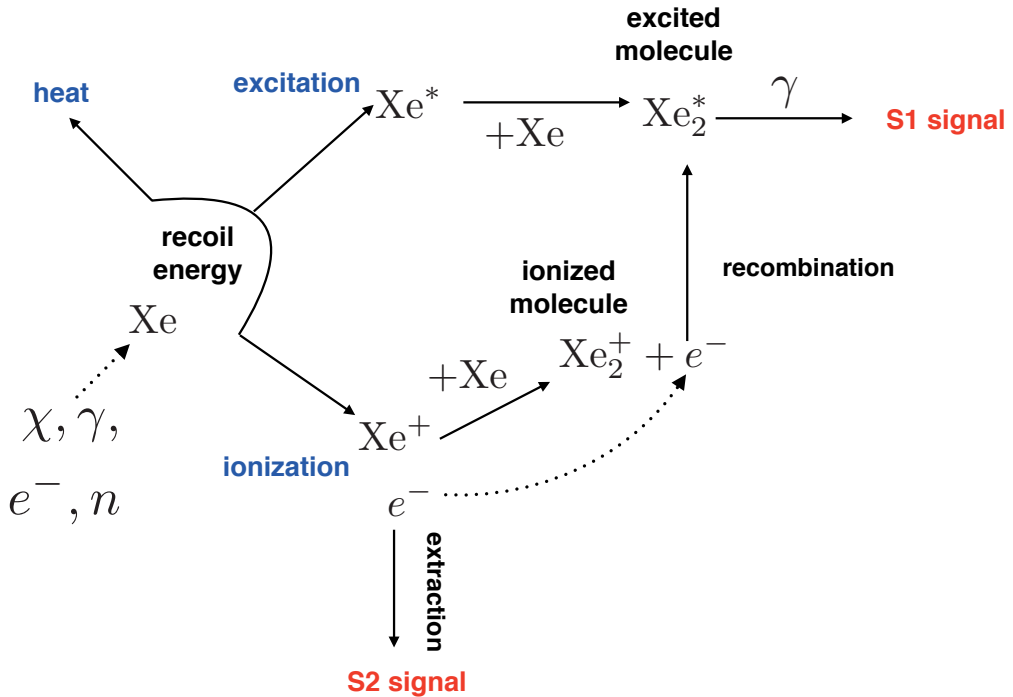
Figure 3.3: *Schematic cartoon of the production of the* S1, S2 *signal and heat in xenon. The recoil energy induced by an incoming particle, e.g.* χ, γ, e^-, n *causes the production of excited molecules, which decay generating scintillation light, and electrons, which can be extracted from the interaction point using an external electric drift field. If the electrons are extracted they can be detected (* S2 *signal). Some electrons will recombine with ionized molecules, and subsequently they produce excited molecules that will decay and produce scintillation light. Both the excited molecules created by the interaction of the particle and by the recombination of electrons contribute to the* S1 *signal. Also heat is produced, but it can not be detected in a xenon TPC.*

3.2 The XENON100 detector

Fig. 3.4 shows a schematic drawing of the XENON100 TPC. The TPC is almost cylindrical with a radius of 15.3 cm and a height of 30.5 cm, and it contains 62 kg of liquid xenon [90]. The TPC is instrumented with two arrays of Hamamatsu R8520-06-Al $1 \times$ inch^2 PMTs located below and above the liquid xenon target. 98 PMTs are placed in the top array arranged in concentric circles to establish a good radial resolution [90]. 80 PMTs are placed in the bottom array, and they are arranged in a dense packing to achieve a high light collection [90].
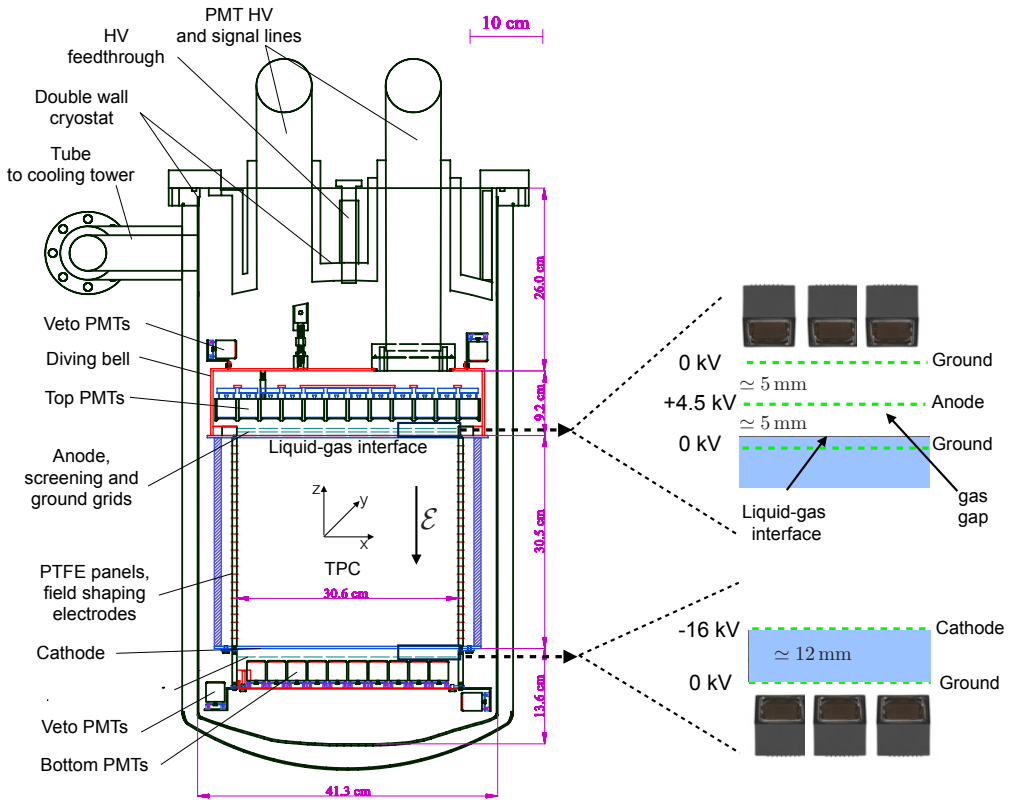
Figure 3.4: *Schematic drawing of the XENON100 detector with a zoom of the electric field configuration. Figure adapted from [90].*

A picture of the bottom and top PMT array is shown in Fig. 3.5, clearly showing the different PMT arrangements. The TPC is mounted in a double-walled stainless steel cryostat constructed from materials with very low radioactive contamination. The TPC is separated from an active liquid xenon veto shield using a wall made of 24 PTFE[1] panels, as indicated in Fig. 3.4. PTFE is a good electrical insulator and reflector of the scintillation light [96], enhancing the light collection efficiency. The liquid xenon veto is about 4 cm thick, it contains 99 kg of xenon, and it is instrumented with 64 PMTs - 32 in the outer layer of the top PMT array and 32 in the outer layer of the bottom PMT array -. The veto is used to reject background events with both an interaction in the veto volume and in the TPC volume, e.g. a neutron that scatters once in the veto and once in the TPC.

---

[1]Polytetrafluoroethylene (teflon).

Bottom PMT array
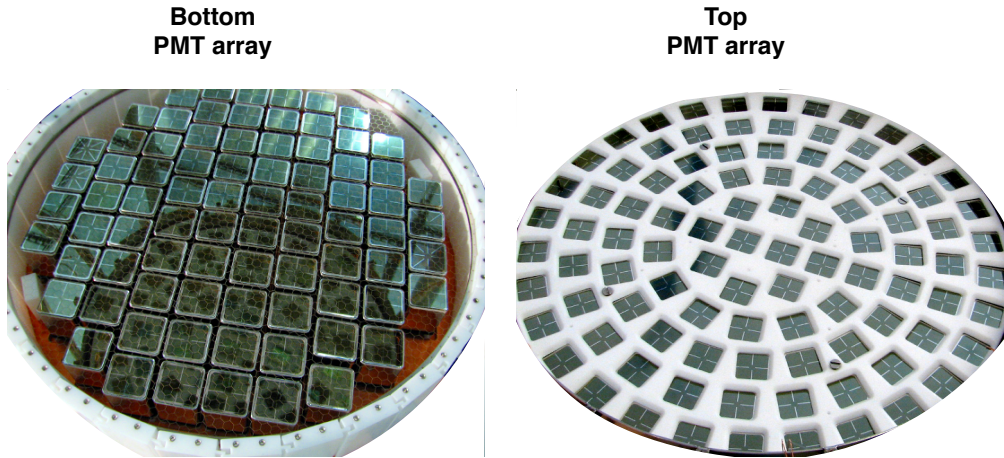
Top PMT array

Figure 3.5: *Pictures of the top and bottom PMT arrays. From [90].*

In Runs-I and II, an electric drift field ($\mathcal{E}$) of $0.53\,\text{kV/cm}$ is created by a cathode at -16 kV, a stainless steel ground grid placed approximately at the liquid-gas interface and field shaping electrodes, as shown in Fig. 3.4. In Run-III the cathode voltage was slightly lowered to -15 kV resulting in an electric drift field of $0.5\,\text{kV/cm}$. Electronegative impurities, e.g. oxygen and water vapour [97], are kept at the sub-ppm (part per million) level to avoid the capture of electrons during their drift. An anode at $4.5\,\text{kV}$ is placed 5.0 mm above the ground grid. The anode and the ground grid create the so-called extraction field of about $11\,\text{kV/cm}$. Two additional ground grids, one placed 5 mm above the bottom PMT array (12 mm below the cathode) and one placed 5.0 mm above the anode, are used to shield both the bottom and the top PMT array from the cathode and the anode high voltage, as shown in Fig. 3.4. The gas gap (Fig. 3.4) is precisely controlled using a diving bell design to achieve a uniform response to electrons that are accelerated in the gas phase [90].

A passive shield consisting of (from outside to inside) 20 cm of water, 25 cm of polyethylene, 20 cm of lead, 20 cm of polyethylene and 5 cm of OFHC[1] copper surrounds the detector [90] (Fig. 3.6). Polyethylene and water are used to thermalize and stop neutrons while lead and copper are used as a shield against γ-rays.

Fig. 3.7 shows a sketch of the cooling system used to liquefy the xenon and to keep the xenon liquid at a temperature of $182.5\,\text{K}$. [97]. A Pulse Tube Refrigerator (PTR) is mounted on a copper block, which closes the inner cryostat vessel and acts as a cold finger [90]. Electrical heaters, which are placed between the PTR and the

---

[1]Oxygen-Free High thermal Conductivity.

cold finger, regulate the temperature of the cold finger, thereby determining a xenon vapour pressure of 2.2 atm in the detector. A vacuum insulated pipe connects the cooling system to the main cryostat. The xenon gas from the detector reaches the cold finger where it is liquefied [90]. Then, a funnel collects the liquid drops that flow back in the detector through a small pipe. In case of a failure of the cooling system, liquid nitrogen can flow through a stainless steel coil wound around the cold finger, acting as an emergency cooling system capable to run for 48 hours.
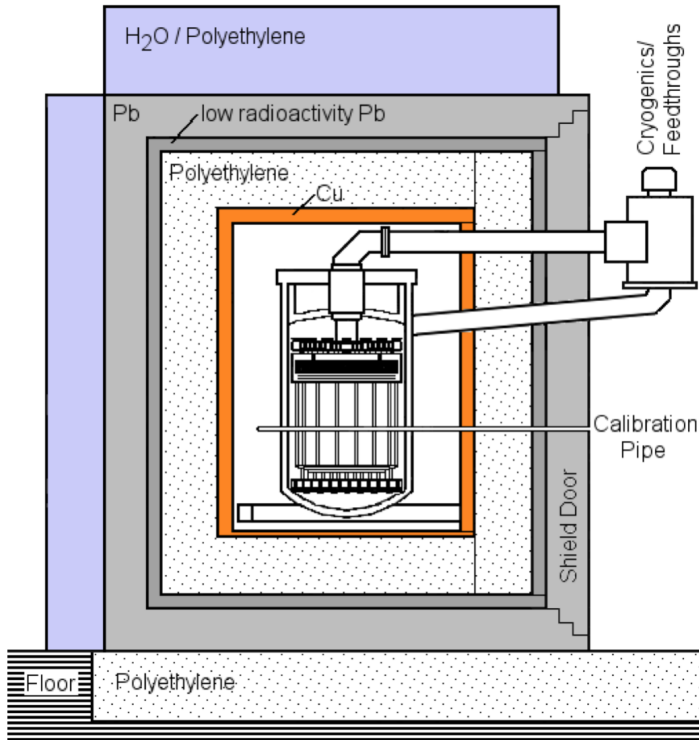
Figure 3.6: *A sketch of the XENON100 detector inside its shield. From outside to inside water, polyethylene, lead, polyethylene and copper are used to shield against unwanted interactions of neutrons and γ-rays. From [90].*
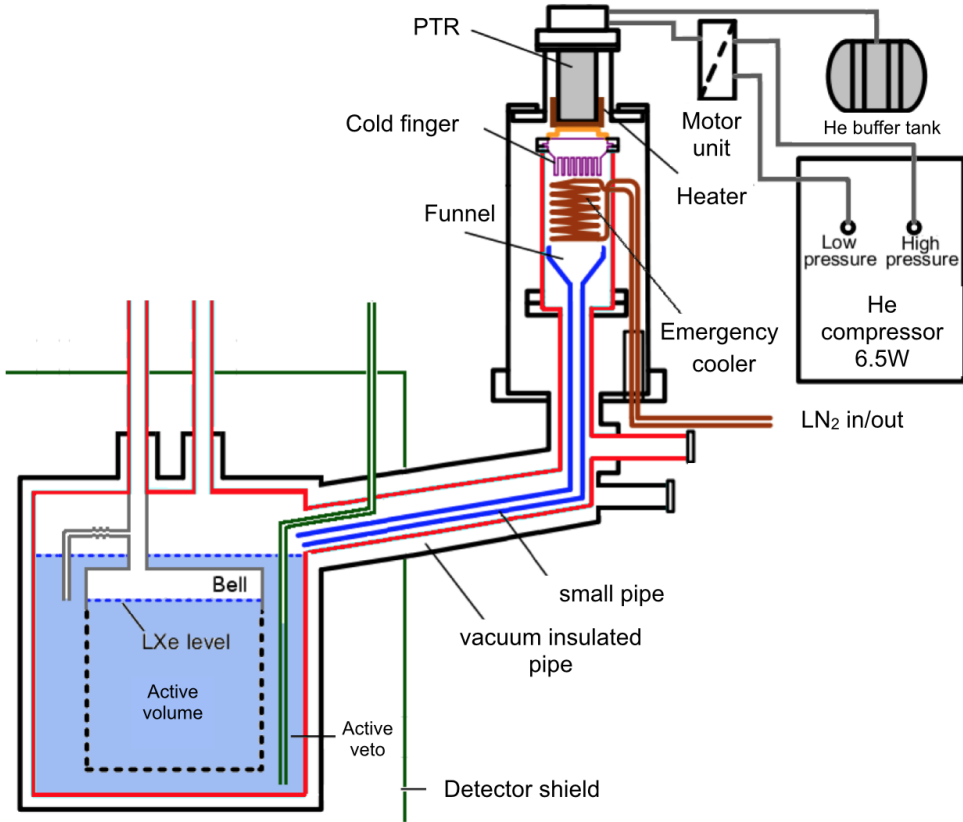
Figure 3.7: *Sketch of the XENON100 cooling system. From [90].*

3.2.1 Data acquisition system and the data processing

The goal of the XENON100 Data AcQuisition (DAQ) system is to record the traces[1] from the PMTs (waveform) as they develop in time. Fig. 3.8 shows the DAQ system, which is subdivided into three subsystems: the trigger, the waveform acquisition, and the rate and time accounting [98].

The raw 242 PMT signals are amplified by a factor of 10 using 16 Phillips 776 NIM amplifiers [90]. The output is digitized by 31 CAEN V1724 flash ADCs with eight input channels, 10 ns sampling period, 14 bit resolution, 2.25 V full scale. Each flash ADC has also a circular buffer of 512 kByte memory per channel [90]. In parallel the signal is used for the trigger generation. In Run-I, the signals from 68 inner PMTs of the top PMT array and 16 PMTs in the center of the bottom PMT array are summed

---

[1]The digital sampling of the output of the PMTs every 10 ns.

using linear FAN-IN/FAN-OUT modules. Since the FAN-IN/FAN-OUT modules have a total of 84 input channels, these PMTs are selected because they provide an optimal area coverage of the TPC. In this way, XENON100 can trigger on small S2 signals down to a size of about 300 photoelectrons[1] (PE).
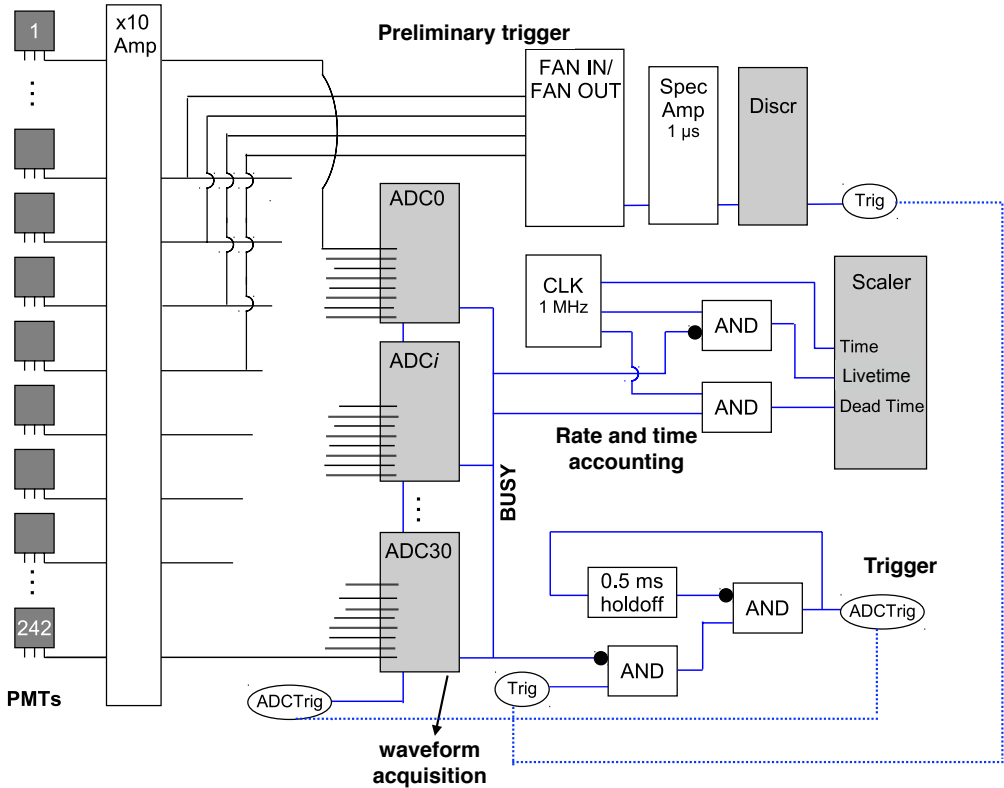
Figure 3.8: *Schematic of the XENON100 data acquisition system. Figure adapted from [90].*

The summed signal is then amplified, integrated, and shaped with a spectroscopy amplifier [90]. Finally, the integrated signal is discriminated using a low threshold discriminator, and it constitutes the preliminary trigger signal (Trig in Fig. 3.8) [98]. This trigger signal and a logic signal, which indicates if the flash ADCs are busy, are combined into an AND gate. Then, the AND of the these two signals is combined into another AND gate with a holdoff logic signal, which prevents overlaps between events for 0.5 ms.

The resulting logic signal from the previous AND is the trigger (ADCTrig in Fig.

---

[1]It is a common practice in the field to report the area (size) of the S1 and the S2 signal in terms of the photoelectrons which initiate the secondary emission in the PMT.

3.8), which is distributed simultaneously to the 31 flash ACDs [98]. When the flash ADCs receive the trigger, the data is recorded, and the waveform of the event is acquired. The waveform of each event is digitized $200\,\mu s$ after the trigger and also $200\,\mu s$ before the trigger retrieving the data already digitized in the ADC circular buffer. The trigger is therefore positioned at the middle of the waveform. The maximum drift time is about $176\,\mu s$ [90] which is well below the $400\,\mu s$ digitization window. The flash ADCs are operated using an on-board FPGA in a mode, called zero length encoding, to record only part of a waveform, where a signal exceeds $0.3\,PE$ [90]. In this way, the size of the data are reduced by about a factor of 10, because large parts of the waveforms consist of noise around the baseline [90].

The rate and time accounting subsystem measures the time, the livetime and the dead time [98]. A clock module generates a logic signal at a frequency of 1 MHz [98], which gives the time. The clock signal is combined with the BUSY signal of the ADCs to calculate the dead time, while the trigger holdoff deadtime is taken into account separately. The resulting deadtime in the Dark Matter Runs is about 1% [90]. The complement of the BUSY signal and the clock signal gives the livetime (see Table 4.1 for the livetime during Run-I, Run-II and Run-III).
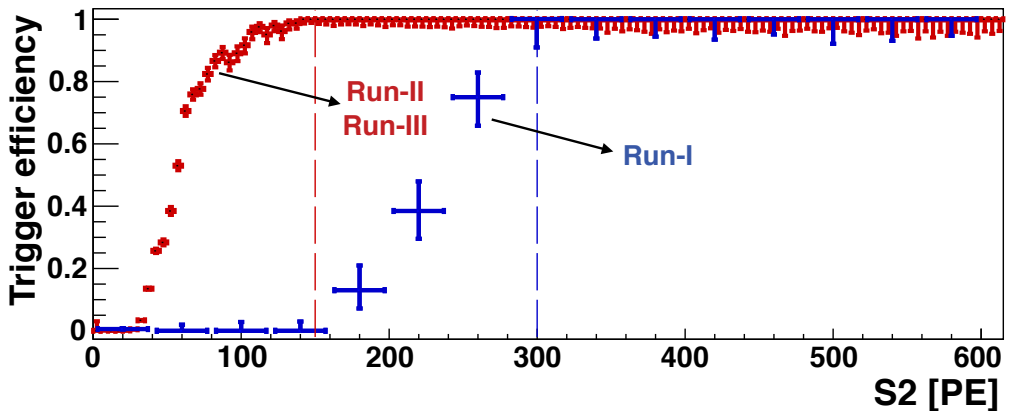
Figure 3.9: *Trigger efficiency versus the* S2 *signal. The trigger efficiency is 100% at 300 PE for Run-I (blue points) while for Run-II and Run-III (red points) is 100% at 150 PE. From [99].*

In Run-II and Run-III the preliminary trigger logic signal was improved. Instead of summing 68 PMTs in the top PMT array and 16 PMTs in the bottom PMT array, a majority trigger mode was used: every PMT in the TPC exceeding about $0.5\,PE$ issued a voltage pulse of $125\,mV$ [99]. Then, the sum of these voltage pulses are amplified, integrated, and shaped as in Run-I. In this way, in Run-II and Run-III S2 signals with

a size larger than 150 PE have a 100% probability to produce a trigger in the detector. In Run-I, S2 signals with a size of about 150 PE have only a 10% probability to produce a trigger in the detector, while the trigger probability is 100% for S2 signals with a size larger than 300 PE, as shown in Fig. 3.9. The 100% trigger efficiency S2 value is used as the S2 signal threshold to analyze the data in each Dark Matter Run.

3.2.2 Data Processing

A XENON100 event is constituted by the waveforms of the 242 PMTs of $400\,\mu s$ length [90] sampled every 10 ns. The physical parameters of the interaction inside the TPC are calculated from the raw data using the XENON100 data processor, called xerawdp. The following three processing steps are executed [98]:

- **Preprocessing:** the baseline of each PMT waveform is computed and the individual PMT waveforms are converted from ADC counts to volts. The individual waveforms are then added into a summed waveform to search for the S1 and S2 peaks.

- **Peak finding:** Fig. 3.10 shows a cartoon of the peak finding algorithms implemented in xerawdp. A main S2 peak is identified if xerawdp finds regions where a signal exceeds a threshold of 10 mV above the baseline for at least $0.6\,\mu s$ [98], which is smaller than the typical $2\,\mu s$ time extent of an S2 signal determined by the diffusion of electrons in liquid xenon and the proportional scintillation in the gas phase. Xerawdp looks for S2 signals in the summed waveform of all PMTs, and it identifies the S1 signals that should have preceded in time the S2 signals. A digital filter is applied to smooth out the high frequency components and to facilitate the detection of the extent of the S2 peaks.

  An S1 peak is identified if a signal occurs before the main S2 signal and exceeds a threshold of 3 mV above the baseline for not more than $0.6\,\mu s$, which is larger than the typical $0.1\,\mu s$ time extent of an S1 signal. The S1 peak time boundaries are defined as the positions where the S1 signal drops below 0.5% of its maximum for more than 20 ns [98]. The S1 peaks are ordered based on the number of PMTs that detected them: the S1 signal which is detected by the largest number of PMTs in the event is paired with the main S2 signal, and these S1 and the S2 signals are used to search for WIMP interactions.

- **Pulse shape analysis:** the number of PMTs that contributed to the S1 and the S2 signal, the S1 and S2 signal size, the S1 and S2 signal pulse width at 10% peak

height and at 50% peak height are determined using the information available in every PMT.
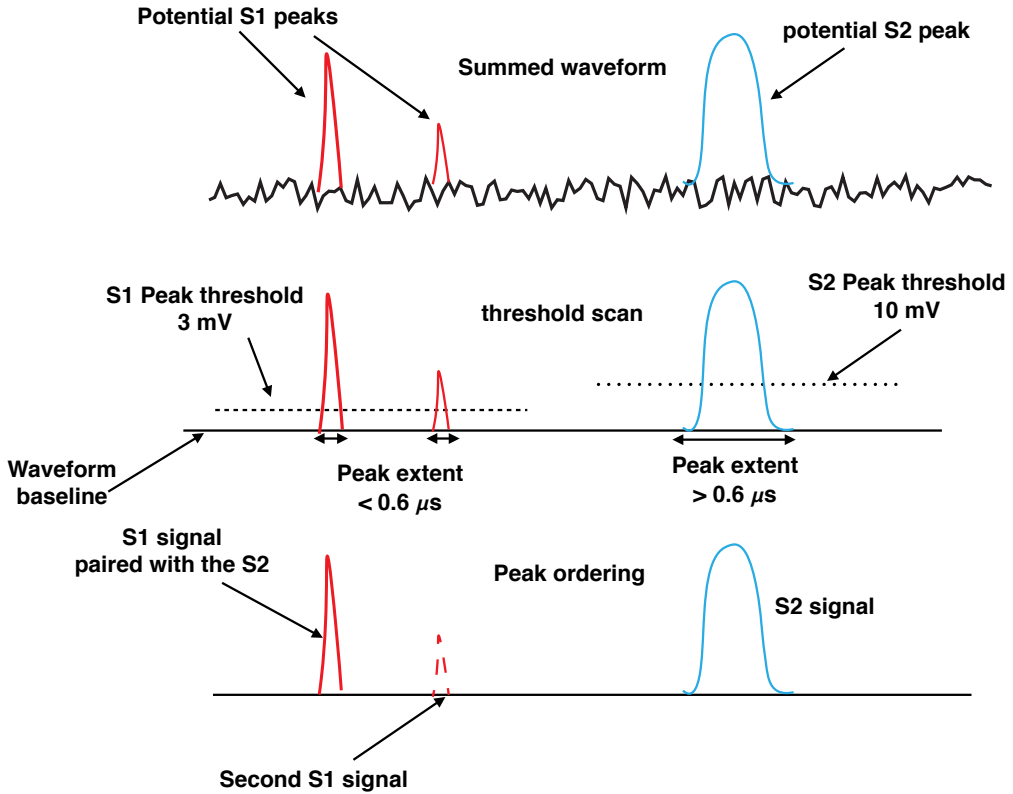
Figure 3.10: *Cartoon of the S2 and S1 peak finding algorithms.*

3.3 S1 and S2 signal and position reconstruction

For a typical low-energy event, the S1, the S2 signal and their light distribution in the top and bottom PMT array are shown in Fig. 3.11 and Fig. 3.12.

Fig. 3.11 shows the S1 and the S2 signal and their positions in the waveform. The S1 signal is a narrow peak with a width of about $0.1\,\mu s$ due to the rapid deexcitation of excitons. Instead, the S2 signal is about $2\,\mu s$ wide due to the combination of the diffusion of electrons in liquid xenon and the proportional scintillation in the gas phase. As shown in Fig. 3.11, the depth of the interaction can be inferred from the time difference (Δt) between the S1 signal and the S2 signal. The z position is given by: z

$= \int v_d \, dt \simeq v_d \times \Delta t$, where v_d is the electron drift velocity in liquid xenon ($v_d = 1.73$ mm/μs [90]).
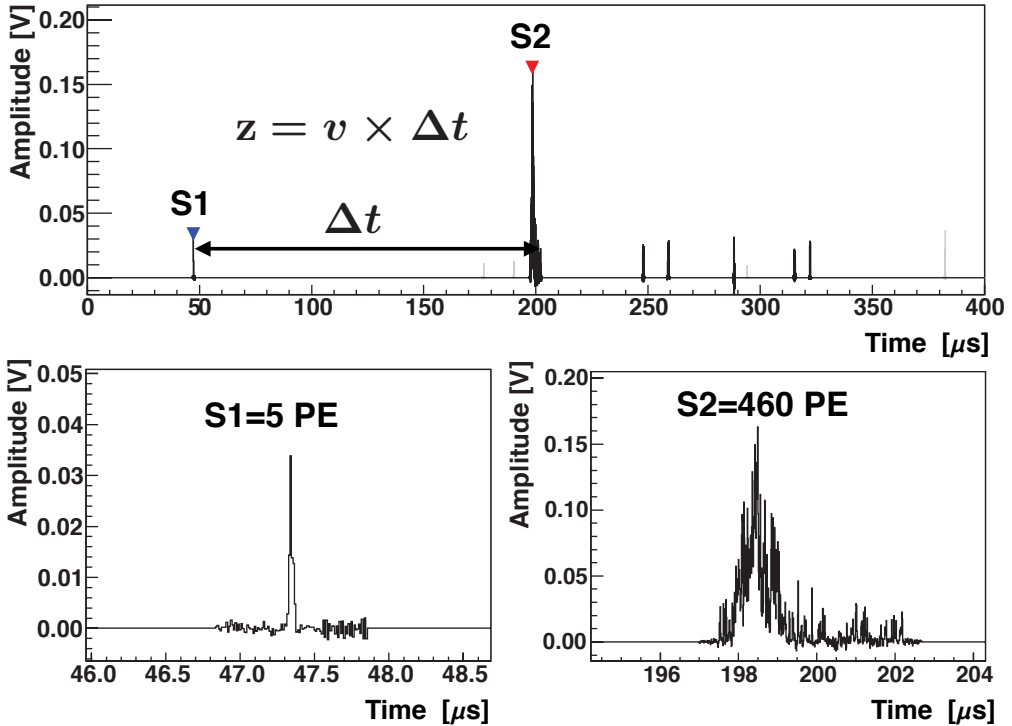
Figure 3.11: *An example of an* S1 *and an* S2 *signal for a typical low-energy event recorded by XENON100. The time difference between the* S1 *and the* S2 *signal allows the reconstruction of the z position of the interaction. Figure adapted from [90].*

Fig. 3.12 shows the S1 and S2 light distribution in the top and bottom PMT arrays for the low-energy event in Fig. 3.11. On average, about 80% of the S1 signal is detected by the bottom PMT array because of the total internal reflection at the liquid-gas interface, which is caused by the relatively large refraction index of liquid xenon (1.69 ± 0.02) compared to gas xenon (about 1), and because of the larger optical transparency of the cathode plus screening grid above the bottom PMT array (83.4%) compared to the optical transparency of the anode plus screening grids below the top PMT array (47.7%) [90]. For this reason, the PMTs with a larger Quantum Efficiency (QE) are selected for the bottom PMT array to increase the S1 light detection efficiency. The QE is on average 32% for the bottom PMT array and 24% for the top PMT array. In this particular case, the S1 signal is only detected by the bottom PMT array.

For the S2 signal, the top PMT array detects most of the secondary scintillation light, since the photons are created close to the top PMT array. The S2 light in the top PMT array is localized and allows the reconstruction of the x-y position of the interaction: a neural network algorithm compares the observed light distribution with the training samples of known vertex locations [90]. Instead, the fraction of the S2 light detected by the bottom PMT array is almost uniformly distributed, as expected for a relatively large amount of photons generated in the gas phase which will then spread almost uniformly in the bottom PMT array.
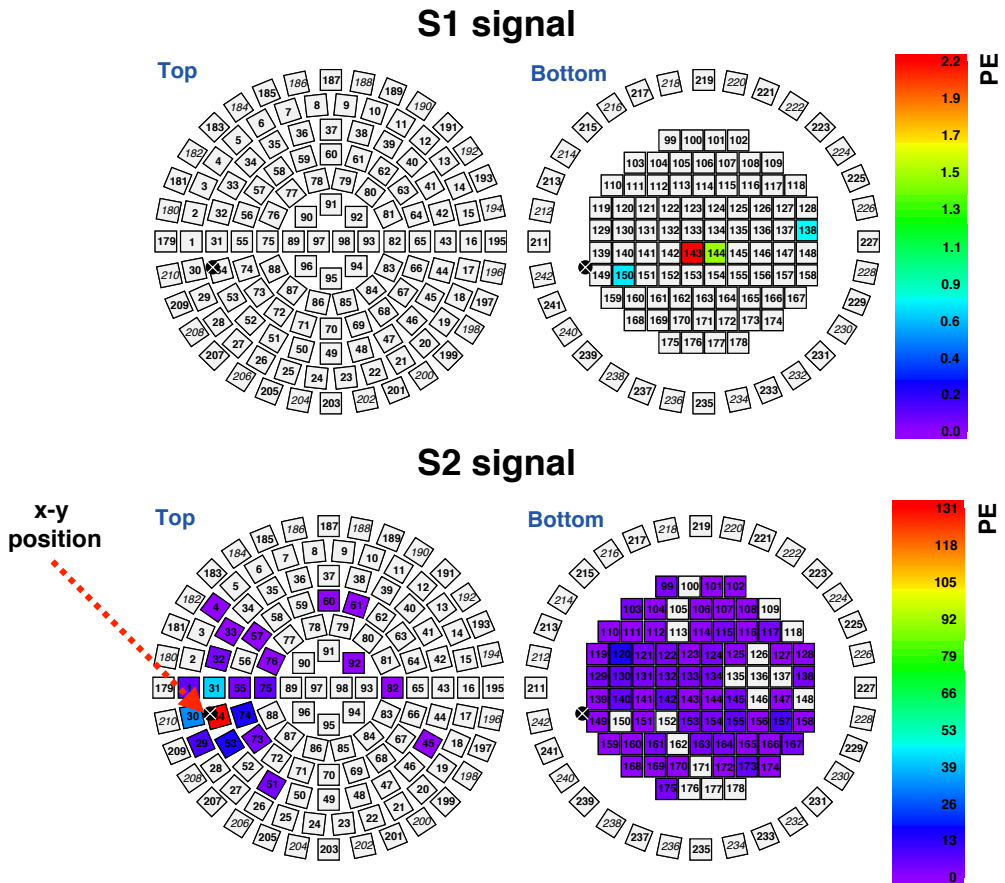
Figure 3.12: S1 *and* S2 *light distribution in the top and bottom PMT array. The* S1 *is completely detected by the bottom PMT array, while the majority of the* S2 *is detected by the top PMT array. The localized* S2 *light pattern in the top PMT array allows the reconstruction of the x-y position of the interaction. Figure adapted from [90].*

3.4 General principles of energy calibration in a xenon TPC

The recoil energy induced by an incoming particle is a crucial parameter in studying the WIMP hypothesis. The recoil energy (E_R) in xenon can be estimated from the scintillation light and ionization[1] as [95]:

$$E_R = N_{ex}W_{ex} + N_i W_i \,. \tag{3.1}$$

Where W_i is the required energy - work function - to produce an electron-ion pair, N_i is the number of electron-ions pairs produced by the interaction of the incoming particle, W_{ex} is the work function to produce an exciton, and N_{ex} is the number of excitons produced by the interaction of the incoming particle. To measure the recoil energy, we need to know W_{ex} and W_i, and the number of initially created excitons and electron-ion pairs, as well. We define the ratio between excitons and electron-ion pairs as $\alpha = N_{ex}/N_i$, and we rewrite equation 3.1 as:

$$E_R = (N_i + N_{ex})\frac{\alpha W_{ex} + W_i}{1 + \alpha} \,. \tag{3.2}$$

An approximation often used in the literature is to define a unique work function, $W = \dfrac{\alpha W_{ex} + W_i}{1 + \alpha}$ [95]. Reference [95] shows that this approximation is as effective as defining two separate W values to calculate the recoil energy in xenon [95]. The assumption here is that a larger W_{ex} is eventually counterbalanced by a lower W_i and viceversa leaving the total number of quanta $N_{ex} + N_i$ unchanged. Similarly, a higher value of α could be compensated by a lower value of W_{ex} and viceversa. Therefore, the recoil energy (E_R) in xenon is rewritten as [95]:

$$E_R = W(N_{ex} + N_i) \,. \tag{3.3}$$

$W = 13.7 \pm 0.2 \, \text{eV}$ [100] is defined as the mean weighted energy required to create either an exciton or an electron-ion pair.

Then, we need to relate the number of excitons and electron-ion pairs to the observable quantities. As described in section 3.1.1, excitons can be directly created by the interaction of the incoming particle or indirectly by the recombination of electrons and charged molecules. Defining r as the recombination probability of electrons, with

---

[1]Here, we use a simplified version of the energy balance equation where the heat is neglected as in [95]. We will see later that this assumption holds for electronic recoils. For nuclear recoils an additional term is needed to account that a non-negligible fraction of the recoil energy is dissipated into heat.

$0 \leq r \leq 1$, the total number of excitons N'_{ex} is [100]:

$$N'_{ex} = N_{ex} + rN_i . \tag{3.4}$$

Where N_{ex} is the immediately produced number of excitons, and rN_i is the number of electron-ion pairs that recombine. For simplicity, we assume that the excitons emit a photon with 100% efficiency[1], and we have:

$$n_\gamma = N'_{ex}, \tag{3.5}$$

where n_γ is the produced number of photons both from directly and indirectly created excitons. Complementary, the extracted number of electrons, n_e, is expressed as [100]:

$$n_e = (1 - r)N_i . \tag{3.6}$$

Using equation 3.6, 3.4 and 3.5, equation 3.3 is rewritten as:

$$E_R = W(n_\gamma + n_e). \tag{3.7}$$

It has to be noted that the number of electrons is anti-correlated with the number of photons. Therefore, the most precise reconstruction of E_R relies on detecting both n_γ and n_e.

Then, the number of photons and electrons must be related to the S1 and the S2 signal. We define the factor g_1 as the detector dependent effect which expresses the relation between the produced photons and the detected number of photoelectrons for the S1 signal. Similarly, g_2 is the detector dependent effect which relates the produced number of electrons with the detected number of photoelectrons for the S2 signal. Therefore, equation 3.7 is rewritten in terms of the measurable signals as:

$$E_R = W(\frac{S1}{g_1} + \frac{S2}{g_2}) . \tag{3.8}$$

Equation 3.8 is currently used by the LUX [57] and the XENON1T [75] collaborations to determine the recoil energy. XENON100 uses a simplified method where only the S1 or the S2 signal is used to reconstruct the nuclear recoil energy scale, as will be described in section 3.5.

Finally, the response of xenon to a nuclear recoil or an electronic recoil is substantially different. Fig. 3.13 shows a cartoon of the response to nuclear and electronic

---

[1]If the efficiency is different from 100%, then the reduction in the number of produced photons can be incorporated in the term g_1 which will be introduced below.

recoil. In case of an electronic recoil, ionization and scintillation are the dominant energy dissipation mechanism. Instead, for a nuclear recoil, the nucleus additionally loses energy via elastic collisions with other nuclei [98]. These collisions increase the kinetic energy of the xenon nuclei in the medium resulting in a production of heat, which can not be detected in a xenon TPC. Therefore, the heat signal is larger in nuclear recoils compared to electronic recoils. For this reason, xenon-based experiments introduce two different energy scales: the electronic recoil equivalent energy scale (E_{ee}) and the nuclear recoil equivalent energy scale (E_{nr}).
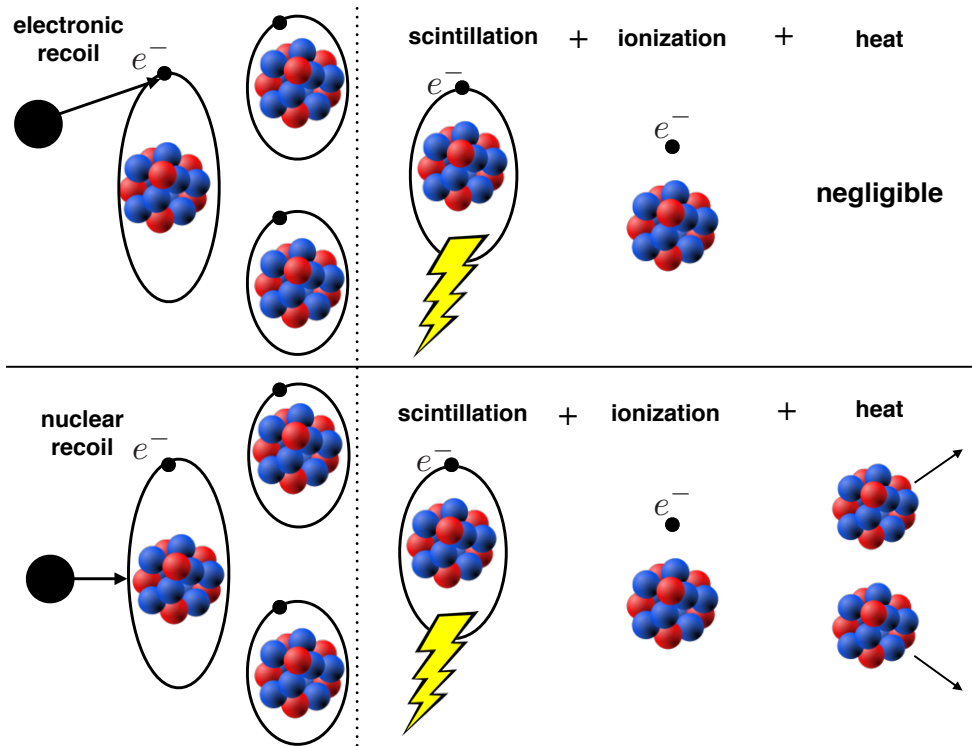
Figure 3.13: *A cartoon of the response of xenon to electronic and nuclear recoils. For electronic recoils the dominant energy dissipation mechanisms are scintillation and ionization. For nuclear recoils, also heat is relevant due to the fact that the nucleus can additionally lose energy through elastic collisions with other nuclei.*

The nuclear recoil equivalent energy scale is quenched with respect to the electronic recoil equivalent energy scale by an energy-dependent factor $\mathcal{L}(E_{nr})$ known as the Lindhard factor [101]: if a nuclear recoil and an electronic recoil have the same energy, the number of observable quanta is reduced by a factor $\mathcal{L}(E_{nr})$ in the case of a nuclear

recoil, due to the heat losses. The nuclear and the electronic recoil equivalent energy scale will be further described using the XENON100 approach in section 3.5.

3.5 Energy calibration in XENON100

In the previous section we described the state of the art for the determination of the recoil energy in a xenon-based TPC. This was based on using both the S1 and S2 signals to make a combined estimate of the energy. However, XENON100 uses a simpler model using each signal on its own. Broadly, the S1 signal energy reconstruction is used to target relatively higher mass WIMPs as in chapter 4. The S2 signal energy reconstruction is used to target relatively lower mass WIMPs as in chapter 5. The advantage of the approach of using individual rather than combined signals is a relative lack of systematic uncertainty in the correlation between S1 and S2 signals. The disadvantage is a relatively poorer energy resolution. Here, we outline the individual signals method following [99].

3.5.1 Generation of the S1 and the S2 signals

As described above, the S1 and the S2 are light signals which are detected by the top and bottom PMT array.

For the S1 signal, the expectation value on an individual PMT in units of PE is expressed as [99]:

$$\mathrm{S1}_{\mathrm{PMT}} = n_\gamma(E_R, \mathcal{E})\Gamma_{\mathrm{PMT}}(\mathrm{r,z})\eta_{\mathrm{PMT}} \equiv n_\gamma(E_R, \mathcal{E})\gamma_{\mathrm{PMT}}(\mathrm{r,z}) \,. \tag{3.9}$$

Here, $\mathrm{S1}_{\mathrm{PMT}}$ is the S1 signal detected by an individual PMT. n_γ is the number of produced photons which depends on the recoil energy (E_R) and on the electric drift field due to the recombination of electrons and charge molecules (section 3.4). Γ_{PMT} is the probability that a photon produced at the position $(\mathrm{r,z})$[1] reaches the photocathode of the PMT. η_{PMT} quantifies the probability of converting incoming photons into detected photoelectrons for the individual PMT. η_{PMT} is given by the product of the QE (section 3.3) and the photoelectron collection efficiency from the photocathode to the first dynode, which is about 70% for each PMT. The mean QE of the PMTs in the bottom array is 32%, while the mean QE of the PMTs in the top array is 24%, with a variation of 3% maximum for the single PMT from the respective mean. The combined

---

[1]The TPC is at very good approximation axially symmetric. Therefore, we use an r-z coordinate system for simplicity.

function γ_{PMT}(r,z) is introduced as γ_{PMT}(r,z) $= \Gamma_{\text{PMT}}$(r,z)η_{PMT}, and it is the quantity that is measured experimentally .

Since in XENON100 we have 178 PMTs, the detected S1 signal is given by the following sum:

$$\text{S1} = \sum_{\text{PMT}=1}^{178} \text{S1}_{\text{PMT}} = n_\gamma(E_R, \mathcal{E})\, \gamma(\text{r,z})\,. \tag{3.10}$$

Where γ(r,z) $= \sum\limits_{\text{PMT}=1}^{178} \gamma_{\text{PMT}}$(r,z).

The S2 signal is generated by the proportional scintillation of the extracted electrons into the xenon gas phase. Before of the extraction in the xenon gas phase, electrons drift through liquid xenon where losses may occur due to attachment to electronegative impurities with characteristic decay time τ, as will be further described in subsection 3.5.2. Therefore, the expectation value for the S2 signal on an individual PMT in units of PE is expressed as [99]:

$$\text{S2}_{\text{PMT}} = n_e(E_R, \mathcal{E})\, e^{-\frac{\Delta t}{\tau}} K G_{\text{S2}} \beta_{\text{PMT}}(\text{x,y})\, \eta_{\text{PMT}} \equiv n_e\, e^{-\frac{\Delta t}{\tau}} \delta_{\text{PMT}}(\text{x,y})\,. \tag{3.11}$$

Here, S2$_{\text{PMT}}$ is the S2 signal detected by an individual PMT. $n_e(E_R, \mathcal{E})$ is the number of produced electrons. K is the extraction efficiency of electrons from the liquid to the gas xenon which is nearly 100% for XENON100 [90]. G_{S2} describes the amplification through photons in the gas phase, and depends primarily on the size of the xenon gas gap and on the extraction field. β_{PMT}(x,y) is the probability that a photon produced in the gas gap at a position (x,y) reaches the photocathode of the PMT. η_{PMT} was introduced above in equation 3.9 and $e^{-\frac{\Delta t}{\tau}}$ is the electron drift loss, further described in subsection 3.5.2. The combined function $\delta_{\text{PMT}}(x, y)$ is introduced as $\delta_{\text{PMT}}(x, y) = K G_{\text{S2}} \beta_{\text{PMT}}(x, y)\eta_{\text{PMT}}$, and it is the quantity that is measured experimentally.

Similarly to the S1 signal, the detected S2 signal is then given by [99]:

$$\text{S2} = \sum_{\text{PMT}=1}^{178} \text{S2}_{\text{PMT}} = n_e\, e^{-\frac{\Delta t}{\tau}} \delta(\text{x,y})\,. \tag{3.12}$$

Where δ(x,y) $= \sum\limits_{\text{PMT}=1}^{178} \delta_{\text{PMT}}$(x,y)[1].

For the S2 signal, it is a common practice to measure the secondary scintillation gain factor, Y, defined as the total number of photoelectrons observed by the PMTs per electron extracted in the gas phase [102]:

$$Y = G_{\text{S2}} <\eta><\beta>\,. \tag{3.13}$$

---

[1]The S2 signal is generated in the gas gap, so the z position of the interaction does not play a role.

Where $<\beta>$ is the mean probability that a photon emitted from the gas gap reaches a PMT photocathode, and $<\eta>$ is the averaged product of the quantum and photocathode collection efficiencies for the PMTs [102]. Y is measured in-situ using S2 signals produced by a single electron, as described in [102]. In XENON100, Y is approximately described by a gaussian distribution with a mean of $(19.7 \pm 0.3)\,\mathrm{PE/e^-}$ and a standard deviation of $(6.9 \pm 0.3)\,\mathrm{PE/e^-}$ [102].

3.5.2 Position dependence of the S1 and the S2 signals

As shown in the previous subsection, the S1 and the S2 signals are position dependent. Therefore, the first step to calculate the recoil energy of an event is to correct the S1 and the S2 signals for space dependent light detection inhomogeneities and attenuation effects. The position corrected S1 and S2 signals, cS1 and cS2, correct for detector geometry effects and are defined by:

$$\mathrm{cS1} = \frac{\mathrm{S1} <\gamma>}{\gamma(r,z)} \equiv \frac{\mathrm{S1}}{\mathrm{LCE_{S1}(r,z)}} . \tag{3.14a}$$

$$\mathrm{cS2} = \frac{\mathrm{S2} <\delta>}{e^{-\frac{\Delta t}{\tau}} \delta(x,y)} \equiv \frac{\mathrm{S2}}{e^{-\frac{\Delta t}{\tau}} \mathrm{LCE_{S2}(x,y)}} . \tag{3.14b}$$

Here, we introduce the Light Collection Efficiencies ($\mathrm{LCE_{S1}}$ and $\mathrm{LCE_{S2}}$). $\mathrm{LCE_{S1}}$ parameterizes the position correction for the S1 signal, while $e^{-\frac{\Delta t}{\tau}}\,\mathrm{LCE_{S2}(x,y)}$ parameterizes the position correction for the S2 signal.

For the S1 signal, the main geometric effect is due to the different paths that the photons travel until they reach a PMT. Solid angle effects, reflectivity of the materials and light absorption by impurities can influence the amount of light which is collected by the PMT arrays. We construct a $\mathrm{LCE_{S1}}$ correction map using mono energetic γ-rays, which are obtained from neutron inelastic scattering or neutron activation. To produce neutrons, an ^{241}AmBe source is deployed. The ^{241}AmBe source is additionally shielded by 10 cm of lead to suppress its high energy (4.4 MeV) γ-ray. The alpha particles emitted by the Americium (Am) source may cause an (α,n) reaction on the Beryllium (Be), emitting neutrons with a broadband energy spectrum extending up to 10 MeV. The inelastic scattering of the neutrons with ^{129}Xe and ^{131}Xe can cause a spin transition of ^{129}Xe and ^{131}Xe to an higher energy level. These excited states of ^{129}Xe and ^{131}Xe have an half-life of 1 ns and 0.5 ns, and they decay to the ground level emitting 40 keV or 80 keV mono energetic γ-rays, respectively. Another possibility is that the neutron activation of ^{128}Xe and ^{130}Xe leads to the creation of the metastable states ^{129m}Xe and ^{131m}Xe, which have a much longer half-lifes of 8.9 and 11.8 days,

respectively. They then decay to the ground state emitting 236 keV or 164 keV mono energetic γ-rays, respectively. Additionally, XENON100 uses a ^{137}Cs and a ^{60}Co source to cross-check the LCE$_{S1}$ obtained from ^{241}AmBe. The decay of ^{137}Cs produces 662 keV mono energetic γ-rays, while the decay of ^{60}Co produces 1170 keV or 1332 keV mono energetic γ-rays. The LCE$_{S1}$ maps from γ-rays induced by neutrons and from γ-rays produced by the decays of ^{60}Co and ^{137}Cs agree within 3% [99].

Fig. 3.14 shows the LCE$_{S1}$ correction map, the amount of the correction for an S1 signal at a given (r,z) position. Across the TPC, the LCE$_{S1}$ is 2 times larger for events produced in the center (r=0) and bottom (z=−300 mm) of the detector, while it is about a 0.6 times lower for events produced at large radii and at the top of the detector.
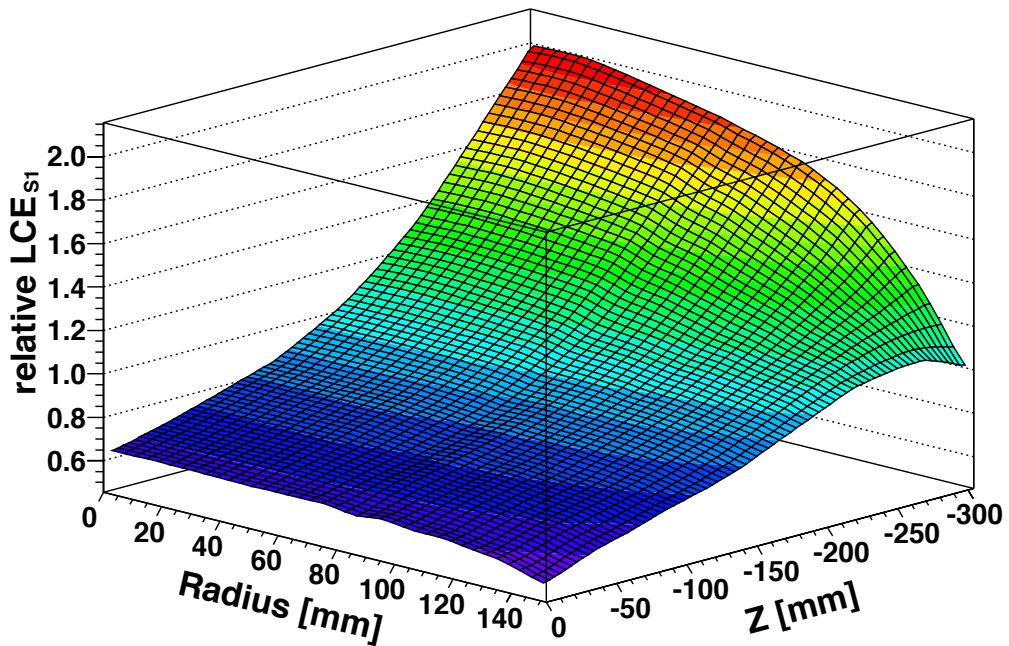
Figure 3.14: *Light Collection Efficiency correction map for the* S1 *signal,* LCE$_{S1}$. *The vertical axis shows the relative* LCE$_{S1}$ *for a given radius and z position. Figure from [90].*

For the S2 signals, a significant attenuation is caused by the loss of electrons. This is due to the attachment of electrons to electronegative impurities during the drift towards the liquid-gas interface. This attenuation can be described by an exponential $e^{-\frac{\Delta t}{\tau}}$, since the probability of an electron absorption is constant during the drift[1].

---

[1] Using the drift time or the z coordinate is equivalent due to fact that the drift velocity is constant.

Here, τ is the characteristic decay time known as the electron lifetime, while Δt is the total drift time. Fig. 3.15 shows the S2 signal size as a function of the drift time for the 662 keV γ-rays emitted by ^{137}Cs. Weekly ^{137}Cs calibrations are used to calculate the electron lifetime by measuring the S2 signal size as a function of the depth of the interaction in the detector.

The electron lifetime measured during the XENON100 Dark Matter Runs increases from around 230 μs during Run-I to around 870 μs during Run-III, due to the continuous purification of liquid xenon from electronegative impurities. In the worst case scenario, considering interactions at the bottom of the TPC (Δt=176 μs) and the minimum measured electron lifetime of 230 μs, the maximum S2 signal reduction is about 47%.
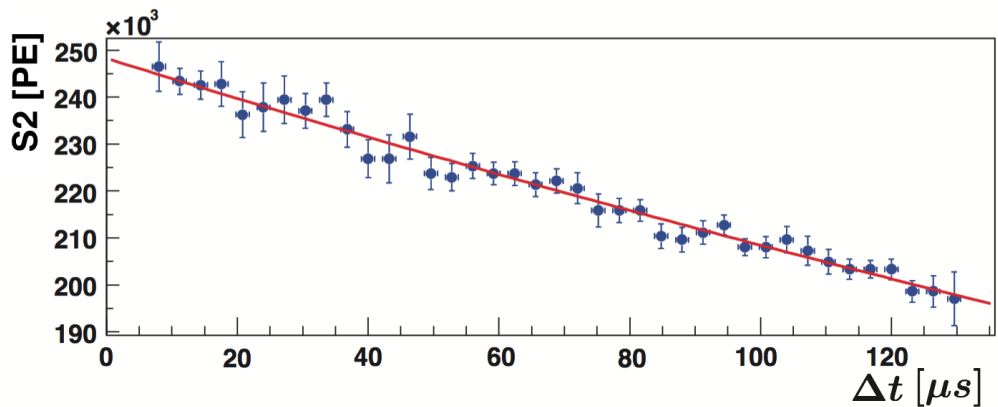
Figure 3.15: S2 *size versus the drift time for a* ^{137}*Cs calibration. An exponential fit is performed to calculate the electron lifetime, which is 556 μs in this example. Figure from [90].*

Additionally, there are second order deviations in the S2 response at large radial positions. An S2 Light Collection Efficiency (LCE$_{S2}$(x,y) correction map can be created using the same mono energetic γ-rays as used for the S1 signal. The maximum LCE$_{S2}$(x,y) correction for the S2 signal is about 10% at large radii [99]. Therefore, equation 3.12 can be very well approximated by:

$$\text{S2} \approx n_e \, e^{-\frac{\Delta t}{\tau}} \, Y \, . \tag{3.15}$$

Where Y was introduced in equation 3.13. This equation will be used in section 3.5.5 and chapter 5 to calculate an S2 energy scale.

3.5.3 Electronic recoils S1 energy calibration

The first step to estimate the S1 energy scale in XENON100 is to measure the response of the detector to mono energetic γ-ray lines which deposit completely their energy in liquid xenon in a single interaction site. In this way, the in-situ measured S1 light for a mono energetic γ-ray line can be used as a fixed point to establish the recoil energy for electronic recoils (E_{ee}) and nuclear recoils (E_{nr}, subsection 3.5.4). We define the S1 light yield ($L_y^{ee}(E_{ee}, \mathcal{E} = 0.53\,\text{kV/cm})$) as the detector-averaged number of detected photoelectrons for a given energy for electronic recoils at the XENON100 electric field of $\mathcal{E} = 0.53\,\text{kV/cm}$:

$$L_y^{ee}(E_{ee}, \mathcal{E} = 0.53\,\text{kV/cm}) = \frac{\text{cS1}}{E_{ee}}. \tag{3.16}$$

Here cS1 was introduced in equation 3.14a.

Fig. 3.16 shows the S1 light yield measured for different mono energetic γ-rays.
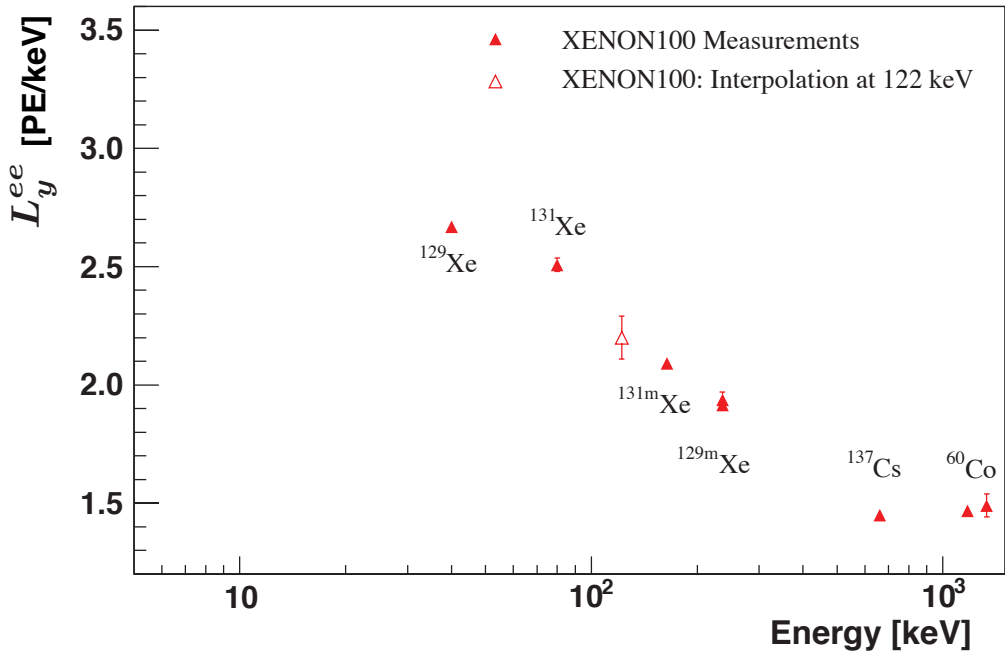
Figure 3.16: S1 *Light yield (L_y^{ee}) for different mono energetic γ-rays. The light yield interpolation at 122 keV is 2.2 PE/keV. Figure from [90].*

Using these mono energetic γ-rays, the L_y^{ee} can be measured as a function of the energy for electronic recoils. Historically, the interpolation of the S1 light yield at 122 keV is taken as the reference energy to construct the nuclear recoil energy scale, as

will be explained in the next subsection. At an electronic recoil energy of $122\,\mathrm{keV}$, the S1 light yield $L_y^{ee}(E_{ee} = 122\,\mathrm{keV}, \mathcal{E} = 0.53\,\mathrm{kV/cm})$ is inferred to be about $2.2\,\mathrm{PE/keV}$ for the different Dark Matter Runs of XENON100 (see Table 4.1).

3.5.4 Nuclear recoils S1 energy calibration

The knowledge of the response to mono energetic γ-rays is not sufficient to calculate the recoil energy for WIMP interactions, since WIMPs induce nuclear recoils. An absolute energy calibration of the detector response to neutrons is challenging because mono energetic neutrons will produce a range of recoil energies due to the variable energy transferred to the xenon nucleus depending on the elastic scattering angle [103]. For this reason, we first estimated the recoil energy for electronic recoils using in-situ measurements in section 3.5.3, and here we explain how we can translate the nuclear recoil energy scale from the electronic recoil energy scale using ex-situ measurements (section 3.5.4). In nuclear recoils, more energy is dissipated into heat compared to an electronic recoil, and the so-called Lindhard factor is introduced to parameterize the larger heat loss in nuclear recoils. The different processes lead to a reduced number of produced photons and an even further reduced number of produced electrons compared to an electronic recoil of the same energy.

The S1 light yield for nuclear recoils is expressed in terms of the S1 light yield for electronic recoils through:

$$
\begin{aligned}
L_y^{nr}(E_{nr}, \mathcal{E} = 0.53\,\mathrm{kV/cm}) &= L_y^{ee}(E_{ee} = 122\,\mathrm{keV}, \mathcal{E} = 0.53\,\mathrm{kV/cm}) \times \\
\mathcal{L}_{eff}(E_{nr}) &\frac{S_{nr}(\mathcal{E} = 0.53\,\mathrm{kV/cm})}{S_{ee}(\mathcal{E} = 0.53\,\mathrm{kV/cm})} \, .
\end{aligned} \tag{3.17}
$$

Where:

- $\mathcal{L}_{eff}(E_{nr})$ is the Lindhard factor which parameterizes the relative scintillation yield of nuclear recoils with energy E_{nr} compared to the reference energy of $122\,\mathrm{keV}$ for electronic recoils at zero electric field. $\mathcal{L}_{eff}(E_{nr})$ is measured ex-situ: small xenon TPCs are used to detect neutrons that scatter in liquid xenon at a known angle in order to deduce the energy of the nuclear recoil and measure $\mathcal{L}_{eff}(E_{nr})$. Alternatively, the neutron scattering from ^{241}AmBe is used in XENON100 to measure $\mathcal{L}_{eff}(E_{nr})$ from Monte Carlo to data spectrum matching. This is an excellent cross-check for the accurate ex-situ scattering measurements of $\mathcal{L}_{eff}(E_{nr})$ as in [104]. Fig. 3.17 shows both the XENON100 and ex-situ measurements of $\mathcal{L}_{eff}(E_{nr})$. The $\mathcal{L}_{eff}(E_{nr})$ measured by XENON100 is about 0.07 at $3\,\mathrm{keV}$ and then increases with the increase of the energy. As shown in Fig.

3.17, a residual systematic uncertainty in the determination of $\mathcal{L}_{eff}(E_{nr})$ remains because the measurements differ of about 30%;

- The electric field dependent light quenching factors for nuclear and electronic recoils, $S_{nr}(\mathcal{E} = 0.53\,\text{kV/cm})$ and $S_{ee}(\mathcal{E} = 0.53\,\text{kV/cm})$, parameterize the reduction in the number of produced photons, due to the fact that electrons are extracted from the interaction site, and some of the electrons do not recombine with ions. The electric field dependent light quenching factors are different for nuclear and electronic recoils: in nuclear recoils, the electrons and ions - produced by the recoil - are distributed in a very dense concentration enhancing the recombination probability compared to electronic recoils, where electrons and ions produced by the recoil are distributed more sparsely over longer tracks (see also section 3.6). Measurements show that at the XENON100 electric field the light quenching factor for nuclear recoils is 0.95, while the light quenching factor for electronic recoils is 0.58 [105].

Figure 3.17: $\mathcal{L}_{eff}(E_{nr})$ as measured by XENON100 (solid blue line) and by ex-situ experiments (points with error bars) as a function of the energy. The dashed green line area is the in-situ measurement from the ZEPLIN TPC [106]. Figure from [104].

Using the S1 light yield for nuclear recoils, the nuclear recoil energy scale is expressed

as[1]:

$$
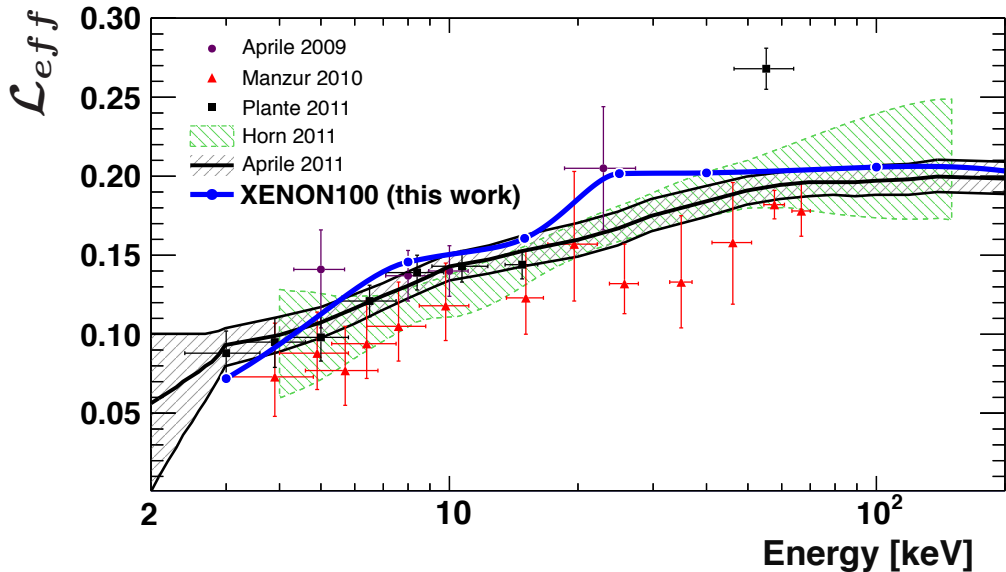\begin{aligned}
E_{nr} &= \frac{cS1}{L_y^{nr}(E_{nr}, \mathcal{E} = 0.53\,\text{kV/cm})} \\
&= \frac{cS1}{L_y^{ee}(E_{ee} = 122\,\text{keV}, \mathcal{E} = 0.53\,\text{kV/cm})\mathcal{L}_{eff}(E_{nr})\frac{S_{nr}(\mathcal{E}=0.53\,\text{kV/cm})}{S_{ee}(\mathcal{E}=0.53\,\text{kV/cm})}}\, .
\end{aligned}
\tag{3.18}
$$

This equation is non-linear in E_{nr} and solving this equation we can relate the energy threshold of XENON100 to the cS1 signal threshold.

Plugging in the previously reported values for L_y^{ee}, S_{ee}, S_{nr} and using $\mathcal{L}_{eff}$ from [107] and the cS1 signal threshold of 3 PE used in [3], we obtain that a cS1 signal threshold of 3 PE corresponds to an energy threshold of 7 keV. However, there is a residual systematic uncertainty in $\mathcal{L}_{eff}$ as aforementioned. For example, using the ex-situ measurement of $\mathcal{L}_{eff}(E_{nr})$ from [108] we calculate an energy threshold of 9 keV. As a consequence, the XENON100 energy threshold could slightly increase depending on the assumed model for $\mathcal{L}_{eff}(E_{nr})$, potentially causing a reduced sensitivity towards low-mass WIMPs.

3.5.5   Nuclear recoil S2 energy scale

In this section we briefly present the nuclear recoil S2 energy scale which will be used in chapter 5 to increase the sensitivity of the XENON100 experiment to low-mass WIMPs.

Modelling the nuclear recoil S2 energy scale is simpler than for the S1 energy scale. Here, we only need the secondary scintillation gain factor, Y, and the electron lifetime, τ, along with ex-situ measurements of the number of electrons produced at a given nuclear recoil energy, Q_y[2]. We do not need to translate the measured energy through an S2 electronic recoil energy E_{ee} due to the presence of single electron signals allowing for the measurement of Y [102]: this standard candle has no analogue in the S1 energy scale.

We can rewrite equation 3.15 as:

$$
S2 \approx Q_y\, E_{nr}\, e^{-\frac{\Delta t}{\tau}}\, Y\, .
\tag{3.19}
$$

---

[1]In 2016, the LUX experiment has measured for the first time the S1 energy scale using a deuterium-deuterium neutron generator. In this way, the factor $L_y^{nr}(E_{nr}, \mathcal{E} = 0.53\,\text{kV/cm})$ is measured in-situ, and the nuclear recoil energy can be calculated using equation 3.18 avoiding any possible systematic uncertainty in the translation of ex-situ measurement. The nuclear recoil energy scales measured by LUX and by XENON100 are in agreement, even though one should note the analytical simplicity and clarity of the LUX calibration method.

[2]Experimental data collected at electric fields between 0.1 kV/cm and 4 kV/cm shows that the electric field dependence of Q_y is weak or negligible [109].

Where we used $n_e = Q_y E_{nr}$. Therefore, the nuclear recoil S2 energy scale is expressed as:

$$E_{nr} \approx \frac{\text{S2}}{Q_y \, E_{nr} \, e^{-\frac{\Delta t}{\tau}} \, Y} \, . \tag{3.20}$$

The equation above will be used in chapter 5 to calculate an S2 energy scale for low-mass WIMP searches.

3.6 Particle identification

In xenon-based detectors it is possible to discriminate between electronic and nuclear recoils, due to the different ratio between the size of the S1 and the S2 signals. For nuclear recoils the amount of scintillation light is relatively large for two reasons:

1. **Different recombination probabilities.** Nuclear recoils and electronic recoils have a different recoil track structure due to different ionization densities [98]. In a nuclear recoil, the energy is lost in almost a point-like interaction leaving the produced electrons in a dense concentration. The ions and the electrons are located in a small volume, increasing the recombination probability. The higher recombination probability implies an enhanced production of scintillation light via recombination. On the other hand, electronic recoils exhibit longer tracks of about $10\,\mu$m [110], leading to a lower recombination probability and thereby less production of scintillation light via recombination.

2. **Enhanced number of immediately produced excitons.** The number of immediately produced excitons, N_{ex}, and electron-ion pairs, N_i, depends on the interaction type [100]. For electronic recoils, the number of ions exceeds the number of immediately produced excitons: $\dfrac{N_{ex}}{N_i} \simeq 0.06$ is calculated in [111], while reference [112] extrapolates from experimental data $\dfrac{N_{ex}}{N_i} < 0.2$. Instead, for nuclear recoils $\dfrac{N_{ex}}{N_i}$ is of O(1) as extrapolated from experimental data [112]. As a consequence, more scintillation light or less ionization is initially created in a nuclear recoil compared to an electronic recoil.

As mentioned in section 3.5.2, we use external sources to measure the LCE. External sources are also used to calibrate the detector response to electronic and nuclear recoils. A $1\,$kBq ^{60}Co and $1.53\,$kBq ^{232}Th sources are used to calibrate the electronic recoil distribution. These sources produce high energies ($>1\,$MeV) γ-rays, which are used to calibrate the response of the detector to electronic recoils using low-energy Compton

scatters with deposited energies of few keV [99]. On the other hand, the response to nuclear recoils is measured using the ^{241}AmBe source, which emits neutrons with a broadband energy spectrum extending up to 10 MeV. The subsequent neutron-induced nuclear recoils have similar low energies as the expected nuclear recoil spectrum caused by a non-relativistic WIMP. In this way, the response to WIMP-induced nuclear recoils can be modelled using ^{241}AmBe.

Fig. 3.18 shows the S2 collected by the bottom array, $cS2_b$, versus the cS1 signal for the electronic and nuclear recoil calibration during Run-II. The $cS2_b$ is used to avoid saturation effects in the PMTs of the top PMT array, even though saturation effects start to play a role only for events with a large cS1 signal. We can see that, for a given cS1 signal, the $cS2_b$ signal for an electronic recoil is larger compared to the $cS2_b$ signal for a nuclear recoil. The discrimination parameter between electronic and nuclear recoils is historically defined as $^{10}\log(cS2_b/cS1)$ [113] and it is used in XENON100 [114]. Fig. 3.19 shows the discrimination parameter versus the cS1 signal for nuclear recoils and electronic recoils and their respective means. For a given cS1 signal, we can clearly see that nuclear recoils have lower values of the discrimination parameter compared to electronic recoils. The discrimination parameter selection is defined to reject 99.75% of electronic recoils. The acceptance to nuclear recoils ranges from about 20% to 60% for cS1 signals in the relevant energy range for WIMP searches [114].
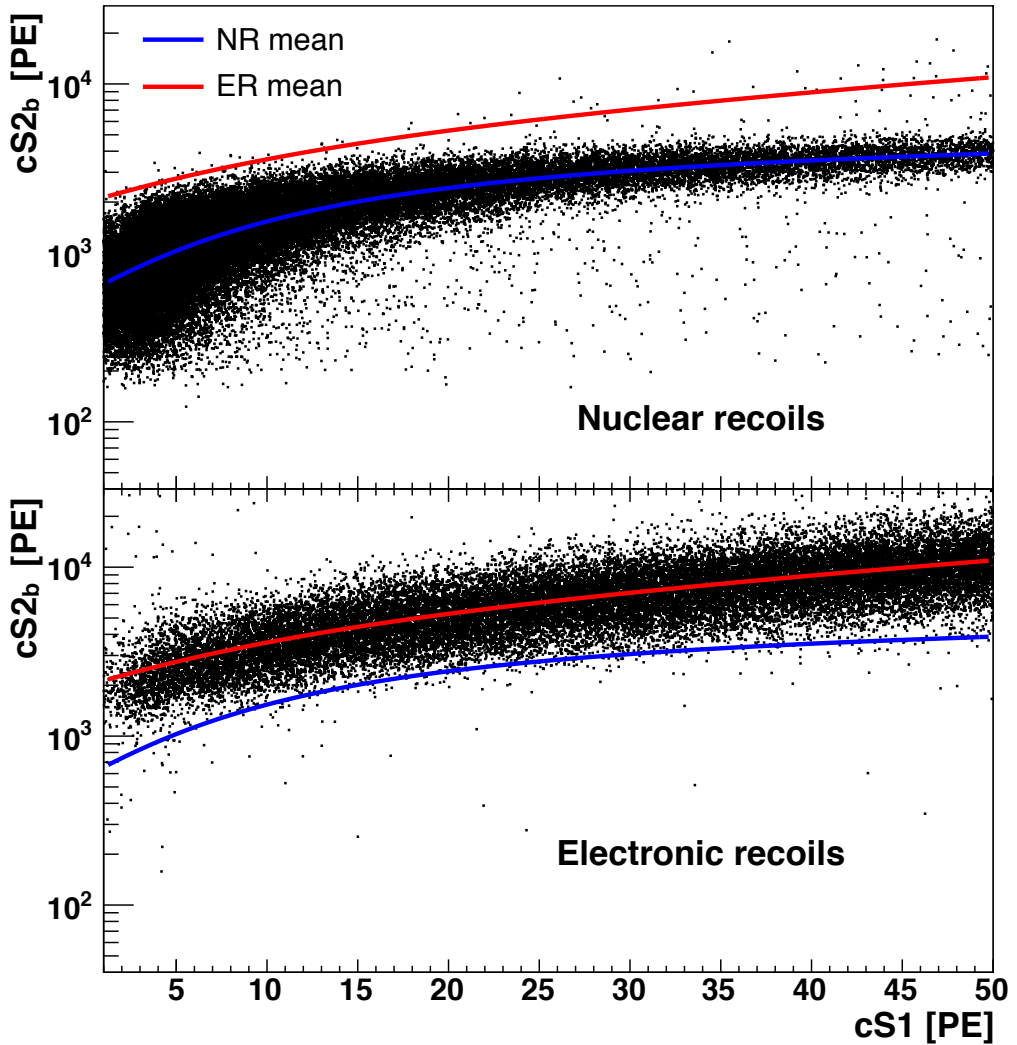
Figure 3.18: *Position corrected S2 collected by the bottom PMT array,* $cS2_b$*, versus the position corrected S1 signal,* cS1*. The black dots are nuclear (top plot) and electronic (bottom plot) recoils. The mean* $cS2_b$ *signal value for a given* cS1 *signal is indicated with the red and blue line for electronic and nuclear recoils, respectively. For a given* cS1 *signal the* $cS2_b$ *is larger in an electronic recoil compared to a nuclear recoil. Neutron and electronic recoil calibration acquired during Run-II are used for the figure.*
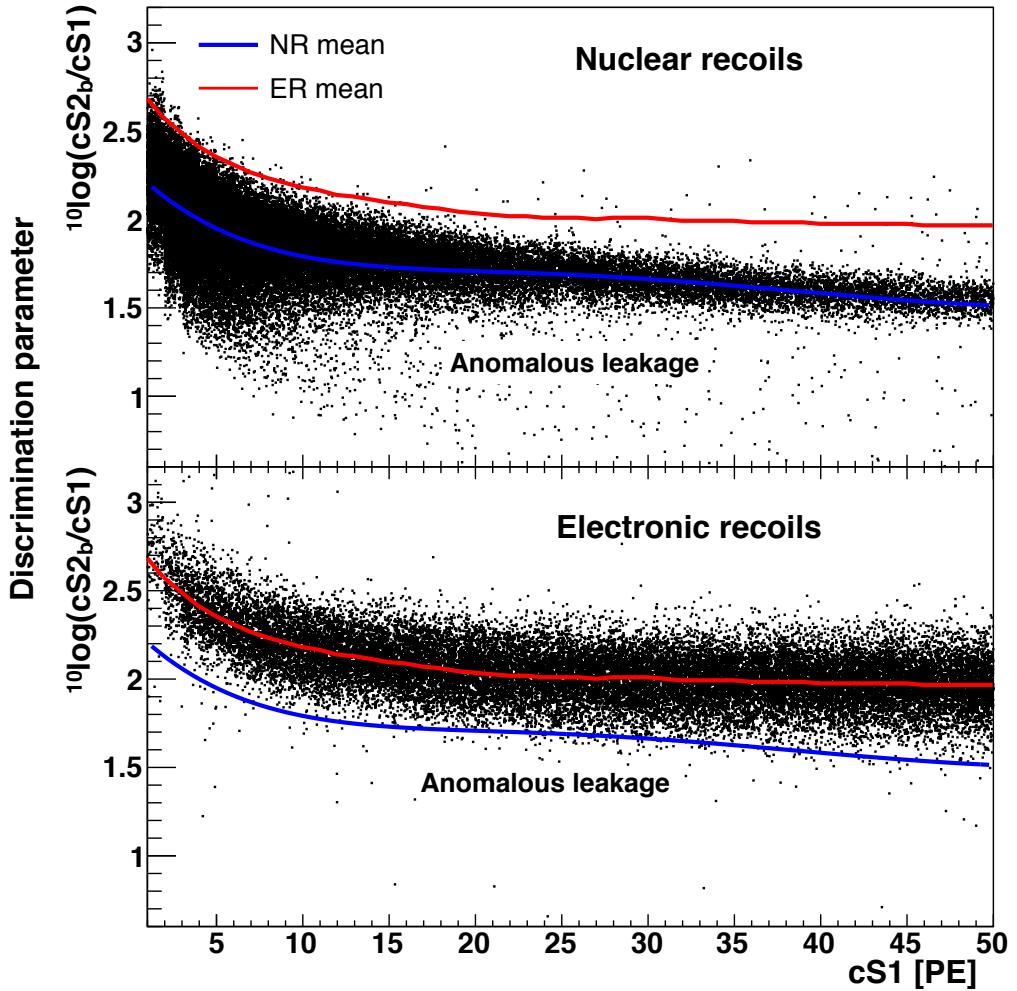
Figure 3.19: *Discrimination parameter, $^{10}\log(cS2_b/cS1)$, versus the position corrected S1 signal, cS1. The black dots are nuclear and electronic recoils. Nuclear recoils (top plot) show a lower value of the discrimination parameter compared to electronic recoils (bottom plot). The discrimination parameter mean for the electronic and nuclear recoils distribution is shown in both canvas with the red and blue line, respectively. Nuclear and electronic recoil calibration data acquired during Run-II are used for the figure.*

Finally, it should be noted that a small fraction of both nuclear and electronic recoils show an anomalous low $^{10}\log(cS2_b/cS1)$ value compared to their respective means. These anomalous low values are caused by accidental coincidences of uncorrelated S1 and S2 signals or double scatters which are erroneously classified as single scatters because one interaction happens in a charge insensitive region of the TPC, e.g. the liquid xenon volume below the cathode as shown in Fig. 3.20.
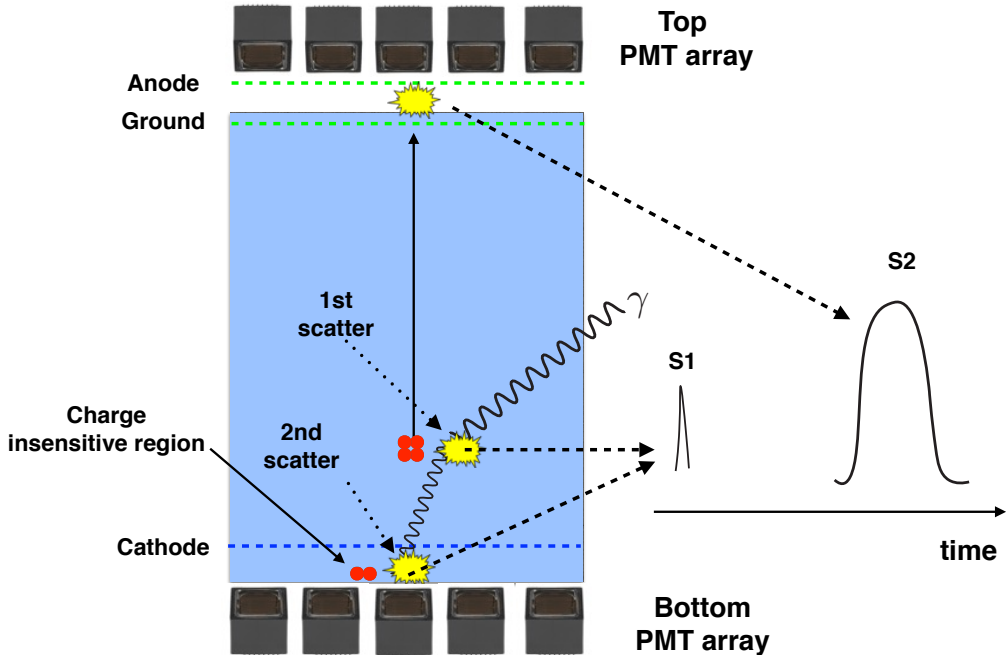
Figure 3.20: *A sketch of an anomalous leakage event. A γ-ray scatters once in the liquid xenon volume between the ground grid and the cathode (1st scatter), and once in the liquid xenon volume below the cathode (2nd scatter). The electrons produced by the 2nd scatter can not be collected, while both scatters generate light which contributes to the S1 signal. This event will show a reduced $^{10}\log(cS2_b/cS1)$ value compared to a single scatter which has the same S1 signal of the anomalous leakage event.*

The two S1 signals can not be separated because the time difference between the two interactions is even within the 10 ns sampling of the PMT waveforms, and the electrons produced in the charge insensitive region can not be collected. Therefore, the observed S1 signal is the sum of the two S1 signals, while only one S2 signal is observed. For electronic recoils, these events can show similar $^{10}\log(cS2_b/cS1)$ values as expected for nuclear recoils. For this reason, they are called anomalous leakage events, and they

constitute a background for WIMP searches. For nuclear recoils, the anomalous leakage events can be partially rejected because they show a lower value of the discrimination parameter compared to the mean for nuclear recoils.

3.7 Backgrounds sources

Ultra low background conditions are required for WIMP detectors in order to potentially identify the very rare WIMP interactions. In this section we summarise the various background sources for XENON100, describing separately sources of electronic and nuclear recoil backgrounds.
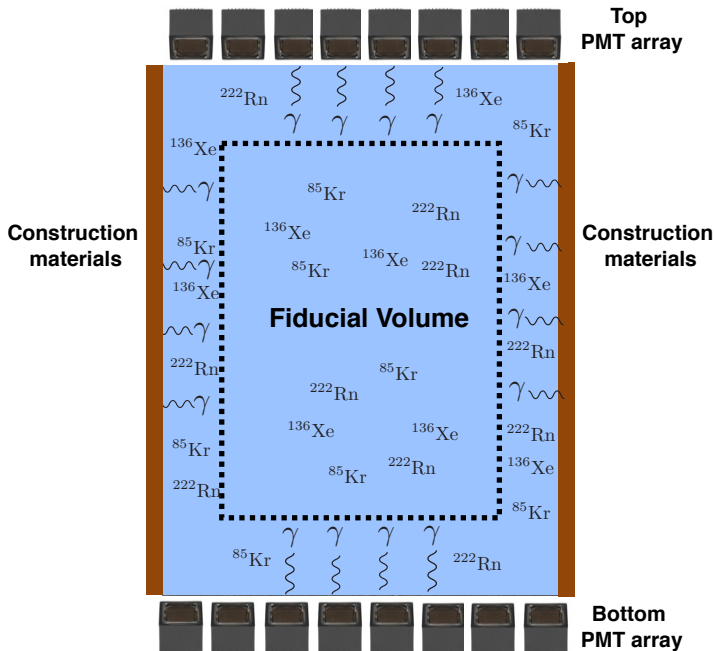
Figure 3.21: *A sketch of the XENON100 TPC and of the location of background-induced electronic recoils inside the TPC. Electronic recoils induced by the radioactivity in the construction materials mostly happen at the edge of the TPC, and they can be rejected using a fiducial volume (black dashed) selection. Instead, the radioactive decays of ^{222}Rn, ^{85}Kr and ^{136}Xe induce electronic recoils which are distributed uniformly in the TPC. A fiducial volume selection is ineffective to reject the electronic recoils caused by these internal background sources.*

3.7.1 Electronic recoils

Electronic recoils are mainly caused by electrons or γ-rays. If electron recoils are not rejected by the S2/S1 discrimination and the induced recoil energy is of the order of keVs, electronic recoils may constitute a background for WIMP searches. Fig. 3.21 shows a sketch of the different electronic recoil background sources. The first contribution comes from the residual radioactivity in the construction materials of the detector. Most of these interactions will occur close to the edge of the detector, due to the short attenuation length of xenon for γ-rays and electrons. These background events are simply removed from the potential WIMP candidate events by defining the fiducial volume. In this way, the background from the construction materials can be reduced thanks to the self shielding properties of xenon.

In addition to the external sources of electronic recoils, internal sources of backgrounds induced by the radioactive decays of ^{222}Rn, ^{85}Kr and ^{136}Xe can also mimic WIMP interactions. These isotopes are soluble into xenon (or part of xenon in the case of ^{136}Xe), being uniformly dispersed inside the target, and they can not be reduced by the fiducialization of xenon, as schematically shown in Fig. 3.21.

Fig. 3.22 shows the energy spectrum of electronic recoils during Run-II and the Monte Carlo simulation of the different contributions to the electronic recoil background. For WIMP searches, we are usually interested in the electronic recoil rate in the energy region between about 1 and 15 keV, which corresponds to WIMP-induced nuclear recoils in the energy region between about 5 and 50 keV. These energy regions are considered for the background estimation. In the following we describe each electronic recoil background contributions from:

- **Materials**: All the construction materials are usually contaminated with small traces of radioactive elements like ^{238}U or ^{232}Th. In addition, stainless steel is known to contain small amounts of ^{60}Co. The decays of these elements produces γ-rays with energies extending to few MeVs. For example, ^{60}Co decays through a β-decay into an excited state of ^{60}Ni, which subsequently decays to the ground state emitting two γ-rays with an energy of 1.17 MeV and 1.33 MeV. The γ-rays with these energies may undergo a Compton scatter with an electron, depositing an energy of few keV in the detector. Subsequently, if they leave the detector without interacting a second time, they can be potentially misidintified as a nuclear recoil. The event rate induced by γ-rays from the construction materials is about 3.0×10^{-3} events/kg/day/keV below 200 keV, as shown in Fig. 3.22.

- ^{222}**Rn**. ^{222}Rn is a heavy noble gas produced in the ^{238}U decay chain, and it

can emanate from the construction materials. ^{222}Rn decays through an α-decay with an energy of 6.5 MeV and an half-life of 3.8 days. The half-life of 3.8 days provides enough time for ^{222}Rn to homogeneously distribute in the liquid xenon volume. Further down the decay chain of radon, the β-decay of ^{214}Pb to ^{214}Bi and the β-decay of ^{210}Pb to ^{210}Bi are potential backgrounds. These β-decays can be directly to the ground state of Bi. Without additional emitted gamma rays, the electron created in the β-decay can induce similar S1 and S2 signals as the ones expected for nuclear or electronic recoils which deposit an energy of few keV. The estimated radon activity is 65 μBq/kg [97] and radon-induced events are the second relevant background. They cause about 2.0×10^{-3} events/kg/day/keV below 200 keV, as shown in Fig. 3.22.

- ^{85}**Kr.** Commercially available xenon contains small traces of krypton. ^{85}Kr is radioactive and it has an isotopic abundance of ^{85}Kr/^{nat}Kr $\sim 10^{-11}$. ^{85}Kr mainly decays through a β-decay with an endpoint energy of 687 keV and an half-life of 10.76 years [99]. Given the half-life, a ^{nat}Kr/Xe concentration of 100 parts per trillion (ppt) corresponds to an activity of about 10 μBq/kg of ^{85}Kr, which induces an event rate of 2×10^{-3} events/kg/day/keV. [90]. Since xenon contains krypton at the ppb (part per billion) level, a cryogenic distillation system is employed to reduce the krypton concentration further. In this way, the ^{nat}Kr contamination of the xenon is reduced to the ppt (part per trillion) level. The xenon gas is first liquefied, and then the different boiling points of krypton and xenon are exploited for separation [90]. During Run-I a small cryogenic distillation system was employed, and the natural krypton concentration was 294 ± 66 ppt. The natural krypton concentration was reduced to 19 ± 4 ppt in Run-II and Run-III using an improved cryogenic distillation system. The electronic recoil background induced by a 19 ± 4 ppt natural krypton concentration is small compared to other backgrounds, as shown in Fig. 3.22.

- ^{136}**Xe.** Natural xenon contains one radioactive isotope, ^{136}Xe, that decays to ^{136}Ba through a double beta decay with an endpoint of 2.45 MeV. The half-life was measured to be $2.21 \pm 0.02(\text{stat}) \pm 0.07(\text{sys}) \times 10^{21}$ years by the KamLAND-Zen collaboration [115] in good agreement with the previous result from the EXO collaboration [94]. Given the half-life and the isotope concentration in natural xenon (Table 3.1) the corresponding activity is about 4 μBq/kg. The contribution of ^{136}Xe to the electronic recoil rate is negligible for XENON100, as shown in Fig. 3.22.
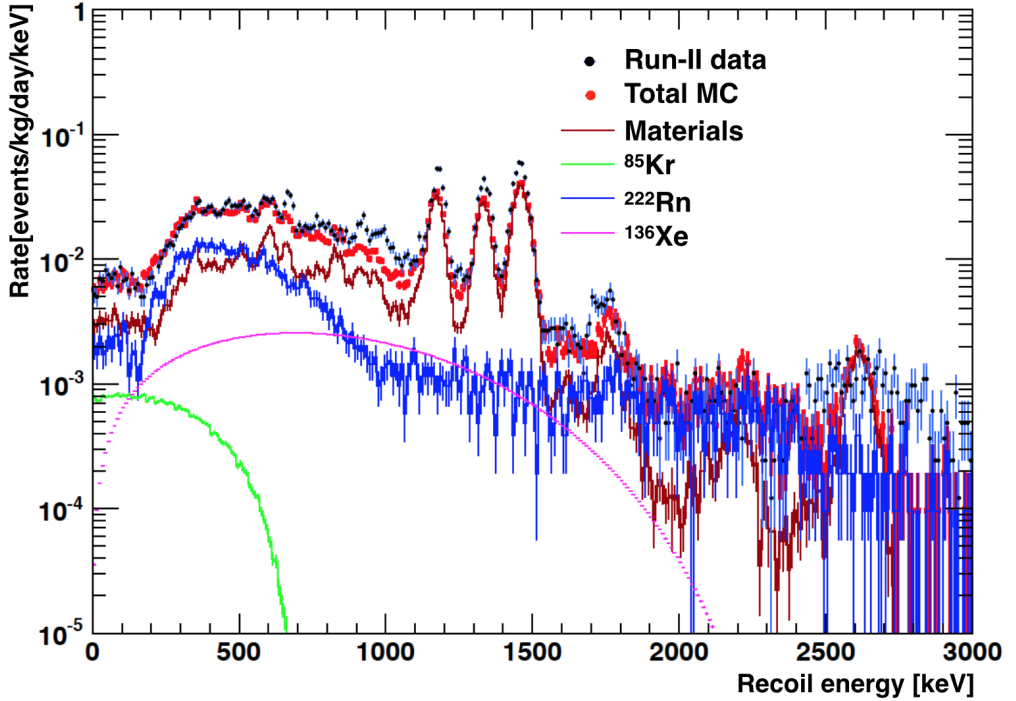
Figure 3.22: *Electronic recoil energy spectrum for Run-II versus the recoil energy. The measured electronic recoil background is given by the black points. The red points are the Monte Carlo simulation of the sum of the different contributions. The residual radioactivity in the construction material is indicated with the brown line. Internal backgrounds from ^{85}Kr, ^{222}Rn and ^{136}Xe are indicated with the green, blue and purple line, respectively. Figure from [97].*

After the S2/S1 discrimination of electronic recoils, the electronic recoil background is 1.5 ± 0.2 events in the fiducial volume for the Run-II exposure [3], while for Run-III is 0.9 ± 0.2 events in the fiducial volume. The different value is due to the different number of live days in Run-II and Run-III, 223 and 153 days respectively. For Run-I, despite the lower number of live days (100 days), the electronic recoil background is 3.7 ± 0.5 events in the fiducial volume, due to the higher krypton concentration [3].

3.7.2 Nuclear recoils

Neutrons, which undergo a single elastic scatter with a xenon nucleus, can become an irreducible background for WIMP searches because they cannot be distinguished from a WIMP-induced nuclear recoil.
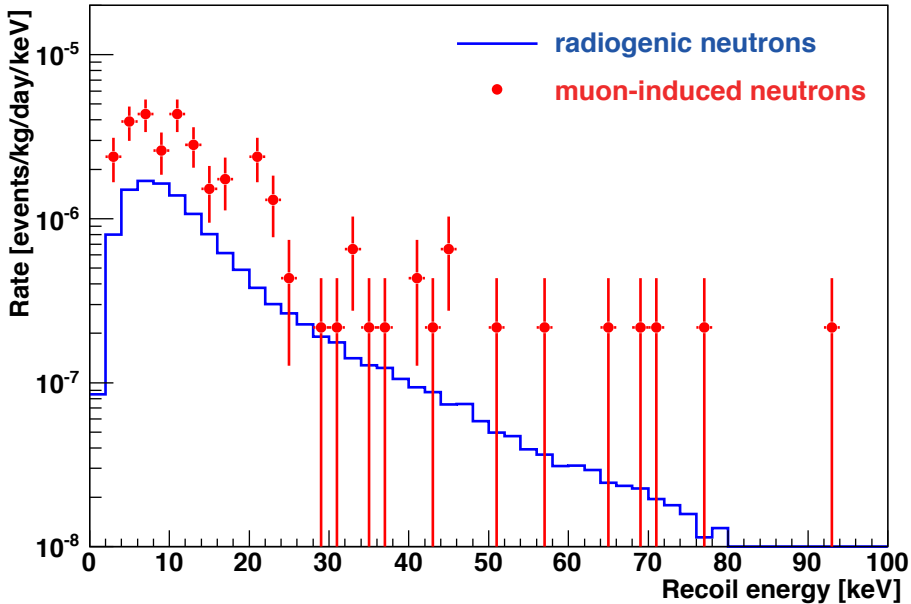
Figure 3.23: *Event rate as a function of the recoil energy for Run-II. The muon-induced (red points) and the radiogenic neutron background (blue line) are indicated. Figure from [116].*

Fig. 3.23 shows the neutron background event rate for Run-II, with two main sources of neutron-induced background as predicted in [116] using Monte Carlo simulations:

- **Muon-induced neutrons.** Muon-induced neutrons are produced by high-energy cosmic-ray muons through e.g. photo-nuclear reactions in electromagnetic showers or interactions between the muon and the nucleus. Cosmogenic neutrons can have energies extending to a few GeV, and may cause a nuclear recoil with a few keV energy when they elastically scatter with a xenon nucleus. To reduce this background, XENON100 is located at the underground laboratory of Gran Sasso where the cosmic-ray muon flux is reduced by six orders of magnitudes compared

to the surface. The event rate peak caused by muon-induced neutrons is 5×10^{-6} events/kg/day/keV at $5\,\mathrm{keV}$, and it decreases with the recoil energy as shown in Fig. 3.23.

- **Radiogenic neutrons.** As for γ-rays, neutrons can also be produced by the residual radioactivity of the construction materials through spontaneous fission or (α,n) reactions. These neutrons have energies extending to about $10\,\mathrm{MeV}$ [116], and they can cause a recoil with a few keV energy. The event rate peak caused by radiogenic neutrons is about 2×10^{-6} events/kg/day/keV at $5\,\mathrm{keV}$, and it decreases with the recoil energy as shown in Fig. 3.23.

In the fiducial volume, the neutron-induced nuclear recoil background is 0.17 ± 0.10 events for the Run-II exposure [99]. Similar values are calculated for the other runs [3].

3.8 Conclusions

In this chapter we described the XENON100 experiment. After reviewing the general property of xenon, we focused on the XENON100 dual phase Time Projection Chamber, describing the detector and the data acquisition system. Then, we described how the scintillation and ionization created by an incoming particle are detected as an S1 and an S2 signal in XENON100. The S1 and S2 signal are used to reconstruct the position of the interaction and to perform particle identification, while the recoil energy is reconstructed from the S1 signal or the S2 signal. The main backgrounds in the XENON100 TPC are finally described: the background levels of the XENON100 TPC were crucial to reach the XENON100 science goals.

4

XENON100 results assuming the presence of an unknown background

The XENON100 collaboration performed three Dark Matter searches (Run-I, Run-II and Run-III) between January 2010 and January 2014. The results were published in [3], and the minimum excluded WIMP-nucleon cross section was $1.1 \times 10^{-45}\,\mathrm{cm^2}$ at a WIMP mass of $50\,\mathrm{GeV}$, as previously shown in Fig. 2.4. The limits were calculated using a profile likelihood approach which assumes that the detector can be completely modelled with the backgrounds known, understood and subtracted.

But, what happens if there is an unknown background? What if the assumption of the modelling breaks down? Then, the limit can exclude WIMP-nucleon cross sections that would be instead allowed or, even worse, a false discovery can be claimed, due to the underestimation of the backgrounds.

Indeed, it is clear that some backgrounds, e.g. anomalous leakage events, are hard to model [117]. Here we ask the question: **if** we do not trust the background modelling, what kind of exclusion limit can we set anyway? To compare the results with [3], we use the same event selection, yet we use a different statistical method resilient to contamination from such an unknown background. We will calculate the excluded WIMP-nucleon cross section using the maximum gap method [118], which will be explained in this chapter. In this way, we will verify that even without background modelling the XENON100 data is still able to exclude the WIMP interpretation of the observed annual modulation by DAMA/LIBRA [67] and a large fraction of the WIMP interpretation of CDMS-II [77].

4.1 Datasets

XENON100 performed Dark Matter Runs in 2010 (Run-I), in 2011-2012 (Run-II) and
in 2013-2014 (Run-III) of 100.9, 223.1 and 153.0 live days each, respectively. Run-I was
a particularly important milestone in the Dark Matter field as it was the first time a
TPC containing more than 100 kg of xenon was operated for several months. Table 4.1
shows the values of the main parameters for the three Dark Matter Runs operated by
XENON100, which we will explain here.

The S1 light yield is similar for the three Runs, and the cS1[1] signal threshold is
the same for the three Runs. Accounting for the cS1 threshold determines an effective
energy threshold of about 7 keV for each Run (see equation 3.18). The ^{85}Kr concentra-
tion was a factor 15 larger in Run-I compared to Run-II and Run-III (section 3.7.1).
Since krypton is homogeneously distributed inside the liquid xenon volume, a fiducial
volume selection is not effective against it. However, at the edges of the detector the
background from the construction materials is still dominant compared to the back-
ground from krypton, and, therefore, a relatively loose fiducial volume selection remains
effective to increase the sensitivity to WIMPs.

In Run-I, the event rate induced by the background from krypton and by the back-
ground from the construction materials were approximately equal to each other when
using a fiducial volume of 48 kg. In Run-II and Run-III, the krypton contamination was
reduced by a factor of 100, and the krypton background became irrelevant compared
to the background induced by the construction materials. Therefore, a reduction in
the fiducial volume both minimised the background from the construction materials
and maximised the sensitivity to WIMPs: a fiducial volume of 34 kg (55% of the liquid
xenon target) was chosen for Run-II and Run-III.

Finally, the WIMP-like observed events (WIMP candidates) were three for Run-
I, and one for Run-II and Run-III [3]. In Run-I we observed three WIMP candidates
because the electronic recoil background is larger in Run-I compared to Run-II and Run-
III. Ultimately in this work, the inclusion of Run-I leads to overly conservative results
without background subtraction. We therefore decide to use only Run-II and Run-III
to calculate the XENON100 results when allowing for the presence of an unknown
background. Given that Run-I constitutes 27% of the total exposure of XENON100,
the exclusion of Run-I can not change significantly the limit.

---

[1]cS1 is the position corrected S1 signal introduced in section 3.5.2.

Table 4.1: *Main parameters of the detector during the first, second and third Dark Matter Run [3].*

Parameter	Run-I	Run-II	Run-III
Period	2010	2011-2012	2013-2014
Live days	100.9	223.1	153.0
S1 Light yield	2.20 PE/keV	2.28 PE/keV	2.25 PE/keV
cS1 signal threshold	3 PE	3 PE	3 PE
Energy threshold	7 keV	7 keV	7 keV
^{85}Kr concentration	300 ppt	20 ppt	20 ppt
Fiducial volume	48 kg	34 kg	34 kg
WIMP candidates	3	1	1

4.2 Event selection

The goal of the event selection criteria is to select WIMP candidate events while removing background events. WIMPs are expected to induce nuclear recoil energies of the order of ten keV, as described in chapter 2. We thus consider only low-energy events with a cS1 signal between 3 and 30 PE, which corresponds to WIMP recoil energies between about 7 keV and 45 keV (see equation 3.18 for details).

The event selection criteria are extensively described in [99], and in this work we use the same selection criteria. For description purposes, we divide the event selection criteria in three categories: selection of interactions in liquid xenon, fiducial volume selection and S2/S1 discrimination selection.

4.2.1 Selection of interactions in liquid xenon

The exhaustive details of the XENON100 WIMP selection can be found in [99]. For this work, we will illustrate two important selections to give the reader a feel for how a liquid xenon Dark Matter analysis is performed.

One of the most important selections is the removal of non-physical interactions using a two-fold PMT coincidence to identify valid S1 signals [99]. A dark current signal in a single PMT can create a S1 signal of a few PE, and it can mimic an interaction of

a low-energy event. Since a dark current signal is unlikely to happen in multiple PMTs at the same time, a two-fold PMT coincidence requirement is used to efficiently reject PMT dark current signals. To illustrate, Fig. 4.1 (top panel) shows a waveform of a low-energy event with an S1 signal of 3.6 PE. In this case, the S1 PMT pattern (Fig. 4.1 (bottom panel)) shows that the S1 signal is observed by three PMTs in total (two PMTs in the top PMT array and one PMT in the bottom PMT array), and therefore is considered a valid candidate.
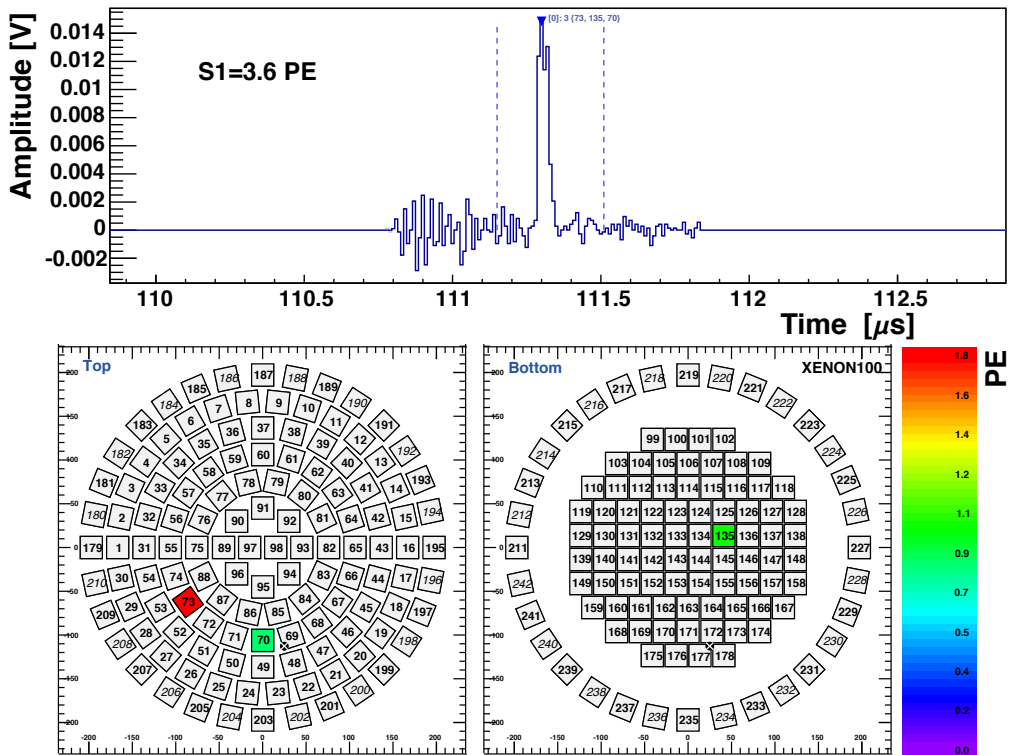
Figure 4.1: *(top)* S1 *Waveform of a low-energy event with an* S1 *signal of 3.6 PE. (bottom)* S1 *PMT pattern in the top and bottom PMT array for the* S1 *signal shown above. The* S1 *signal is produced by a physical interaction because it is observed by three PMTs.*

Looking at another selection: an important cut is used to reject interactions in the xenon gas phase. If a particle interacts between the top PMT array and the upper ground mesh, it will produce electrons that drift downwards towards the anode. When the electrons reach the high field region, proportional scintillation takes place, and an S2 signal is created. The S2 signal can potentially pile up with a lone S1 signal, perhaps from an interaction in the liquid below the cathode. These events are usually called

gas events, and they can be wrongly identified as WIMP events.

Fig. 4.2 shows a sketch of an interaction in the xenon liquid phase and of an interaction in the xenon gas phase. The S2 signal of the gas event is produced closer to the top PMT array compared to the event originating from the interaction in the liquid phase. This results in an asymmetric S2 signal distribution in the top and the bottom PMT array. In gas events a larger fraction (about 65%) of the total S2 is detected by the top PMT array compared to an interaction in the liquid (about 55%). When more than 62% of the S2 light is observed by the top PMT array the event is identified as a gas event, and is therefore rejected [99].
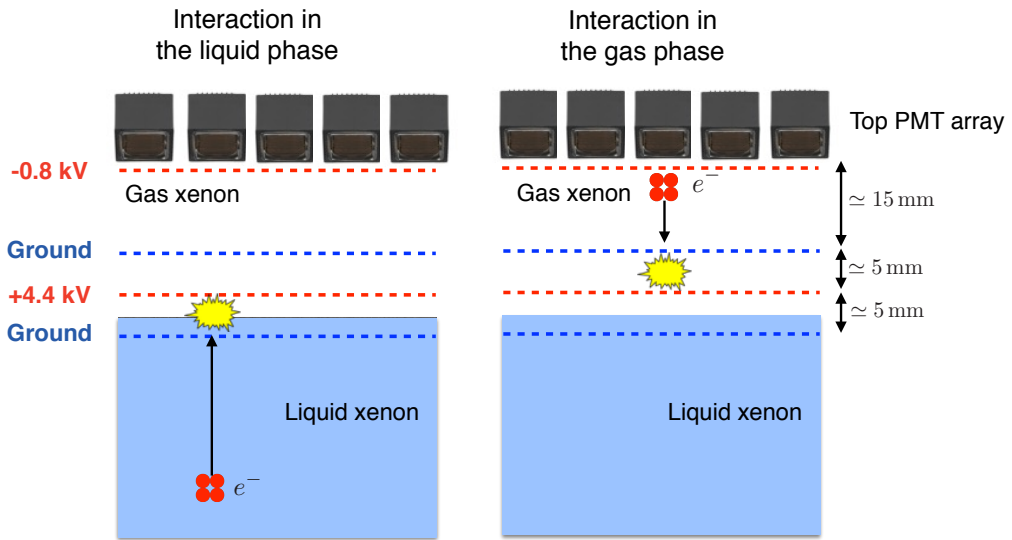
Figure 4.2: *A sketch of an interaction in the liquid xenon phase and of an interaction in the gas xenon phase.*

The acceptance of the selection to reject gas events and the acceptance of the two-fold PMT coincidence requirement are estimated using nuclear recoil calibration data, and they are shown in Fig. 4.3. The acceptance of the two-fold PMT coincidence is 58% for cS1 signals of 3 PE, increasing to above 94% for cS1 signals larger than 8 PE. The two-fold PMT coincidence requirement turns out to be the dominant driver of acceptance loss between all the selection criteria for cS1 signals lower than 8 PE. The acceptance of the selection to reject gas events is 97% for cS1 signals of 3 PE and increases to 100% for cS1 signals above 13 PE. When the two selections explained in this section and all the other selection criteria described in [99] are applied, the acceptance is further reduced by about 20%, as shown in Fig. 4.3. The acceptance of the event

selection criteria is shown as a function of the cS1 signal, which will be later used in the maximum gap method (section 4.3.2).
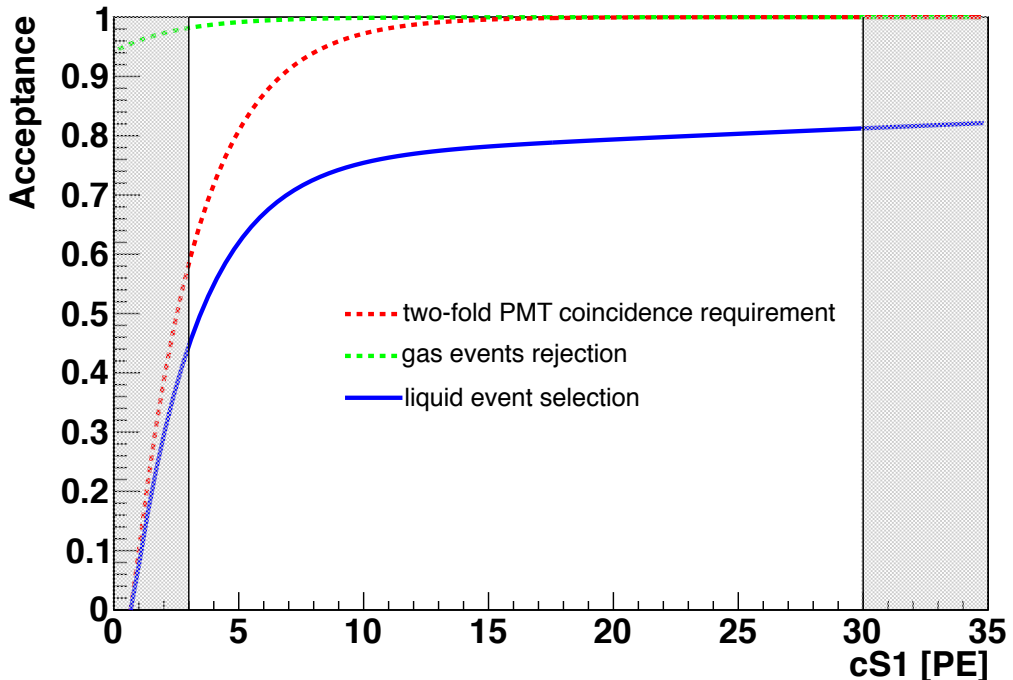
Figure 4.3: *Acceptance of the selection to reject gas events (green dashed line) and of the two-fold PMT coincidence requirement (red dashed line). The acceptance of the selection of interactions in liquid xenon (liquid event selection) is given by the blue line. The* cS1 *range between 3 and 30 PE is used for the analysis.*

4.2.2 Fiducial volume selection

Fig. 4.4 shows the z-r^2 distribution of events in Dark Matter data after selecting events in liquid xenon in Run-II and Run-III. Clearly, most of these events are located close to the edge of the detector, where we expect the residual radioactivity to cause a substantial background. These background events are removed using a fiducial volume selection: events inside the fiducial volume are accepted, while events outside are rejected. Remaining events are frequently caused by internal background sources, e.g. krypton and radon as described in section 3.7.1. As a consequence, these events are uniformly spread across the TPC, and a fiducial volume selection is not effective against them. The fiducial volume is indicated by the super-elliptical region inside the green

dashed line, and it contains 34 kg for Run-II and Run-III. Indicated in red are events remaining after all selection criteria are applied. These events are considered WIMP candidates.
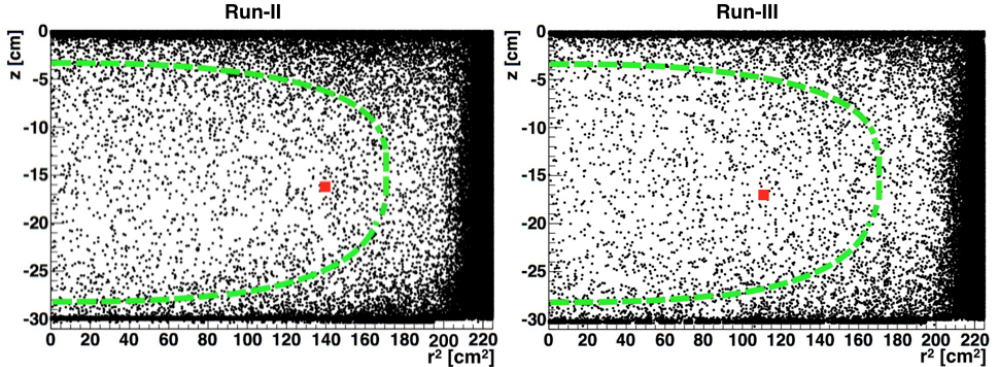
Figure 4.4: *z position versus r^2 for Run-II (left) and Run-III (right). The green dashed line indicates the 34 kg fiducial volume. The black dots are the events observed during the Dark Matter Runs, while the red squares are the WIMP candidates.*

4.2.3 S2/S1 discrimination selection

After selecting liquid events and applying the fiducial volume selection, we make use of the expected properties of a WIMP interaction. WIMPs are expected to cause nuclear recoils, while the majority of the background is expected to be caused by electronic recoils (see section 2.3). As described in section 3.6, electronic and nuclear recoils produce differing amounts of charge/light (S2/S1).

Fig. 4.5 shows the discrimination parameter, $^{10}\log(cS2_b/cS1)$ (section 3.6), as a function of the cS1 signal for Run-II and Run-III. We can clearly see that the majority of the events show values of the discrimination parameter similar to the ones expected for electronic recoils backgrounds. We apply an S2/S1 discrimination parameter which rejects 99.75% of the electronic recoils. After applying the S2/S1 discrimination selection, in Run-II and Run-III one event shows values of the discrimination parameter which can be compatible with the ones expected for nuclear recoils.
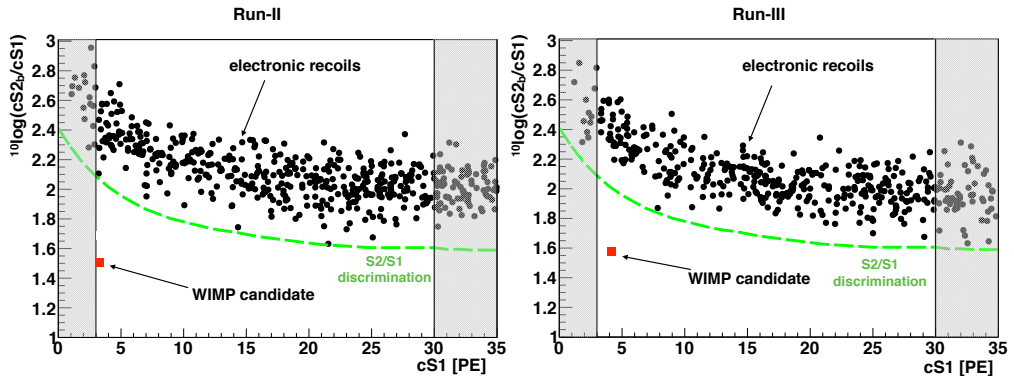
Figure 4.5: *Discrimination parameter, $^{10}log($ $cS2_b/cS1)$, versus the $cS1$ signal for Run-II (left) and Run-III (right). The black dots are electronic recoils, while the red squares are the WIMP candidates for each Run. The green dashed line is the S2/S1 discrimination parameter selection. The $cS1$ range between 3 and 30 PE is used for the analysis.*

4.2.4 Total acceptance

The acceptance of the event selection criteria is shown in Fig. 4.6. Given the similarity of the runs [3], we make the approximation of modelling Run-II and Run-III as each having the same averaged acceptance.

The acceptance of the liquid event selection is 80% for cS1 signals above 20 PE, and rapidly decreases to 45% for cS1 signals of 3 PE. The dominant driver of this loss is given by the two-fold PMT coincidence requirement, as described above. The S2/S1 discrimination selection acceptance is determined using the fraction of events removed in the nuclear recoil calibration data. The acceptance is 60% for cS1 signals of 3 PE, it decreases to 20% for cS1 signals of 25 PE and it increases for cS1 signals above 25 PE. This is because the relative charge to light ratio varies non linearly, and xenon has its best difference at a few keV at the chosen electric drift field. The total acceptance is given by the product of the liquid event selection and the S2/S1 discrimination selection.

The acceptance of the fiducial volume is considered in the exposure (34 kg × 376.1 days) and is therefore not reported in Fig. 4.6. As previously mentioned, the fiducial volume selection reduces by 45% the xenon target mass.

Figure 4.6: *Acceptance of the WIMP event selection criteria. The dashed blue line is the acceptance of the liquid event selection criteria while the dashed green line is the acceptance of the S2/S1 discrimination parameter selection. The total acceptance (black line) is given by the product of the acceptance of the liquid event selection criteria and of the acceptance of the S2/S1 discrimination parameter selection. The cS1 range between 3 and 30 PE is used for the analysis.*

4.3 WIMP Search
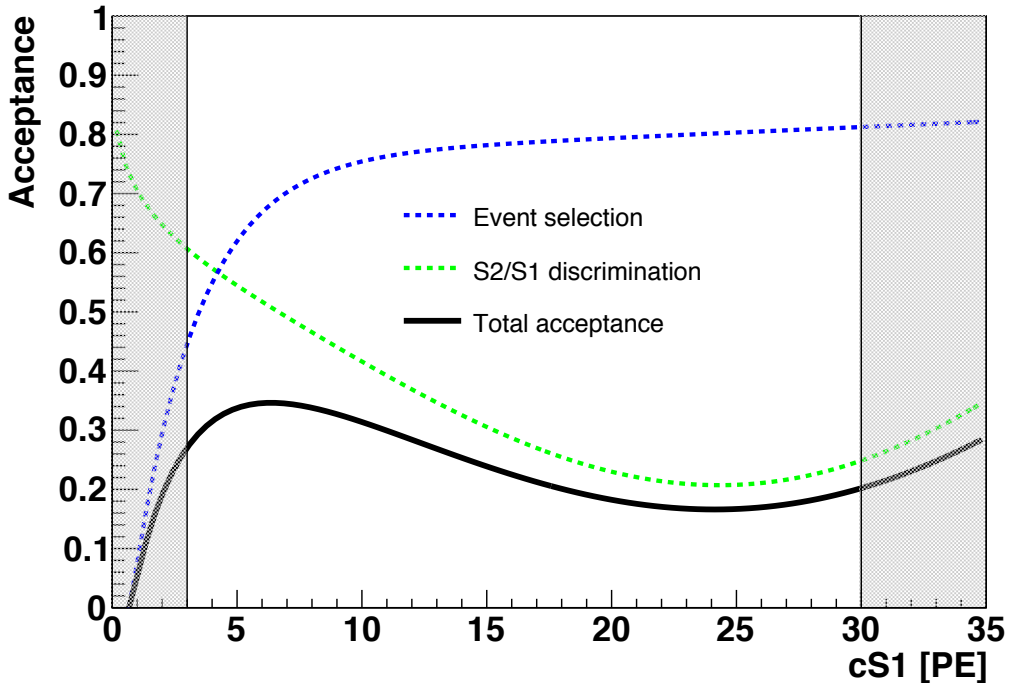
After determining the acceptance, we have all the ingredients to calculate a WIMP exclusion limit at our disposal. In section 2.1 we described the WIMP event rate as a function of the recoil energy. In section 3.5 we showed how the recoil energy is measured as a cS1 signal by the XENON100 detector. In the previous section, we then described the selection of the WIMP candidates and its acceptance. Subsection 4.3.1 shows how we can express the WIMP event rate as a function of the cS1 signal using the aforementioned quantities. We will then apply a statistical method in subsection 4.3.2 to determine a WIMP exclusion limit, showing the results in subsection 4.3.3.

4.3.1 WIMP spectrum

In order to calculate the XENON100 results, we express the WIMP differential rate as a function of the cS1 signal[1] ($\frac{dR}{dcS1}$) [99]:

$$\frac{dR}{dcS1} = \epsilon_{cS1} \int \frac{dR}{dE_{nr}} \epsilon_{S2}(E_{nr}) \, p(cS1|E_{nr}) dE_{nr} \,. \tag{4.1}$$

Where ϵ_{cS1} is the total acceptance. $\frac{dR}{dE_{nr}}$ is the WIMP rate as a function of the nuclear recoil energy. $\epsilon_{S2}(E_{nr})$ is the acceptance of the S2 threshold cut (see section 3.2.1), which is applied before the smearing of the WIMP energy spectrum into the WIMP cS1 spectrum. The S2 threshold cut acceptance is determined separately because it influences the S1 signal detection efficiency via the energy sharing at the level of the produced photons and electrons by the WIMP interaction. The S2 threshold is effectively below the S1 threshold in energy, so the acceptance loss is less than 5% for cS1 signals above $3\,\mathrm{PE}$ [114]. $p(cS1|E_{nr})$ is the probability to produce a cS1 signal given a nuclear recoil energy E_{nr}. To determine $p(cS1|E_{nr})$, we use equation 3.18 which we re-state here for convenience:

$$E_{nr} = \frac{cS1}{L_y^{ee} \mathcal{L}_{eff}(E_{nr}) \frac{S_{nr}}{S_{ee}}} \,. \tag{4.2}$$

We use $L_y^{ee} = 2.265\,\mathrm{PE/keV}$, which is the average of Run-II ($L_y^{ee} = 2.28\ \mathrm{PE/keV}$) and Run-III ($L_y^{ee} = 2.25\,\mathrm{PE/keV}$) (Table 4.1). $\mathcal{L}_{eff}$ is the same used in [119], while S_{nr}=0.95 and S_{ee}=0.58 as described in section 3.5.

We assume Poisson fluctuations in the number of photoelectrons that initiate the secondary emission in the PMT. We approximate the resolution of the PMTs with a gaussian distribution with a mean given by the previous poisson-distributed number of photoelectrons. The width of the gaussian distribution is given by the product of the single photoelectron PMT resolution ($0.5\,\mathrm{PE}$ as measured in [90]) and of the square root of the number of photoelectrons. Fig. 4.7 shows $p(cS1|E_{nr})$ for monoenergetic nuclear recoils with different energies, from $7\,\mathrm{keV}$ to $40\,\mathrm{keV}$.

We can see that the cS1 signal mean increases with the increase of the nuclear recoil energy. The cS1 signal widths are also important: for a nuclear recoil energy of $7\,\mathrm{keV}$, the mean of the cS1 distribution is $3.2\,\mathrm{PE}$, leaving only about 50% of the cS1 signals produced above the cS1 threshold of $3\,\mathrm{PE}$.

---

[1]As discussed in section 3.5, the energy is determined from the S1 signal alone. A more general approach would express the differential event rate as a function of the S1 and the S2 signals.
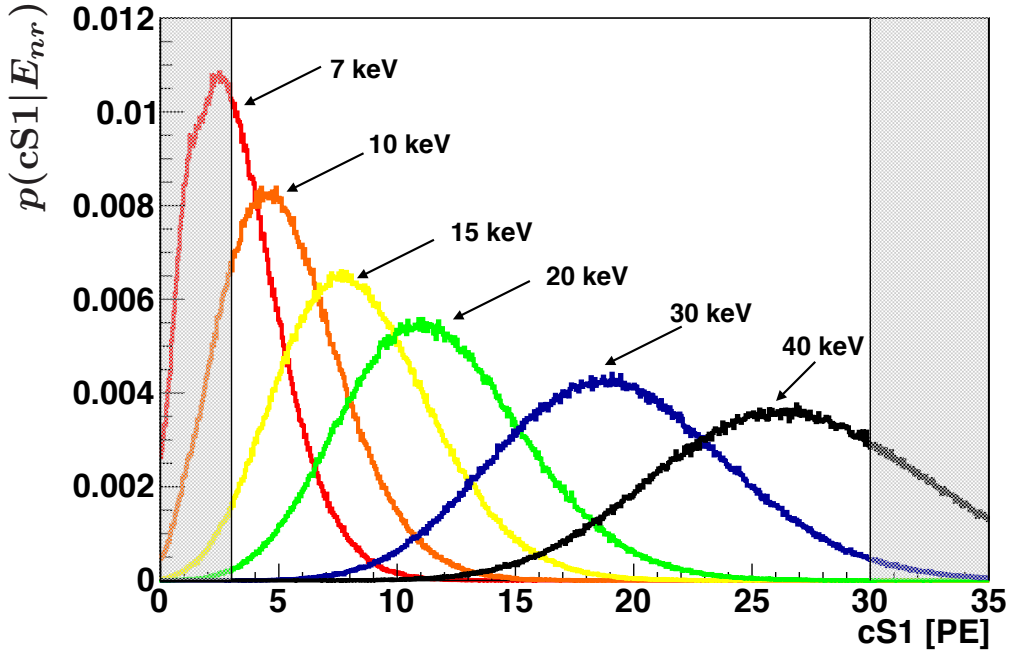
Figure 4.7: *Probability of observing a* cS1 *signal given a nuclear recoil with an energy E_{nr} ($p(cS1|E_{nr})$) from 7 keV (red line) to 40 keV (black line). For 7 keV, the mean* cS1 *signal is 3.2 PE, while for 40 keV the mean* cS1 *signal is 27.2 PE. The* cS1 *range between 3 and 30 PE is used for the analysis.*

Having determined $p(cS1|E_{nr})$, we can calculate the WIMP cS1 spectrum, $\dfrac{dR}{d\text{cS1}}$, using equation 4.1. We also conservatively set $L_{eff}(E_{nr})$ to zero for nuclear recoil energies below 3 keV to account for uncertainties in the $\mathcal{L}_{eff}$ measurement. Fig. 4.8 shows $\dfrac{dR}{d\text{cS1}}$ for a WIMP with a mass of 10, 100 and 1000 GeV using a WIMP-nucleon cross section of $10^{-45}\,\text{cm}^2$.

Low-mass WIMPs produce lower cS1 signals than heavier WIMPs, due to the fact that low-mass WIMPs induce recoils with lower energies compared to heavier WIMPs. As a consequence, the 3 keV $L_{eff}(E_{nr})$ cut-off and the cS1 signal threshold of 3 PE limit the XENON100 sensitivity for low-mass WIMPs. Instead, heavier WIMPs have broader spectra, and both the 3 keV $L_{eff}(E_{nr})$ cut-off and the cS1 signal threshold of 3 PE become less important.
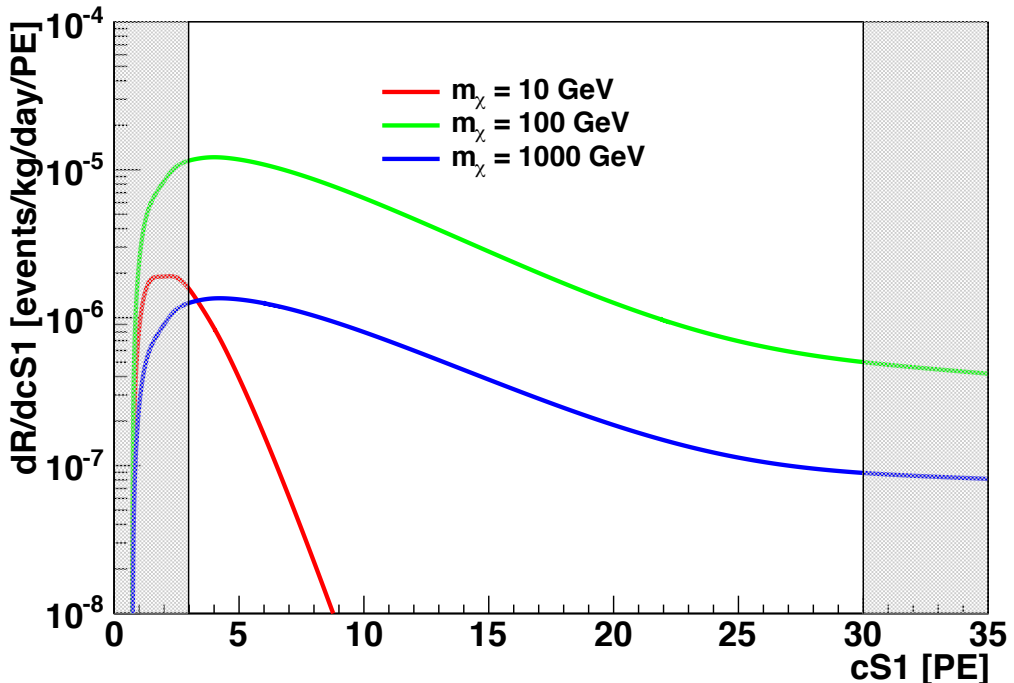
Figure 4.8: *WIMP cS1 spectrum, $\frac{dR}{dcS1}$, for a WIMP with a mass of 10 GeV (red line), 100 GeV (green line line) and 1000 GeV (blue line) for a WIMP-nucleon cross section of $10^{-45}\,cm^2$. The cS1 range between 3 and 30 PE is used for the analysis.*

4.3.2 The maximum gap method

As mentioned, the most recent XENON100 limits use the profile likelihood method, which relies on accurate modelling to account for background. Here, we relax this assumption of accurately modelled background. A method to make good use of data with unknown background, called the maximum gap method, was developed in [118]. In principle, the method exploits the difference between the signal spectra and that of an arbitrary background.

Fig. 4.9 shows an illustration of the maximum gap method. We assume that the signal expectation is given by equation 4.1 for a given WIMP-nucleon cross section. The number of expected observed WIMP-scatter events, μ, can then be calculated as:

$$\mu = \int_{3\,\mathrm{PE}}^{30\,\mathrm{PE}} \frac{dR}{dcS1} dcS1 \,. \tag{4.3}$$

Where the integral is done between the lower and upper threshold of the WIMP search,

cS1=3 PE and cS1= 30 PE. We can see in this particular example that events at cS1 signals larger than 20 PE are most likely coming from background because they do not follow the expected signal distribution[1].
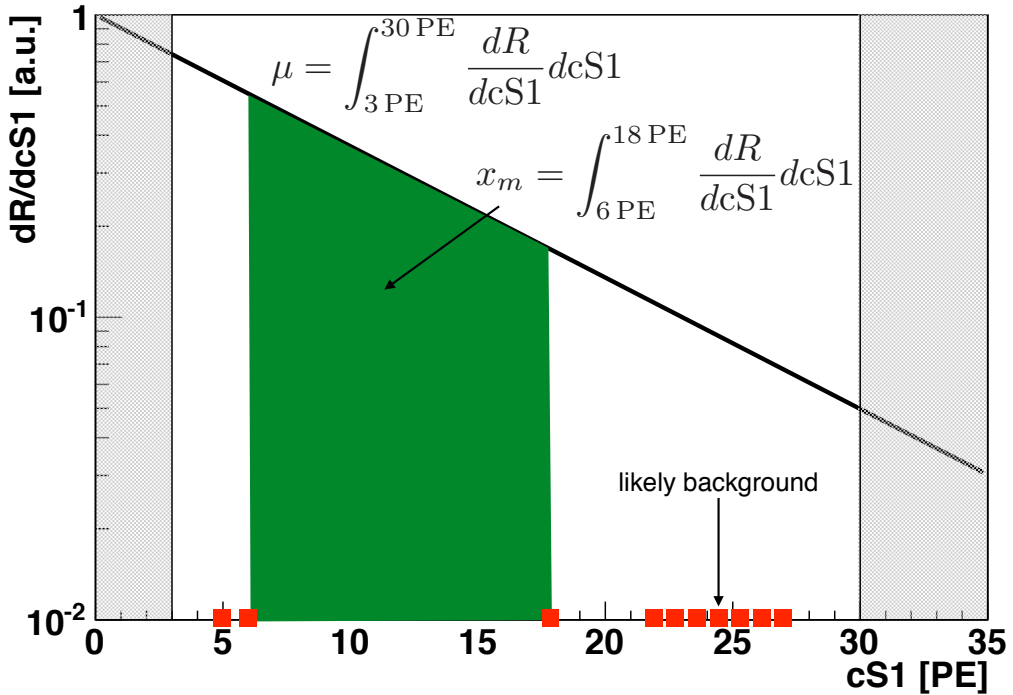
Figure 4.9: *Illustration of the maximum gap method. The WIMP cS1 spectrum, $\frac{dR}{d\text{cS1}}$, is given by the black line, while the observed events are the red squares. Seven events are observed for cS1 signals larger than 20 PE. They are probably induced by backgrounds because they do not follow an exponential distribution. Between 5 PE and 18 PE we observe three events, and the maximum gap is found between the events at cS1=6 PE and cS1=18 PE (green shaded region). The gap between the events at cS1=5 PE and cS1=6 PE has a smaller size. The cS1 range between 3 and 30 PE is used for the analysis.*

We can note that between every two events at cS1 signals cS1_i and cS1_{i+1} there is an integral expected event rate, called a "gap" in [118]. A gap is calculated as:

$$x_i = \int_{\text{cS1}_i}^{\text{cS1}_{i+1}} \frac{dR}{d\text{cS1}} d\text{cS1}, \tag{4.4}$$

with x_i varying depending on the WIMP-nucleon cross section and the interval in

---

[1]If we would use all the events in Fig. 4.9 to set a limit using e.g., Poisson statistics, we would set an overly conservative limit.

question[1]. The maximum gap is defined as the gap with the greatest size, x_m, between all the possible gaps. Qualitatively, a cross section is rejected if the expected number of WIMP events in the maximum gap are too many compared to the non-observation in that gap. Quantitatively, it is shown in [118] that given the maximum gap size, x_m, and the total expected number of events μ, the confidence level, C_0, is given by:

$$C_0 = \sum_{k=0}^{i} \frac{(kx_m - \mu)^k e^{-kx_m}}{k!} \left(1 + \frac{k}{\mu - kx_m}\right). \tag{4.5}$$

Where i is the greatest integer that satisfies $i \leq \mu/x_m$. A confidence level of 90% is typically used. Practically, the exclusion limit is calculated by decreasing the WIMP-nucleon cross section until μ and x_m give C_0=90%.

The lower and upper cS1 thresholds were fixed for the original blind analyses carried out on the individual runs [3]. The sensitivity of the detector to light WIMPs is heavily influenced by the selection of the lower threshold; the 3 PE threshold used corresponds to the lowest point where the acceptance remained well understood. The upper threshold has a relatively minimal impact on the analysis as most WIMP recoils are at low energies. 30 PE was originally chosen to allow accurate background estimations in the profile likelihood analysis. Even so, for this analysis the threshold is still appropriate - for the heaviest WIMPs considered here, about 10% of the WIMP cS1 spectrum is expected to appear at higher cS1 values.

We can now show two concrete examples for the XENON100 data. In Run-II and Run-III we have one WIMP candidate with a cS1 signal of 3.8 PE and 4.7 PE, respectively. Fig. 4.10 (a) shows the WIMP cS1 spectrum for a WIMP with a mass of 100 GeV and a WIMP-nucleon cross section of 2.48×10^{-45} cm^2. The maximum gap is found between 4.7 PE and 30 PE, with $x_m = 2.80$ events, while the total number of expected events between 3 PE and 30 PE is $\mu = 3.45$ events. Therefore, we have $i = 1$, and applying equation 4.5 a WIMP with a WIMP-nucleon cross section of 2.48×10^{-45} cm^2 and a mass of 100 GeV is excluded with 90% confidence level. Fig. 4.10 (b) shows the WIMP cS1 spectrum for a WIMP with a mass of 10 GeV and a cross section of 3.32×10^{-43} cm^2. In this case, the maximum gap is found between 3 PE and 3.8 PE, with $x_m = 4.13$ events, while the total number of expected events between 3 PE and 30 PE is $\mu = 9.36$ events. Therefore, $i = 2$, and we exclude a WIMP with a mass of 10 GeV and a WIMP-nucleon cross section of 3.32×10^{-43} cm^2 with a 90% confidence level using equation 4.5.

---

[1]The upper/lower cS1 thresholds are effectively used as events that start/end the x_i calculation. A gap can also be between an event and an interval boundary.

(a)

(b)
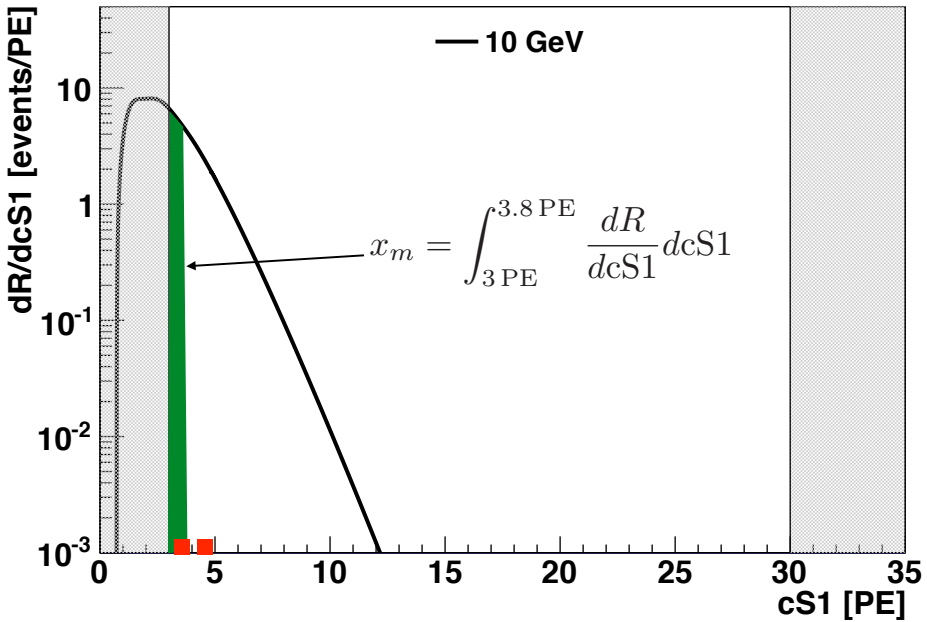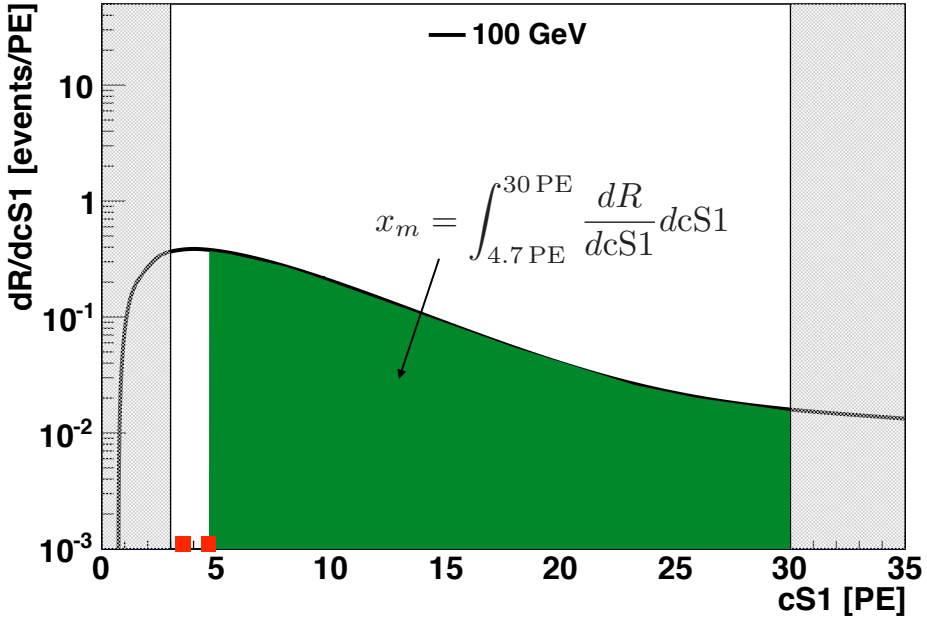
Figure 4.10: *(a) Maximum gap method illustrated for a WIMP with a mass of 100 GeV and a cross section of 2.48× 10⁻⁴⁵ cm². (b) Maximum gap method illustrated for a WIMP with a mass of 10 GeV and a cross section of 3.32× 10⁻⁴³ cm². The* cS1 *range between 3 and 30 PE is used for the analysis.*

4.3.3 Exclusion limit discussion

We use the data from Run-II and Run-III under the assumption of a single run with
an exposure given by the fiducial volume (34 kg) multiplied for the live days of the
two runs (376.1 days). This assumption is a close approximation of the simple-merger
method outlined in [120]. We perform the analysis in the mass range 6-1000 GeV.
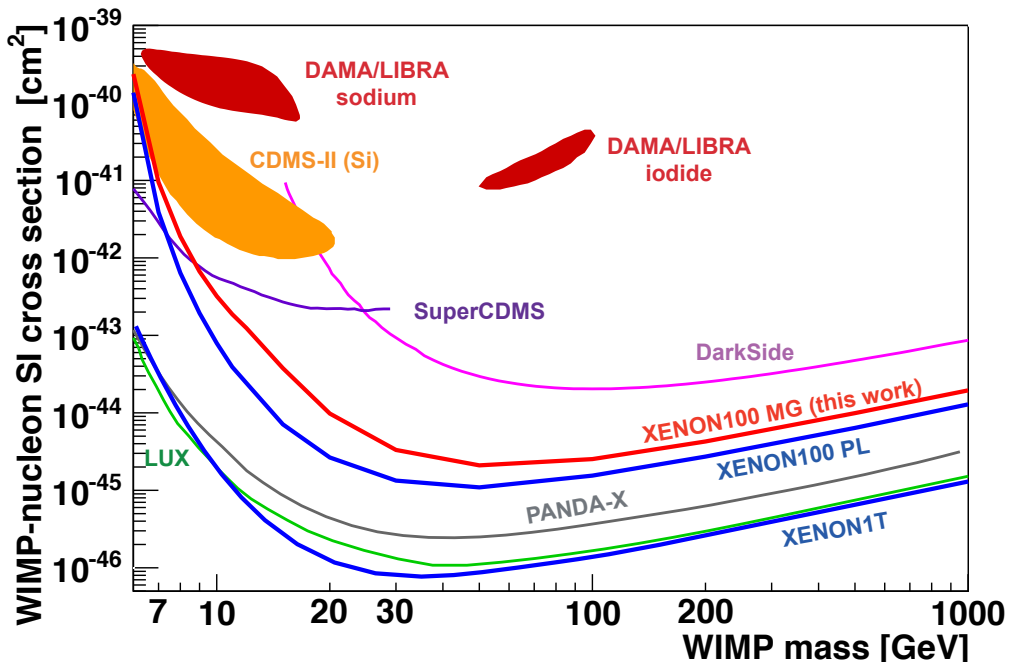
Figure 4.11: *WIMP-nucleon cross section as a function of the WIMP mass. The 90% con-
fidence level XENON100 exclusion limit calculated in this work using the maximum gap (MG)
method is shown with the red line, while the exclusion limit calculated in [3] using the profile
likelihood (PL) method is given by the dashed blue line. The DAMA/LIBRA [67] and CDMS-SI
[77] contour regions and the exclusion limits from SuperCDMS [68], DarkSide [72], LUX [57],
XENON1T [75] and PANDA-X [71] are also reported.*

Fig. 4.11 shows the 90% confidence level exclusion limit obtained in this work.
The best exclusion is found for a WIMP-nucleon cross section of 2.05×10^{-45} cm^2 at
a WIMP mass of 50 GeV. The cross section exclusion rapidly decreases for low-mass
WIMPs due both to the 3 keV $\mathcal{L}_{eff}$ cut-off and the 3 PE cS1 signal threshold, while
it rises smoothly with the WIMP mass above 50 GeV due to the linearly decreasing
WIMP number density with the increasing WIMP mass. Fig. 4.11 also shows the final
results of XENON100 using the profile likelihood method [3]. Compared to the profile

likelihood method, the excluded WIMP-nucleon cross section obtained in this work is about a factor 2 worse for a WIMP with a mass of $50\,\mathrm{GeV}$. The worsening of the results is expected due to the relaxation of the well modelled background assumption in [3]. Results from other experiments are also reported: XENON1T [75], PANDA-X [71] and LUX [57] have more than an order of magnitude better sensitivity compared to XENON100, due mainly to the lower background rate and the larger exposure as explained in section 2.4.

4.4   Conclusions

In this chapter we asked the question: what limits can we set on WIMPs with XENON100 if we drop the assumption of a well modelled background? First, we described how a Dark Matter analysis is done in a xenon TPC. After applying the selection criteria for WIMPs and determining its acceptance, we are able to interpret the results in terms of the excluded WIMP-nucleon cross section at a given WIMP mass. In this thesis, we use the maximum gap method to interpret the results without background modelling and subtraction. Even relaxing the assumption on the background modelling, namely accounting for unknown backgrounds, the XENON100 data still excludes the WIMP interpretation of the observed annual modulation by DAMA/LIBRA [67] and a large fraction of the WIMP interpretation of CDMS-II [77].

5

Low-mass WIMP search with the XENON100 detector

The DAMA/LIBRA and the CDMS-II collaboration have claimed or shown evidence of an observation of a low-mass WIMP. The XENON100 collaboration excludes the claim reported by the DAMA/LIBRA collaboration and a large fraction of the 3σ evidence reported by the CDMS-II collaboration, as shown in Fig. 4.11. However, in the last years there has been a debate in the literature about the calculation of the XENON100 exclusion limit for low-mass WIMPs.

As described in section 3.5, an energy threshold of about $7\,\text{keV}$ is determined from the cS1 signal threshold of $3\,\text{PE}$. However, the value of the energy threshold is influenced by the model chosen for $\mathcal{L}_{eff}$. Several studies, e.g. [121] [122], have shown that different $\mathcal{L}_{eff}$ models can potentially increase the XENON100 energy threshold, decreasing the XENON100 sensitivity especially for low-mass WIMPs.

In an attempt to improve the XENON100 sensitivity towards low-mass WIMPs and to clarify the controversies between experiments, we developed a novel low-mass WIMP search technique based on the experience from the XENON10 experiment [80]. We use the S2 signal to reconstruct the energy, and we do not apply any constraints on the observation of an S1 signal. If the energy is reconstructed from the S2 signal, a substantial reduction of the energy threshold is possible. Indeed, due both to the direct Q_y measurement of LUX down to $0.7\,\text{keV}$ [103] and to the XENON100 secondary scintillation gain factor of $20\,\text{PE/e}^-$, an energy threshold of $0.7\,\text{keV}$ can be achieved in XENON100 using the S2 energy scale. On the other hand, if we do not require an S1 signal we lose three main features of a xenon TPC, namely the particle identification, the z position reconstruction, and the ability to construct a complete background model.

Without a background model, we will assume that every event remaining after the data selection could be a valid WIMP candidate. In this way, we are still able to set an exclusion limit, but we will never be able to make a discovery. Nonetheless, we will show that we improve the XENON100 sensitivity for WIMPs with a mass below 7.4 GeV, due to the reduced energy threshold. For example, the XENON100 sensitivity for WIMPs with a mass below 6 GeV is improved by more than a factor of 10.

The paper was published in Physical Review D94, 092001 (2016) [4] and was based on an analysis I developed and presented to the XENON100 collaboration. I'm one of the corresponding authors. In the following we reprint the publication.

Low-mass dark matter search using ionization signals in XENON100

E. Aprile,[1] J. Aalbers,[2] F. Agostini,[3, 4] M. Alfonsi,[5] F. D. Amaro,[6] M. Anthony,[1] F. Arneodo,[7] P. Barrow,[8]
L. Baudis,[8] B. Bauermeister,[5, 9] M. L. Benabderrahmane,[7] T. Berger,[10] P. A. Breur,[2] A. Brown,[2] E. Brown,[10]
S. Bruenner,[11] G. Bruno,[12, 3] R. Budnik,[13, *] A. Buss,[12] L. Bütikofer,[14] J. M. R. Cardoso,[6] M. Cervantes,[15]
D. Cichon,[11] D. Coderre,[14] A. P. Colijn,[2] J. Conrad,[9, †] J. P. Cussonneau,[16] M. P. Decowski,[2] P. de Perio,[1]
P. Di Gangi,[4] A. Di Giovanni,[7] E. Duchovni,[13] A. D. Ferella,[3, 9] A. Fieguth,[12] D. Franco,[8] W. Fulgione,[3, 17]
M. Galloway,[8] M. Garbini,[4] C. Geis,[5] L. W. Goetzke,[1] Z. Greene,[1] C. Grignon,[5] E. Gross,[13] C. Hasterok,[11]
E. Hogenbirk,[2] R. Itay,[13] B. Kaminsky,[14] G. Kessler,[8] A. Kish,[8] H. Landsman,[13] R. F. Lang,[15] L. Levinson,[13]
M. Le Calloch,[16] C. Levy,[10] F. Linde,[2] S. Lindemann,[11] M. Lindner,[11] J. A. M. Lopes,[6] A. Lyashenko,[18]
A. Manfredini,[13] T. Marrodán Undagoitia,[11] J. Masbou,[16] F. V. Massoli,[4] D. Masson,[15] D. Mayani,[8]
A. J. Melgarejo Fernandez,[1] Y. Meng,[18] M. Messina,[1] K. Micheneau,[16] B. Miguez,[17] A. Molinario,[3] M. Murra,[12]
J. Naganoma,[19] U. Oberlack,[5] S. E. A. Orrigo,[6, ‡] P. Pakarha,[8] B. Pelssers,[9] R. Persiani,[16] F. Piastra,[8] J. Pienaar,[15]
G. Plante,[1] N. Priel,[13] L. Rauch,[11] S. Reichard,[15] C. Reuter,[15] A. Rizzo,[1] S. Rosendahl,[12] N. Rupp,[11] J. M. F. dos
Santos,[6] G. Sartorelli,[4] M. Scheibelhut,[5] S. Schindler,[5] J. Schreiner,[11] M. Schumann,[14] L. Scotto Lavina,[16]
M. Selvi,[4] P. Shagin,[19] H. Simgen,[11] A. Stein,[18] D. Thers,[16] A. Tiseni,[2, §] G. Trinchero,[17] C. D. Tunnell,[2, ¶]
M. von Sivers,[14] R. Wall,[19] H. Wang,[18] M. Weber,[1] Y. Wei,[8] C. Weinheimer,[12] J. Wulf,[8] and Y. Zhang[1]

(XENON Collaboration)

[1]*Physics Department, Columbia University, New York, New York, 10027, USA*
[2]*Nikhef and the University of Amsterdam, Science Park, 1098XG Amsterdam, Netherlands*
[3]*INFN-Laboratori Nazionali del Gran Sasso and Gran Sasso Science Institute, 67100 L'Aquila, Italy*
[4]*Department of Physics and Astrophysics, University of Bologna and INFN-Bologna, 40126 Bologna, Italy*
[5]*Institut für Physik & Exzellenzcluster PRISMA, Johannes Gutenberg-Universität Mainz, 55099 Mainz, Germany*
[6]*Department of Physics, University of Coimbra, 3004-516, Coimbra, Portugal*
[7]*New York University Abu Dhabi, Abu Dhabi, United Arab Emirates*
[8]*Physik-Institut, University of Zurich, 8057 Zurich, Switzerland*
[9]*Department of Physics, Stockholm University, Stockholm, SE-10691 Sweden*
[10]*Department of Physics, Applied Physics and Astronomy, Rensselaer Polytechnic Institute, Troy, New York 12180, USA*
[11]*Max-Planck-Institut für Kernphysik, 69117 Heidelberg, Germany*
[12]*Institut für Kernphysik, Wilhelms-Universität Münster, 48149 Münster, Germany*
[13]*Department of Particle Physics and Astrophysics, Weizmann Institute of Science, Rehovot, 7610001, Israel*
[14]*Albert Einstein Center for Fundamental Physics, University of Bern, 3012 Bern, Switzerland*
[15]*Department of Physics and Astronomy, Purdue University, West Lafayette, Indiana 47907, USA*
[16]*SUBATECH, Ecole des Mines de Nantes, CNRS/In2p3, Université de Nantes, Nantes 44307, France*
[17]*INFN-Torino and Osservatorio Astrofisico di Torino, 10125 Torino, Italy*
[18]*Physics & Astronomy Department, University of California, Los Angeles, California, 90095, USA*
[19]*Department of Physics and Astronomy, Rice University, Houston, Texas 77005, USA*
(Dated: December 20, 2016)

We perform a low-mass dark matter search using an exposure of 30 kg×yr with the XENON100 detector. By dropping the requirement of a scintillation signal and using only the ionization signal to determine the interaction energy, we lowered the energy threshold for detection to 0.7 keV for nuclear recoils. No dark matter detection can be claimed because a complete background model cannot be constructed without a primary scintillation signal. Instead, we compute an upper limit on the WIMP-nucleon scattering cross section under the assumption that every event passing our selection criteria could be a signal event. Using an energy interval from 0.7 keV to 9.1 keV, we derive a limit on the spin-independent WIMP-nucleon cross section that excludes WIMPs with a mass of $6 \text{ GeV}/c^2$ above $1.4 \times 10^{-41} \text{ cm}^2$ at 90% confidence level.

———

* ran.budnik@weizmann.ac.il
† Wallenberg Academy Fellow
‡ Present address: IFIC, CSIC-Universidad de Valencia, Valencia, Spain
§ atiseni@nikhef.nl
¶ ctunnell@nikhef.nl

I. INTRODUCTION

Astrophysical observations indicate that dark matter (DM) is needed to explain structures ranging from the scales of galaxies to the largest observed scales [1]. Nevertheless, little is known about its nature. One theoretically favored candidate is a weakly interacting massive particle (WIMP). These particles may be detectable with experiments sensitive to WIMP-induced nuclear recoils [2].

Most WIMP models predict particles with a mass at the electroweak scale of $\sim 100 \, \text{GeV}/c^2$ [3]. However, there is also interest in light-mass DM, below $10 \, \text{GeV}/c^2$, prompted by, e.g., asymmetric models [4, 5] and claims of DM observations [6, 7]. Light-mass DM would yield low-energy events that are close to the experimental energy threshold of liquid-xenon detectors. Therefore, exploiting an approach that lowers the threshold [8], we investigate the spin-independent WIMP-nucleon cross section versus mass parameter space extending the XENON100 results for masses below $\sim 7.4 \, \text{GeV}/c^2$.

II. THE XENON100 DETECTOR

The XENON100 detector [9] is a dual-phase (liquid-gas) xenon time projection chamber (TPC) located in the Laboratori Nazionali del Gran Sasso (LNGS). The TPC detection principle allows for measurements of nuclear recoils (NR) and electronic recoils (ER) through two signals: a prompt scintillation signal S1 and an ionization signal S2. The S1 signal is scintillation light from the rapid deexcitation of excited liquid xenon molecular states after an ionizing particle deposits energy. This deposition also liberates electrons, which drift in an electric field of $530 \, \text{V/cm}$ toward the liquid-gas interface, where a larger field of $\sim 12 \, \text{kV/cm}$ extracts them from the liquid. These accelerated electrons generate proportional scintillation in the xenon gas above the liquid.

Two arrays of 178 1"-square Hamamatsu R8520-AL PMTs are installed above and below the 62-kg xenon target. They detect both signals from the target. The distribution of the S2 signal among the top PMTs gives the projection of the interaction position on the PMT plane, while the relative time between the S1 and S2 signals provides the depth of the interaction, or z coordinate. We distinguish ER and NR by the ratio of their respective S1 and S2 signals. A trigger identifies S2 signals, and the waveform of each PMT is digitized in the interval between $200 \, \mu s$ before and after the trigger. The time for an electron to drift from the cathode to anode, or the maximum drift time, is $176 \, \mu s$ [9]. The TPC is surrounded by an active veto region consisting of 99 kg of liquid xenon, instrumented with 64 PMTs optically isolated from the TPC.

In previous XENON100 analyses [10, 11], the recoil energy has been determined using the size of the S1 signal and the relative scintillation efficiency for the nuclear re-coils, $\mathcal{L}_{\text{eff}}$, relative to the 122 keV calibration γ line of ^{57}Co [10]. WIMPs with a mass below $10 \, \text{GeV}/c^2$ create NRs only up to a few keV, resulting in an S2 signal lower than a few hundred photoelectrons (PE) and an S1 signal that is often not detectable. Therefore for this analysis we only use the S2 signal to infer the energy.

III. ANALYSIS

This analysis is performed using the data from XENON100's Science Run II, which collected a 225 live-day exposure between February 28, 2011 and March 31, 2012 [10]. For the WIMP analysis, we drop the requirement of observing an S1 signal. This allows us to lower the effective threshold at the cost of losing z coordinate reconstruction from the S2-S1 peak time difference and particle identification based on the S2/S1 signal ratio. We perform a background-limited analysis on this previously unblinded data set.

Both a NR and an ER within liquid xenon will produce an S2 signal. We use calibration data of ERs and NRs taken with external ^{60}Co/^{232}Th and ^{241}AmBe calibration sources, respectively. In these calibrations and in the DM search data, photo-ionization and delayed extraction of electrons produce signals that have a mean size of 20 PE per electron [12]. We restrict ourselves to charge signals above 80 PE, where the trigger efficiency is still at 80%, to minimize the background from these electrons. For the same reason, this value will be used as the lower threshold for the WIMP analysis.

Many processes besides WIMP interactions can create S2 or S2-like signals in our detector, e.g., radioactive backgrounds or photo-ionization of impurities or metallic surfaces in the TPC [12]. We use selection criteria to suppress these backgrounds in the DM search data. To begin, WIMPs are expected to interact uniformly in the liquid xenon target. In the DM search data, the event rate increases towards the radial edges of the detector because of radioactive backgrounds. Therefore, we require that the reconstructed radius of the event is less than 13.4 cm, which is approximately 2 cm from the TPC walls. This cut removes events from external backgrounds, which are stopped predominantly in the outer layers of the liquid target. The remaining liquid xenon target mass is 48.3 kg [13]. Within this target, the events are uniformly distributed radially, which means that a smaller fiducial volume does not reduce the background density.

Given an event with an S1 signal in the DM search data, we can use the information from that signal to isolate nuclear recoils using two additional cuts. First, the Monte Carlo nuclear-recoil model of [14] is used to determine a cut on the S1 size relative to the S2 size for any WIMP mass less than $20 \, \text{GeV}/c^2$. We parametrize this Monte Carlo model by requiring that a nuclear recoil has–if present–an S1 signal less than $[4.7 + 0.012 \times (\text{S2} - 80)] \, \text{PE}$. This cut has an acceptance of
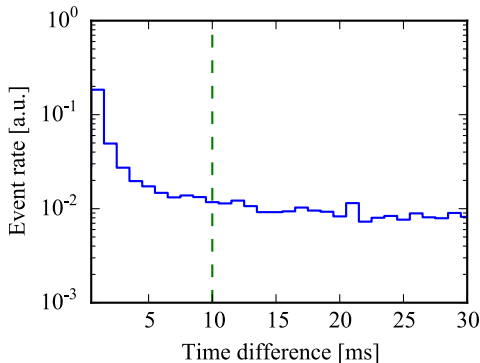
FIG. 1. Rate of events (S2 $>$ 80 PE) as a function of the time difference from the previous recorded event. A cut is set at 10 ms to remove a population of events of small S2 signals (e.g., photo-ionization) that appears within a few ms from the previous trigger.

FIG. 2. S2 asymmetry parameter for ^{241}AmBe calibration data in the liquid and a population of events produced in the xenon gas phase. We select interactions in the gas by requiring an S1 signal, small drift time, and a large S2 width using ^{60}Co and DM search data. An S2 asymmetry cut set at 0.17 is used to reject the gas event population in the dark matter data.

99.9% determined from the same Monte Carlo. Second, we can estimate the z position of the interaction from the drift time between the S1 and S2 signals. We require the z position to be more than 1.9 cm below the liquid-gas interface and more than 0.5 cm above the cathode. This condition decreases the fiducial volume by 8% and we conservatively assume an acceptance of 92% also for events without a detected S1 signal.

Secondary S2 signals can create events in which the main S2 signal is preceded or followed by similar nearby signals in the same event. These can be caused by multiple scatters in the active volume (i.e., not WIMPs) or misidentified detector artifacts. Additionally, any interaction in XENON100 can cause small S2 signals appearing up to milliseconds after the trigger, which are partly caused by photo-ionization on metal surfaces or impurities and possibly by delayed charge extraction as well [12].

We remove events which occur less than 10 ms after any other recorded event, resulting in a 2% live-time reduction. Figure 1 shows the event rate as a function of the time difference from the previous event. Signals caused by photo-ionization or delayed extraction are observed within a few ms from the previous event and are removed by this selection.

In the DM search data, we reject events with more than one S2 signal in the same event, e.g., multiple scatter events. If an S2 signal larger than 10 (30) PE is seen 176 μs before (after) the main S2 signal, the event is removed. The threshold after the main S2 signal is less strict since even a 250 PE S2 signal will itself create a secondary single-electron S2 signal ($\approx$ 20 PE [12]) by photo-ionization in 10% of the cases. The acceptance loss is 3% at S2 = 100 PE and slowly increasing for larger S2 signals, as estimated by a model of induced S2 signals similar to [12], but extended to low energies using the
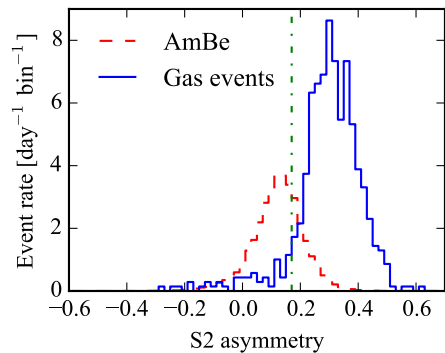
10 ms time difference cut.

For the following selection criteria, we estimate the acceptance on calibration data. For calibration events, to ensure that we only select valid low-energy events, we additionally require that the S1 signal observed in the TPC (at any size) has a coincident S1 signal in the veto region. We also apply the fiducial volume and single scatter selections as described above. In this way, we create a low-energy sample of real interactions. We use the fraction of events removed by the individual selection condition in the ^{241}AmBe calibration data [13]. ^{241}AmBe calibration was acquired before and after the DM search data. The acceptance for ^{241}AmBe taken at the end of the run is $\simeq$ 6% lower compared to ^{241}AmBe acquired at the beginning of the run. Conservatively, we choose ^{241}AmBe calibration data acquired at the end of the run to model the WIMP acceptance.

Events which contain too much electronic noise activity cannot be evaluated properly and are removed by comparing the area of the main S2 peak to the remaining baseline area. An S2 size-dependent threshold (the S2 pulse should contain at least 45% of the total area at 100 PE) was derived using ^{241}AmBe calibration data and leads to a 97% WIMP acceptance.

Finally, we apply a cut to remove events where the S2 signal is produced by an interaction in the gas between the anode and the top PMT screening electrode [9]. These are most likely caused by radioactivity from the top PMT array. In these so-called "gas events," a larger than average fraction of the S2 light is seen by the top PMT array since the S2 signal is produced close to it. The S2 signal is also wider than an S2 produced in the liquid since the luminescence region is typically twice as wide and–if an S1 signal is detected–it occurs very

TABLE I. Acceptances of the different data selections and number of DM candidate events passing the selections. The cuts are applied sequentially. The number of events is in the S2 energy range [80, 1000] PE.

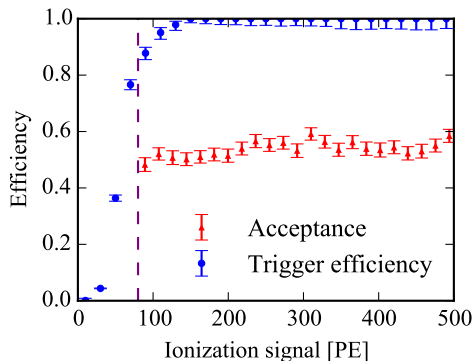| Description of cut	Acceptance at S2=100 PE	Events
Radial cut (starting events)	100%	254901
Depth and electronic recoil	92%	103914
Detector noise	97%	57516
Single S2 and 10 ms cut	95%	49041
Interaction in the gas	61%	13560

FIG. 3. The analysis acceptance (red triangles) and the trigger efficiency (blue circles). The purple dashed line is the analysis threshold (80 PE).

shortly before the S2. Therefore, we define an asymmetry parameter $(S2_{top} - S2_{bottom}) / (S2_{top} + S2_{bottom})$, corresponding to the fraction of observed light in the top PMTs compared to the bottom PMTs.

In Fig. 2, the asymmetry parameter is shown for [241]AmBe events that occurred in the liquid xenon and a sample of events from interactions in the gas phase. The gas events are taken from ^{60}Co and DM search data, requiring an S1 signal and selecting events where the S2 width at 10% peak height is inconsistent with diffusion broadening given the drift time of the event. Both distributions are normalized to the rate expected in the DM search data. The events in the liquid should be primarily due to ERs from background γs, so we estimate the rate by comparing the rate of ^{60}Co events and DM search data events at energies far beyond the region of interest, as done in [13]. The gas event rate was estimated from DM search data events with an S2 asymmetry larger than 0.45 (again, well beyond the region of interest), as seen in Fig. 2.

We remove events with an S2 asymmetry parameter larger than 0.17 and smaller than an S2 size-dependent threshold derived from [241]AmBe (-0.32 at 100 PE). The 0.17 threshold is chosen by optimizing the ratio of the

liquid events over the square root of gas events. Only 61% of liquid events with an S2 signal of 100 PE will pass the asymmetry cut (as determined from the [241]AmBe data). The low acceptance is necessary because of the gas event background in this analysis. We also apply a loose S2 10%-width selection of [0.8, 2.7] μs with an acceptance of 99.8% at S2=100 PE.

Figure 3 shows the analysis acceptance and the trigger efficiency [13] as a function of the S2 signal size. The trigger efficiency in our region of interest is more than 80%. The product of the trigger efficiency and analysis acceptance is our final signal detection efficiency. Table I shows the acceptance of the analysis selections discussed above, as well as the number of events remaining at each stage. After applying the data selection cuts summarized in Table I to the the entire data set of 30 kg × yr, 13560 valid candidate events remain in the S2 range [80, 1000] PE (see Fig. 4).
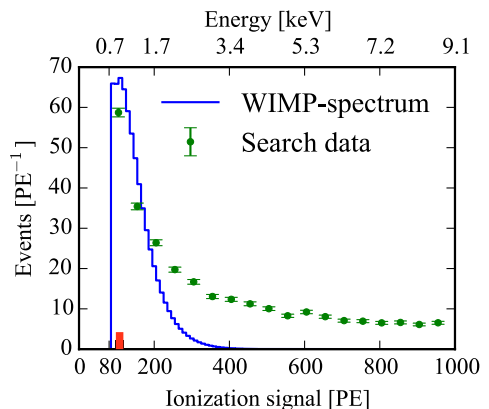
FIG. 4. Energy distribution of the events remaining in the data set after all data selection cuts. As an example, the expected spectrum for a WIMP of 6 GeV/c^2 and a spin-independent WIMP-nucleon scattering cross section of 1.5×10^{-41} cm^2 is also shown. The corresponding nuclear recoil energy scale is indicated on the top axis. The charge yield model assumed here has a cutoff at 0.7 keV, which truncates the WIMP spectrum. The optimum interval (thick red line) is found in the S2 range [98, 119] PE and contains 1173 events.

IV. RESULTS

The interpretation of the outcome of the data selection requires the reconstruction of a nuclear recoil equivalent energy scale from the measured S2 signals. It is based on two quantities: the first one is the charge yield Q_y, shown in Fig. 5, which gives the number of ionization electrons per keV liberated by a NR event. The second one is the secondary scintillation gain Y, which is detector-
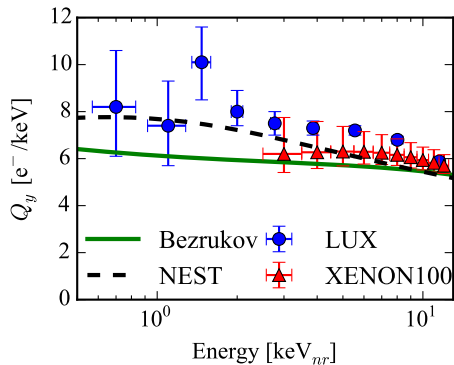
FIG. 5. Charge yield (Q_y) as a function of energy for nuclear recoils (keV). This analysis employs the conservative nuclear recoil charge yield model of Bezrukov *et al.* (electric field independent) [15], given by the green line. It agrees with the measurement of XENON100 (E = 0.53 kV/cm) [14] (red triangles). The NEST model (E = 0.73 kV/cm) [16] (dashed black) and the recent measurement of LUX (E = 0.18 kV/cm) [17] (blue points) predict slightly higher yields. To account for the mild discrepancies below 3 keV, we use the model from Bezrukov *et al.* and conservatively assume Q_y=0 below 0.7 keV.

dependent and gives the number of proportional scintillation photoelectrons per electron extracted into the gas phase. In this science run of XENON100, Y is described by a normal distribution with $\mu = (19.7 \pm 0.3)\,\mathrm{PE/e^-}$ and $\sigma = (6.9 \pm 0.3)\,\mathrm{PE/e^-}$ [12]. Charge extraction from the liquid is almost unity at the XENON100 extraction field [9].

As shown in Fig. 5, there is some remaining uncertainty in Q_y, especially at very low recoil energies, even though the LUX data demonstrate clearly that Q_y is nonzero above 0.7 keV [17]. In order to not base our WIMP result on optimistic assumptions, we use the analytical model of Bezrukov *et al.* [15], which agrees with the XENON100 measurement [14], and the NEST model [16] above ~6 keV and is more conservative at lower energies. We additionally introduce a cutoff at 0.7 keV, below which Q_y is set to zero, to penalize the result for the limited knowledge on the charge yield at the lowest energies. This energy also corresponds to the threshold at which signals will be above our 80 PE threshold.

However, we note that a Monte Carlo model based on the Bezrukov *et al.* function without any cutoff leads to a good description of the measured charge spectrum from ^{241}AmBe calibration data (see Fig. 6). The data were selected based on the same criteria as used in the WIMP analysis, with the exception of the S2 asymmetry cut, which is not required due to the significantly higher rate of the ^{241}AmBe source compared to the gas event rate. Besides the statistical uncertainty, the spectrum also in-
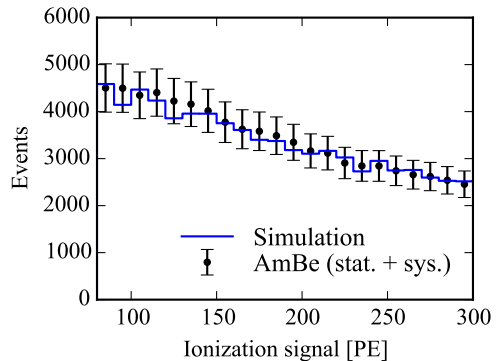
FIG. 6. S2 spectrum of ^{241}AmBe calibration data compared to simulations using the Q_y from Bezrukov *et al.* [15] with no energy cutoff.
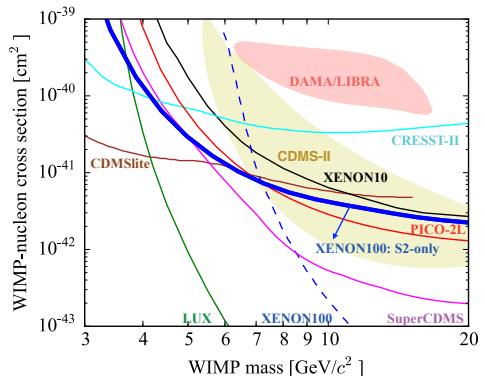
FIG. 7. WIMP exclusion limit on the spin-independent WIMP-nucleon scattering cross section at 90% confidence level. Limits from the LUX [21], XENON100 [10], Super-CDMS [22], CDMSlite [23], XENON10 [8], CRESST-II [24] and PICO-2L [25] experiments are shown. The claims from DAMA/LIBRA experimental data [26] and CDMS-II (Si detectors) [7] are also shown. The limit from this analysis is shown with the thick blue line and it improves the XENON100 result [10] (dashed blue line) for WIMP masses below ~7.4 GeV/c^2.

cludes a systematic uncertainty of 8%, which is mainly due to the uncertainties in the S2 amplification [12] and the cut acceptance. The simulation follows the strategy described in [14] but ignores the S1 light information.

The same Monte Carlo method is used to model the expected WIMP energy spectra. The number of electrons released after a nuclear recoil of energy E is given by a Poisson distribution with mean $N = EQ_y$. The charge loss due to the electron lifetime (τ_e) is modeled

per event as an exponential reduction in the number of electrons, though this effect is small due to the average $\langle \tau_e \rangle = 570\,\mu$s. The evolution of τ_e throughout the 225 days is modeled as in previous work [13]. The secondary scintillation is modeled using the measured parameters given above and in [12]. A Maxwell-Boltzmann distribution with the asymptotic velocity of the local system $v_0 = 220\,$km/s, the solar velocity $v_{sun} = 232\,$km/s and the galactic escape velocity $v_{esc} = 544\,$km/s is used to model the DM halo, assuming a local WIMP density of $\rho_0 = 0.3\,$GeV/$(c^2 \times$cm$^3)$ [18]. As an example, Fig. 4 shows the NR spectrum, as parametrized in [19], induced by a $6\,$GeV/c^2 WIMP at a spin-independent cross section of $\sigma = 1.5 \times 10^{-41}\,$cm^2. We observe an event rate of $\sim 0.5\,$events/(keV$\times$kg$\times$day) between 0.7 and 1.7 keV that drops to $\sim 0.07\,$events/(keV$\times$kg$\times$day) between 3.4 and 9.1 keV.

In the absence of a full background model, which cannot be constructed as the origin of the small-S2 background in the detector cannot be reliably quantified, we assume that every event passing the analysis cuts could be due to a DM interaction. The analysis employs the optimum interval method [20] and will therefore always lead to an exclusion limit. The optimum S2 interval varies with WIMP mass, but in all cases in this analysis, it contains a minimum of 1000 events passing all cuts. The low-mass WIMP result for this $30\,$kg $\times$ yr XENON100 exposure is based on all events remaining in the 80-1000 PE interval (0.7-9.1 keV), the NR acceptance of Fig. 3, and is shown in Fig. 7. At a WIMP mass of $6\,$GeV/c^2, XENON100 excludes spin-independent WIMP-nucleon interaction cross sections of $1.4 \times 10^{-41}\,$cm^2 at 90% confidence level. The moderate improvement upon the XENON10 low-mass result [8], despite the much larger exposure, is due to the significantly higher background from photo-ionization events, which is enhanced by the presence of larger metal surfaces inside the TPC. The new result challenges a standard WIMP interpretation of the DAMA/LIBRA modulation signal, excludes large fractions of the CDMS-II (Si) preferred region and improves the result of the previous XENON100 result [10] below $\sim 7.4\,$GeV/c^2. We improve the LUX [21] (SuperCDMS [22]) results below ~ 3.7 (5.3) GeV/c^2.

[1] P.A.R. Ade *et al.* (Planck Collaboration), Astron. Astrophys. **594**, A13 (2016)
[2] M. W. Goodman and E. Witten, Phys. Rev. D **31**, 3059 (1985).
[3] G. Jungman, M. Kamionkowski, and K. Griest, Phys. Rep. **267**, 195 (1996).
[4] D. E. Kaplan, M. A. Luty, and K. M. Zurek, Phys. Rev. D **79**, 115016 (2009).
[5] T. Lin, H.B. Yu, and K.M. Zurek, Phys. Rev. D **85** 063503 (2012).
[6] R. Bernabei *et al.* (DAMA/LIBRA Collaboration), Eur. Phys. J. C **73**, 2648 (2013).
[7] R. Agnese *et al.* (CDMS-II Collaboration), Phys. Rev. Lett. **111**, 251301 (2013).
[8] J. Angle *et al.* (XENON10 Collaboration), Phys. Rev. Lett. **107**, 051301 (2011).
[9] E. Aprile *et al.* (XENON100 Collaboration), Astropart. Phys. **35**, 573 (2012).
[10] E. Aprile *et al.* (XENON100 Collaboration), Phys. Rev. Lett. **109**, 181301 (2012).
[11] E. Aprile *et al.* (XENON100 Collaboration), Phys. Rev. Lett. **111**, 021301 (2013).
[12] E. Aprile *et al.* (XENON100 Collaboration), J. Phys. G: Nucl. Part. Phys. **41**, 035201 (2014).
[13] E. Aprile *et al.* (XENON100 Collaboration), Astropart. Phys. **54**, 11 (2014).
[14] E. Aprile *et al.* (XENON100 Collaboration), Phys. Rev. D **88**, 012006 (2013).
[15] F. Bezrukov, F. Kahlhoefer, and M. Lindner, Astropart. Phys. **35**, 119 (2011).
[16] B. Lenardo, K. Kazkaz, A. Manalaysay, J. Mock, M. Szydagis, and M. Tripathi, IEEE Trans. Nucl. Sci. **62**, 3387 (2015).
[17] D. S. Akerib *et al.* (LUX Collaboration), arXiv:1608.05381 (2016).
[18] A. M. Green, Mod. Phys. Lett. A **27**, 1230004 (2012).
[19] J.D. Lewin, and P.F. Smith, Astropart. Phys. **6**, 87 (1996).
[20] S. Yellin, Phys. Rev. D **66**, 032005 (2002).
[21] D. S. Akerib *et al.* (LUX Collaboration), Phys. Rev. Lett. **116**, 161301 (2016).
[22] R. Agnese *et al.* (SuperCDMS Collaboration), Phys. Rev. Lett. **112**, 241302 (2014).
[23] R. Agnese *et al.* (SuperCDMS Collaboration), Phys. Rev. Lett. **116**, 071301 (2016).
[24] G. Angloher *et al.* (CRESST Collaboration), Eur. Phys. J. C **76**, 25 (2016).
[25] C. Amole *et al.* (PICO Collaboration), Phys. Rev. D **93**, 061101(R) (2016).
[26] C. Savage, G. Gelmini, P. Gondolo and K. Freese, J. Cosmol. Astropart. Phys. **04** (2009) 010.

6

Outlook

Experiments searching for the interaction of WIMPs in deep-underground detectors have improved their sensitivity by seven orders of magnitude over the last 30 years. This rapid progress in the sensitivity of WIMP experiments has mainly been driven by innovations in the detector technology that allowed to construct bigger detectors and by the suppression of the backgrounds.

Firstly, the evolution of the sensitivity during the last 30 years is presented from the first results in 1985 to the recent results in 2017. Finally, the main experiments planned in the next decade are described, focusing on the long-term outlook for the direct detection field.

6.1 Historical reflection and current state-of-affairs

Fig. 6.1 shows the evolution of the sensitivity for the WIMP-nucleon cross section at a WIMP mass of 50 GeV from the first results in 1985 to the latest results in 2017 reported by the XENON1T experiment. WIMP searches began in the late 1980s with germanium detectors which excluded a WIMP-nucleon cross section larger than $10^{-40}\,\mathrm{cm}^2$. Subsequently, the sensitivity improved by about 2-3 orders of magnitude using better and larger mass cryogenic solid state detectors like CDMS.

From 2007 onward, xenon-based detectors have become the most sensitive experiments. The XENON100 experiment, featured in this work, operated for about 5 years without finding evidence for WIMPs. The XENON100 experiment excluded a WIMP-nucleon cross section larger than $1.1 \times 10^{-45}\,\mathrm{cm}^2$ at a WIMP mass of 50 GeV. The sensitivity has been improved by an order of magnitude by other xenon-based detectors. The LUX and the PANDA-X experiment excluded a WIMP-nucleon cross section

larger than $1.1 \times 10^{-46}\,\mathrm{cm}^2$ and $2.5 \times 10^{-46}\,\mathrm{cm}^2$, respectively.

With backgrounds present, the WIMP exclusion limit improves as the square root of the exposure due to statistical fluctuations in the background subtraction. Since the mass of the XENON100 detector can not be increased, continuing to acquire data would improve the latest XENON100 results only marginally. Therefore, running further the XENON100 detector would not increase our chances to discover WIMPs, nor would it improve the sensitivity.
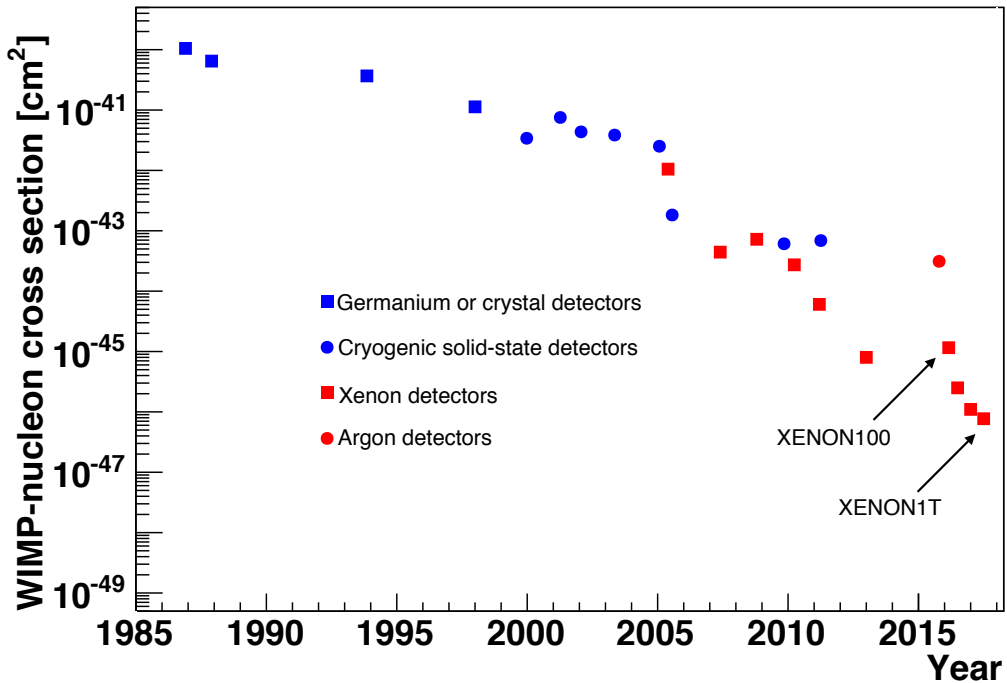
Figure 6.1: *Evolution during the years of the sensitivity at a WIMP mass of 50 GeV for different direct detection experiment technologies.*

To increase our chances to discover WIMPs, the XENON collaboration has been focusing on the construction and the operation of the next-generation experiment of the XENON project, XENON1T. XENON1T is the first xenon-based ton-scale detector, and it has recently reported its first Dark Matter result [75] (Fig. 2.9), becoming the most sensitive WIMP experiment in the world at the time of writing.

To achieve this result, the XENON1T collaboration has operated a dual-phase TPC containing $3.2\,\mathrm{t}$ of xenon with a target mass of $2\,\mathrm{t}$ [75]. The target mass is more than a factor 30 larger than the XENON100 experiment, being one of the main reasons that

allowed XENON1T to become the most sensitive experiment in the world. Another main driver of the sensitivity of the XENON1T experiment is the suppression of the backgrounds. The reduction in the background level is mostly determined by the water shield around the detector, as well as a careful screening campaign to reduce the residual radioactivity in the construction materials and the reduction of the internal backgrounds.

Figure 6.2: *A picture of the XENON1T detector.*

The XENON1T detector is shown in Figure 6.2. From the figure, we can see that the cryostat is freely suspended from three rods, which are attached to the top of a stainless steel support structure. Both the cryostat and the support structure are located inside a stainless steel tank containing water. The water is instrumented with PMTs to detect the cherenkov light emitted by cosmic-ray induced muons. These muons can produce neutrons that can then interact in the TPC target volume mimicking WIMP-induced nuclear recoils. If a nuclear recoil is recorded just after the detection of the cherenkov light, the event is not considered as a valid WIMP candidate because it is likely to be induced by a muon. In this way, the irreducible muon-induced background is suppressed to negligible levels in XENON1T [123]. A picture taken during the filling of the tank with water is shown in Fig. 6.3.

With the muon-induced background at a negligible level, the main contribution to the nuclear recoil background is due to the residual radioactivity in the construction

materials. Thanks to the large xenon mass which shields the target volume and a careful screening campaign, the nuclear recoil background in XENON1T is estimated to amount to only 0.6 ± 0.1 events per ton $\times$ year [123]. For comparison, the neutron recoil background in XENON100 was 8 events per ton $\times$ year.
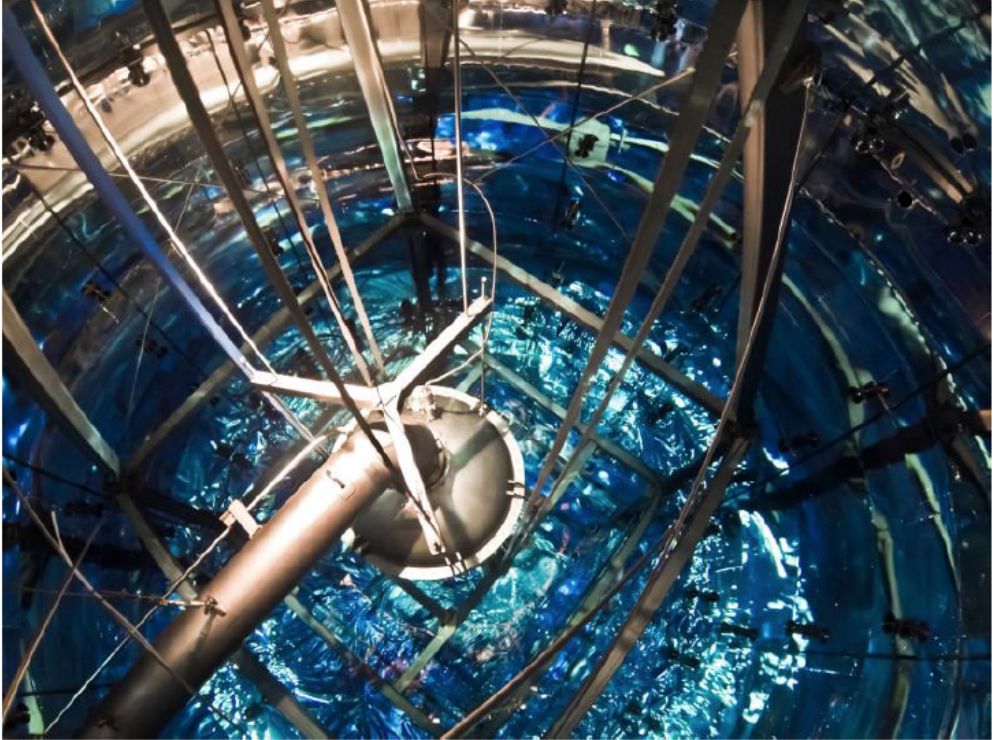
Figure 6.3: *A picture taken during the filling of the water tank.*

The background expected from electronic recoils is also significantly reduced compared to XENON100. The main background contribution for XENON1T is due to the radon-induced background, while other backgrounds are negligible[1]. The radon-induced background causes 1.5 ± 0.1 events per ton $\times$ year in XENON1T [123]. For comparison, the electronic recoil background in XENON1T is reduced by more than a factor of 40 compared to XENON100 where the expected background from electronic recoils was 72 events per ton $\times$ year.

---

[1]The expected background from krypton is a factor 10 lower compared to the radon-induced background, due to the reduction of the natural krypton concentration from 19 ppt in XENON100 to 0.2 ppt in XENON1T. The background from the construction materials is also more than a factor 10 lower compared to the radon-induced background.

Given the large target mass and the very low background levels, the XENON1T experiment is expected to further improve its sensitivity by about a factor of 5 after a $2\,\text{ton} \times$ year exposure, possibly showing the first signs of WIMPs. The best sensitivity is expected to be achieved at a WIMP mass of 50 GeV/c^2 reaching a WIMP-nucleon cross section of 1.6×10^{-47} cm^2.

6.2 Long-term future

Fig. 6.4 shows the sensitivity for the WIMP-nucleon cross section as a function of the WIMP mass for the experiments that have already published their results and for some experiments planned to start the data taking within the next ten years.
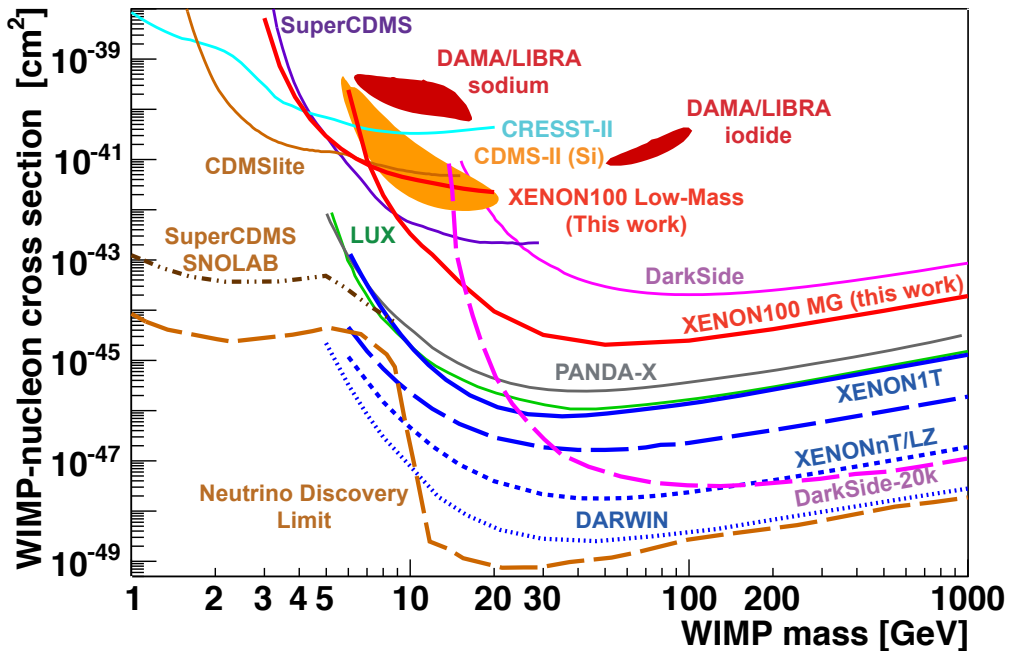
Figure 6.4: *WIMP-nucleon cross section as a function of the WIMP mass. The expected sensitivity of the next-generation experiments is shown with dashed lines, while the excluded WIMP-nucleon cross section by different experiments is shown with solid lines. The contributions from this thesis are highlighted in red.*

After the XENON1T experiment will complete its science program, the XENONnT experiment will improve the XENON1T sensitivity by about a factor of 10. XENONnT will use the infrastructure of the XENON1T experiment, e.g. the same water tank, support structure and cryostat. The xenon target is designed to be about 8 t using an

enlarged TPC and an enlarged inner cryostat, while the assumed exposure will be 20 ton × year. Similarly, the LUX collaboration has planned the LZ experiment which will have a similar target mass and sensitivity compared to XENONnT. The ultimate xenon TPC will be the DARWIN experiment, which will have a target mass of about 50 t and an exposure of 200 ton × year. The DARWIN experiment is expected to improve by about a factor of 10 the XENONnT/LZ sensitivity at a WIMP mass of 50 GeV.

For argon-based experiments, the DarkSide collaboration proposes a 20 t (DarkSide-20k) argon TPC. Due to the superior rejection of electronic recoils using pulse shape discrimination techniques in argon-based experiments, at larger recoil energies (section 2.3), DarkSide-20k will have a better sensitivity compared to the XENONnT/LZ experiment for a WIMP with a mass larger than about 300 GeV.

For low-mass WIMPs, due to the lower energy threshold achievable using cryogenic solid-state detectors, the SuperCDMS SNOLAB experiment [124] is expected to achieve the best WIMP-exclusion limit for WIMP-masses below about 5 GeV, with a sensitivity of about $10^{-43}\,\mathrm{cm^2}$ for WIMPs with a mass between 1 and 5 GeV.

When WIMP detectors will increase their size, they will eventually become sensitive to neutrinos from astrophysical sources: solar neutrinos, atmospheric neutrinos, and diffuse supernova neutrinos (the neutrino flux coming from the past history of all supernova explosions in the Universe [125]) can mimic a WIMP signal. The main background will be determined by neutrino-induced nuclear recoils from coherent neutrino-nucleus scattering[1].

Neutrino-induced nuclear recoils can not be distinguished from the WIMP-induced nuclear recoils, and the coherent neutrino-nucleus scattering will constitute an irreducible background to discover WIMPs (neutrino discovery limit in Fig. 6.4) for the WIMP experiments described in this work. However, direction-sensitive detectors can potentially overcome the neutrino discovery limit using the discrimination of nuclear recoils coming from the CYGNUS direction - expected from WIMPs - and nuclear recoils coming from the other directions - expected from the neutrino backgrounds.

Before reaching the neutrino discovery limit, there are still three orders of magnitude in the WIMP-nucleon cross section versus the WIMP mass parameter space to be explored. Experiments planned to start in the next decade will definitely have an exciting time ahead to try to discover WIMPs, or in the worst case scenario further extend the sensitivity to WIMPs. In both cases, our understanding of the WIMP properties will increase, enlightening the nature and properties of the Dark Matter

---

[1]The coherent neutrino-nucleus scattering is expected from standard model physics. The next-generation WIMP detectors will allow to precisely measure the coherent neutrino-nucleus scattering.

content of the universe.

Bibliography

[1] F. HALZEN, A. D. MARTIN. *Quarks and Leptons: An Introductory Course in Modern Particle Physics.* 1986.

[2] **http://home.cern/topics/large-hadron-collider**.

[3] XENON100 COLLABORATION. **XENON100 Dark Matter Results from a Combination of 477 Live Days**. *Phys. Rev. D*, **94, 122001**, 2016.

[4] XENON100 COLLABORATION. **Low-mass dark matter search using ionization signals in XENON100**. *Phys. Rev. D*, **94, 092001**, 2016.

[5] A. LIDDLE. *An Introduction to Modern Cosmology.* 2003.

[6] R. A. ALPHER, H. BETHE, G. GAMOW. **The Origin of Chemical Elements**. *Physical Review*, **73, 803**, 1948.

[7] K.A. OLIVE ET AL. (PARTICLE DATA GROUP). **2015 Review of Particle Physics 2015 (chapter 22)**. *Chin. Phys. C*, **38, 090001**, 2014.

[8] J. BERINGER ET AL. (PARTICLE DATA GROUP). **2013 Review of Particle Physics (chapter 22)**. *Phys. Rev. D*, **86, 010001**, 2012.

[9] H. GEORGI, S. L. GLASHOWS. **Unity of All Elementary-Particle Forces**. *Phys. Rev. Lett.*, **32, 438**, 1974.

[10] A. GUTH. **Inflationary universe: A possible solution to the horizon and flatness problems**. *Phys. Rev. D*, **23, 347**, 1982.

[11] PLANCK COLLABORATION. **Planck 2015 results. XIII. Cosmological parameters**. *AA*, **594, A13**, 2016.

[12] A. PENZIAS, R. WILSON. **A Measurement of the Flux Density of CAS A At 4080 Mc/s**. *Astrophysical Journal Letters*, **142**:1149–1154, 1965.

[13] http://www.cpepweb.org/main_universe/images/universe_original.jpg.

[14] A. EINSTEIN. **The Foundation of the General Theory of Relativity**. *Annalen der Physik*, 1916.

[15] A. FRIEDMANN. **Uber die Krummung des Raumes**. *Zeitschrift für Physik*, 1922.

[16] J. L. CERVANTES-COTA, G. SMOOT. **Cosmology today - A brief review**. *AIP Conf. Proc.*, **1396**:28–52, 2011.

[17] S. PERLMUTTER ET AL. **Measurements of Ω and Λ from 42 high redshift supernovae**. *Astrophysical Journal*, **517**:565–586, 1999.

[18] A. G. RIESS ET AL. **Observational evidence from supernovae for an accelerating Universe and a cosmological constant**. *Astronomical Journal*, **116**:1009–1038, 1998.

[19] D.EISENSTEIN AT AL. **SDSS-III: massive spectroscopic surveys of the distant universe, the milky way galaxy, and extra-solar planet system**. *Astronomical Journal*, **142:72**, 2011.

[20] THE SUPERNOVA COSMOLOGY PROJECT. **The Hubble space telescope cluster supernova survey: v. improving the dark energy constraints above z > 1 and building an early-type-hosted supernova sample**. *Astrophysical Journal*, **746, 85**, 2012.

[21] WMAP COLLABORATION. **Seven-Year Wilkinson Microwave Anisotropy Probe (WMAP1) Observations: Sky Maps, Systematic Errors, and Basic Results**. *Astrophysical Journal Supplement Series*, **192, 14**, 2011.

[22] JR. V. C. RUBIN, W. K. FORD. **Rotation of the Andromeda Nebula from a Spectroscopic Survey of Emission Regions**. *Astrophysics Journal*, **159**:379–404, 1970.

[23] E. CORBELLI, P. SALUCCI. **The extended rotation curve and the dark matter halo of M33**. *Monthly Notices of the Royal Astronomical Society*, **311**:441–447, 2000.

[24] M. ROOS. **Dark Matter: The evidence from astronomy, astrophysics and cosmology**. *arXiv:1001.0316v2*, 2010.

[25] J. H. OORT. **The force exerted by the stellar system in the direction perpendicular to the galactic plane and some related problems**. *Bulletin of the Astronomical Institutes of the Netherlands*, **6**:249–287, 1932.

[26] D. CLOWE ET AL. **A Direct empirical proof of the existence of Dark Matter**. *Astrophysics Journal*, **648**:L109–L113, 2006.

[27] R. SCHON. *XAMS Development of liquid xenon detector technology for dark matter searches*. PhD thesis, University of Amsterdam, 2015.

[28] **http://www.esa.int/spaceinimages/Images/2013/03/Planck_CMB**.

[29] K. NAKAMURA ET AL. (PARTICLE DATA GROUP). **2011 Review of Particle Physics (chapter 21)**. *J. Phys. G: Nucl. Part. Phys.*, **37, 075021**, 2010.

[30] **http://www.esa.int/spaceinimages/Images/2013/03/ Planck_Power_Spectrum**.

[31] PLANCK COLLABORATION. **Planck 2013 results. XVI. Cosmological parameters**. *AA*, **571, A16**, 2014.

[32] P. HUT. **Limits on masses and number of neutral weakly interacting particles**. *Phys. Lett. B*, **69**:85–88, 1987.

[33] J. BINNEY, S. TREMAINE. *Galactic Dynamics*. Princeton series in astrophysics, 1987.

[34] J. L. FENG. **Dark Matter Candidates from Particle Physics and Methods of Detection**. *Ann. Rev. Astron. Astrophys.*, **48: 495**, 2010.

[35] G. BERTONE. *Particle Dark Matter: Observational, Models and Searches*. Cambridge University Press, 2010.

[36] G. JUNGMAN, M. KAMIONKSWKI, K. GRIEST. **Supersymmetric Dark Matter**. *Physics Reports*, **267**:195–373, 1996.

[37] S. P. MARTIN. **A Supersymmetry Primer**. *arXiv:hep-ph/9709356v6*, 2011.

[38] ATLAS COLLABORATION. **Search for dark matter in events with heavy quarks and missing transverse momentum in pp collisions with the ATLAS detector**. *Eur. Phys. J. C*, **75:92**, 2015.

[39] ATLAS COLLABORATION. **Search for dark matter candidates and large extra dimensions in events with a photon and missing transverse momentum in pp collision data at $\sqrt{s} = 7$ TeV with the ATLAS detector**. *Phys. Rev. Lett.*, **110, 011802**, 2013.

[40] ATLAS COLLABORATION. **Search for dark matter in events with a Z boson and missing transverse momentum in pp collisions at $\sqrt{s} = 8$ TeV with the ATLAS detector**. *Phys. Rev. D.*, **90, 012004**, 2014.

[41] ATLAS COLLABORATION. **Search for Dark Matter in Events with Missing Transverse Momentum and a Higgs Boson Decaying to Two Photons in pp Collisions at $\sqrt{s} = 8$ TeV with the ATLAS Detector**. *Phys. Rev. Lett.*, **115, 131801**, 2015.

[42] ATLAS COLLABORATION. **Search for Dark Matter in Events with a Hadronically Decaying W or Z Boson and Missing Transverse Momentum in pp Collisions at $\sqrt{s} = 8$ TeV with the ATLAS Detector**. *Phys. Rev. Lett.*, **112, 041802**, 2014.

[43] ATLAS COLLABORATION. **Search for new phenomena in final states with an energetic jet and large missing transverse momentum in pp collisions at $\sqrt{s}$=13 TeV using the ATLAS detector**. *Phys. Rev. D*, **94, 032005**, 2016.

[44] CMS COLLABORATION. **Search for dark matter, extra dimensions, and unparticles in monojet events in proton-proton collisions at $\sqrt{s} = 8$ TeV**. *Eur. Phys. J. C*, **75:235**, 2015.

[45] CMS COLLABORATION. **Search for the production of dark matter in association with top-quark pairs in the single-lepton final state in proton-proton collisions at $\sqrt{s} = 8$ TeV**. *Journal of High Energy Physics*, **2015: 121**, 2015.

[46] S. SIVERTSSON, J. EDSJO. **Accurate calculations of the WIMP halo around the Sun and prospects for its gamma-ray detection**. *Phys. Rev. D*, **81, 063502**, 2010.

[47] HAMISH SILVERWOOD. *The Dark that shapes the light*. PhD thesis, University of Amsterdam, 2016.

[48] IceCube collaboration. **Search for dark matter annihilations in the Sun with the 79-string IceCube detector**. *Phys. Rev. Lett.*, **110, 131302**, 2013.

[49] Super-Kamiokande collaboration. **Search for neutrinos from annihilation of captured low-mass dark matter particles in the Sun by Super-Kamiokande**. *Phys. Rev. Lett.*, **114, 141301**, 2015.

[50] KM3Net collaboration. **Letter of Intent for KM3NeT 2.0**. *J. Phys. G: Nucl. Part. Phys.*, **43 (8), 084001**, 2016.

[51] **http://fermi.gsfc.nasa.gov/science/instruments/lat.html**.

[52] L. Bergstrom. **Dark matter and imaging air Cherenkov arrays**. *Astropart. Phys.*, **43**:44–49, 2013.

[53] **http://fermi.gsfc.nasa.gov/**.

[54] J. Kopp, V. Niro, T. Schwetz, J. Zupan. **Leptophilic Dark Matter in Direct Detection Experiments and in the Sun**. *arXiv:1011.1398*.

[55] J. I. Read. **The Local Dark Matter Density**. *J. Phys. G: Nucl. Part. Phys.*, **41, 063101**, 2014.

[56] R. W. Schnee. **Introduction to Dark Matter Experiments**. *arXiv:1101.5205v1*, 2011.

[57] LUX collaboration. **Results from a search for dark matter in the complete LUX exposure**. *Phys. Rev. Lett.*, **118, 021303**, 2017.

[58] J.D. Lewin, P.F. Smith. **Review of mathematics, numerical factors, and corrections for dark matter experiments based on elastic nuclear recoil**. *Astropart. Phys.*, **6**:87–112, 1996.

[59] K. Freese, M. Lisanti, C. Savage. **Annual Modulation of Dark Matter: A Review**. *Rev. Mod. Phys.*, **85, 1561**, 2013.

[60] **http://www.djsadhu.com/audio-video/audio-production/solar-system-2-0-new-animation/**.

[61] F. Donato, N. Fornengo, S. Scopel. **Effects of galactic dark halo rotation on WIMP direct detection**. *Astropart. Phys.*, **9**:247–260, 1998.

[62] G. Duda, A. Kemper, P. Gondolo. **Model Independent Form Factors for Spin Independent Neutralino-Nucleon Scattering from Elastic Electron Scattering Data**. *JCAP*, **0704:012**, 2007.

[63] M.T. Ressell, D.J. Dean. **Spin-Dependent Neutralino-Nucleus Scattering for A $\approx$ 127 Nuclei**. *Phys. Rev. C*, **56**:535–546, 1997.

[64] J. Menendez, D. Gazit, A. Schwenk. **Spin-dependent WIMP scattering off nuclei**. *Phys. Rev. D*, **86, 103511**, 2012.

[65] Sonja Orrigo. **Direct Dark Matter Search With XENON100 at RICAP14**, 2014.

[66] CoGenT collaboration. **Maximum Likelihood Signal Extraction Method Applied to 3.4 years of CoGeNT Data**. *arXiv:1401.6234v2*, 2014.

[67] DAMA Collaboration. **Final model independent result of DAMA/LIBRA-phase1**. *Eur. Phys. J. C*, **73:2648**, 2013.

[68] SuperCDMS collaboration. **Search for Low-Mass WIMPs with SuperCDMS**. *Phys. Rev. Lett.*, **112, 241302**, 2014.

[69] CRESST collaboration. **Results on light dark matter particles with a low-threshold CRESST-II detector**. *Eur. Phys. J. C*, **76:25**, 2015.

[70] LUX collaboration. **A Detailed Look at the First Results from the Large Underground Xenon (LUX) Dark Matter Experiment**. *arXiv:1402.3731v2*, 2014.

[71] PANDA-X collaboration. **Dark Matter Results from First 98.7-day Data of PandaX-II Experiment**. *Phys. Rev. Lett.*, **117, 121303**, 2016.

[72] Dark Side collaboration. **Dark Side Collaboration First Results from the DarkSide-50 Dark Matter Experiment at Laboratori Nazionali del Gran Sasso**. *Phys. Lett. B*, **743, 456**, 2015.

[73] P. Gorel. **Search for Dark Matter with Liquid Argon and Pulse Shape Discrimination: Results from DEAP-1 and Status of DEAP-3600**. *arXiv:1406.0462*.

[74] J. Mock et al. **Modeling Pulse Characteristics in Xenon with NEST**. *Journal of Instrumentation*, **9, T04002**, 2014.

[75] XENON1T collaboration. **First Dark Matter Search Results from the XENON1T Experiment**. *arXiv:1705.06655*, 2017.

[76] C. Savage, G. Gelmini, P. Gondolo, K. Freese. **Compatibility of DAMA/LIBRA dark matter detection with other searches**. *JCAP*, **0904:010**, 2009.

[77] CDMS collaboration. **Silicon Detector Dark Matter Results from the Final Exposure of CDMS II**. *Phys. Rev. Lett.*, **111, 251301**, 2013.

[78] SuperCDMS collaboration. **A Search for Low-Mass WIMPs using Voltage-Assisted Calorimetric Ionization Detection in the SuperCDMS Experiment**. *Phys. Rev. Lett.*, **112, 041302**, 2014.

[79] CRESST collaboration. **Results from 730 kg days of the CRESST-II Dark Matter search**. *Eur. Phys. J. C*, **72:1971**, 2012.

[80] XENON10 Collaboration. **A search for light dark matter in XENON10**. *Phys. Rev. Lett.*, **107, 051301**, 2011.

[81] LUX collaboration. **Limits on spin-dependent WIMP-nucleon cross section obtained from the complete LUX exposure**. *Phys. Rev. Lett.*, **118, 251302**, 2017.

[82] O. Buchmueller, M. J. Dolan, S. A. Malik, C. McCabe. **Characterising dark matter searches at colliders and direct detection experiments: Vector mediators**. *Journal of High Energy Physics*, **01 037**, 2015.

[83] PICO collaboration. **Dark Matter Search Results from the PICO-60 C3F8 Bubble Chamber**. *Phys. Rev. Lett.*, **118, 251301**, 2017.

[84] DAMA Collaboration. **Searching for WIMPs by the annual modulation signature**. *Phys. Lett. B*, **424**:195–201, 1998.

[85] J. L. Feng, J. Kumar, D. Sanford. **Xenophobic Dark Matter**. *Phys. Rev. D*, **88, 015021**, 2013.

[86] S. Chang, R. Edezhath, J. Hutchinson, M. Luty. **Leptophilic Effective WIMPs**. *Phys. Rev. D*, **90, 015011**, 2014.

[87] J. Kopp, V. Niro, T. Schwetz, J. Zupan. **DAMA/LIBRA and leptonically interacting Dark Matter**. *Phys. Rev. D*, **80, 083502**, 2009.

[88] XENON100 COLLABORATION. **Search for Event Rate Modulation in XENON100 Electronic Recoil Data**. *Phys. Rev. Lett.*, **115, 091302**, 2015.

[89] J. H. DAVIS. **The Past and Future of Light Dark Matter Direct Detection**. *Int. J. Mod. Phys. A*, **30, 1530038**, 2015.

[90] XENON100 COLLABORATION. **The XENON100 Dark Matter Experiment**. *Astropart. Phys.*, **35**:573–590, 2012.

[91] L. BAUDIS. **WIMP Dark Matter Direct-Detection Searches in Noble Gases**. *Physics of the Dark Universe*, **4**:50–59, 2014.

[92] V. CHEPEL, H. ARAUJO. **Liquid noble detectors for low energy particle physics**. *Journal of Instrumentation*, **8 R04001**, 2012.

[93] E. APRILE, T. DOKE. **Liquid Xenon Detectors for Particle Physics and Astrophysics**. *Rev. Mod. Phys.*, **82**:2053–2097, 2010.

[94] EXO COLLABORATION. **An improved measurement of the $2\nu\beta\beta$ half-life of Xe-136 with EXO-200**. *Phys. Rev. C*, **89, 015502**, 2014.

[95] M. SZYDAGIS ET AL. **NEST: A Comprehensive Model for Scintillation Yield in Liquid Xenon**. *Journal of Instrumentation*, **6, P10002**, 2011.

[96] C. SILVA, J. PINTO DA CUNHA, A. PEREIRA, V. CHEPEL, M. I. LOPES, V. SOLOVOV. **Reflectance of Polytetrafluoroethylene (PTFE) for Xenon Scintillation Light**. *Journal of Applied Physics*, **107, 064902**, 2009.

[97] M. WEBER. *Gentle Neutron Signals and Noble Background in the XENON100 Dark Matter Search Experiment*. PhD thesis, Heidelberg University, 2013.

[98] GUILLAME PLANTE. *The XENON100 Dark Matter Experiment: Design, Construction, Calibration and 2010 Search Results with Improved Measurement of the Scintillation Response of Liquid Xenon to Low-Energy Nuclear Recoils*. PhD thesis, Columbia University, 2012.

[99] XENON100 Collaboration. **Analysis of the XENON100 Dark Matter Search Data**. *Astropart. Phys.*, **54**:11–24, 2014.

[100] C. E. DAHL. *The physics of background discrimination in liquid xenon, and first results from XENON10 in the hunt for WIMP dark matter*. PhD thesis, Princeton University, 2009.

[101] J. Lindhard, V Nielsen, M. Scharff, P.V. Thomsen. **Integral equations governing radiation effects. (Notes on atomic collisions. III)**. *Mat. Fys. Medd. Dan. Vid. Selsk.*, **33**(14), 1963.

[102] XENON100 collaboration. **Observation and applications of single-electron charge signals in the XENON100 experimen**. *J. Phys. G: Nucl. Part. Phys.*, **41, 035201**, 2014.

[103] LUX collaboration. **Low-energy (0.7-74 keV) nuclear recoil calibration of the LUX dark matter experiment using D-D neutron scattering kinematics**. *arXiv:1608.05381*, 2016.

[104] XENON100 collaboration. **Response of the XENON100 Dark Matter Detector to Nuclear Recoil**. *Phys. Rev. D*, **88, 012006**, 2013.

[105] E. Aprile et al. **Simultaneous Measurement of Ionization and Scintillation from Nuclear Recoils in Liquid Xenon as Target for a Dark Matter Experiment**. *Phys. Rev. Lett.*, **97, 081302**, 2006.

[106] M. Horn et al. **Nuclear recoil scintillation and ionisation yields in liquid xenon from ZEPLIN-III data**. *Phys. Lett. B*, **705**:471–476, 2011.

[107] K.-L. Giboni, L. W. Goetzke, R. F. Lang, K. E. Lim, A. J. Melgarejo Fernandez G. Plante, E. Aprile, R. Budnik, B. Choi. **New Measurement of the Scintillation Efficiency of Low-Energy Nuclear Recoils in Liquid Xenon**. *Phys. Rev. C*, **84, 045805**, 2011.

[108] A. Manzur, A. Curioni, L. Kastens, D.N. McKinsey, K. Ni, T. Wongjirad. **Scintillation efficiency and ionization yield of liquid xenon for mono-energetic nuclear recoils down to 4 keV**. *Phys. Rev. C*, **81, 025808**, 2010.

[109] L. Wang, D. Mei. **A Comprehensive Study of Low-Energy Response for Xenon-Based Dark Matter Experiments**. *J. Phys. G: Nucl. Part. Phys.*, **44**, 2016.

[110] F.V. Massoli. *The XENON1T experiment: Monte Carlo background estimation and sensitivity curves study*. PhD thesis, University of Bologna, 2015.

[111] T. Takahashi et al. **Average energy expended per ion pair in liquid xenon**. *Phys. Rev. A*, **12, 1771**, 1975.

[112] B. Leonardo et al. **A Global Analysis of Light and Charge Yields in Liquid Xenon**. *arXiv:1412.4417*, 2015.

[113] XENON10 Collaboration. **First Results from the XENON10 Dark Matter Experiment at the Gran Sasso National Laboratory**. *Phys. Rev. Lett.*, **100, 021303**, 2008.

[114] XENON100 Collaboration. **Dark Matter Results from 225 Live Days of XENON100 Data**. *Phys. Rev. Lett.*, **109, 181301**, 2012.

[115] KamLAND-Zen collaboration. **Search for Majorana Neutrinos near the Inverted Mass Hierarchy Region with KamLAND-Zen**. *Phys. Rev. Lett.*, **117, 082503**, 2016.

[116] XENON100 Collaboration. **The neutron background of the XENON100 dark matter search experiment**. *J. Phys. G: Nucl. Part. Phys.*, **40, 115201**, 2013.

[117] M. Schumann. **XENON100 new results at PATRAS12/Fermilab**, 2012.

[118] S. Yellin. **Finding an Upper Limit in the Presence of Unknown Background**. *Phys. Rev. D*, **66, 032005**, 2002.

[119] XENON100 Collaboration. **Dark Matter Results from 100 Live Days of XENON100 Data**. *Phys. Rev. Lett.*, **107, 131302**, 2011.

[120] S. Yellin. **Some ways of combining optimum interval upper limits**. *arXiv:1105.2928*, 2011.

[121] J.J. Collar. **A Realistic Assessment of the Sensitivity of XENON10 and XENON100 to Light-Mass WIMPs**. *arXiv:1106.0653*, 2011.

[122] Dan Hooper. **Revisiting XENON100's Constraints (and Signals?) For Low-Mass Dark Matter**. *JCAP*, **09(2013)035**, 2013.

[123] XENON1T collaboration. **Physics reach of the XENON1T dark matter experiment**. *JCAP*, **04(2016)027**, 2016.

[124] SuperCDMS collaboration. **Projected Sensitivity of the SuperCDMS SNOLAB experiment**. *Phys. Rev. D*, **95, 082002**, 2017.

[125] J. Billard, E. Figueroa-Feliciano, L. Strigari. **Implication of neutrino backgrounds on the reach of next generation dark matter direct detection experiments**. *Phys. Rev. D*, **89, 023524**, 2014.

Summary

It is hypothesized that 26% of the mass and energy content of the universe is made by Dark Matter. Dark Matter does not emit light, but its gravitational effect on the universe is visible. However, the nature of Dark Matter is not understood.

In this thesis, it is hypothesized that the Dark Matter content of the universe can be explained by the Weakly Interactive Massive Particle (WIMP) hypothesis: a new subatomic particle which participates only in gravitational and weak interactions. While there are several possible ways to detect WIMPs, in this thesis we focused on their direct detection. If WIMPs interact weakly, then there is a minute chance to observe an elastic scattering with a nucleus. Several experiments have been operated in the last 30 years to try to detect the elusive WIMP-nucleus scattering. These experiments are all located in underground laboratories in order to reduce external backgrounds, originating from for example interactions of cosmic rays, and they must be constructed using materials with a very low radioactive contamination.

In this thesis, we focused on the XENON100 experiment located at the underground laboratories of Gran Sasso. This experiment is a xenon-based dual-phase (liquid-gas) Time Projection Chamber (TPC). The peculiarity of this technology is that an interaction of a particle in the TPC produces both scintillation photons and ionization electrons, which are both detected as light signals by PhotoMulTipliers (PMT). Using these two signals the background level can be further reduced. Firstly, the position of the interaction can be reconstructed in three dimensions discriminating between an interaction in the central volume of the TPC and an interaction at the edges of the TPC. The former may be caused by a WIMP interaction and the latter is likely originating from residual radioactivity in the construction materials of the detector. Secondly, the ratio of the ionization to the scintillation signal is different for electron recoils - mostly caused by backgrounds - and nuclear recoils - possibly caused by WIMPs -.

In this thesis we measure the recoil energy of interactions in the target from the scintillation and ionization signals. The recoil energy spectrum is of imminent impor-

tance to determine a WIMP mass once a discovery is established. So far, the XENON experiments have observed no signal of WIMPs, and only exclusion limits have been produced. The data analysis heavily relies on an accurate description of the backgrounds. In this thesis a new analysis is presented that assumes potentially unknown backgrounds to be present in the data. In this way, we obtain a WIMP exclusion limit without background subtraction for WIMP masses between 7 and $1000\,\mathrm{GeV}$ with a minimum of $2.05 \times 10^{-45}\,\mathrm{cm}^2$ at a WIMP mass of $50\,\mathrm{GeV}$. The limit is about a factor 2 worse than the one reported in [3] where backgrounds are assumed to be completely understood and are subtracted.

Then, we tried to clarify some controversial observations at low-mass WIMPs between experiments. The use of the scintillation signal to calculate a WIMP exclusion limit results in a reduced sensitivity towards the low-mass WIMP region, due to relatively large signal threshold which consequently determines a relatively large energy threshold for low-mass WIMPs. Therefore, we developed an analysis which uses only the ionization signal to calculate the recoil energy, resulting in a significant reduction of the energy threshold of the detector and in an enhanced sensitivity for low-mass WIMPs. Using this approach we improved the sensitivity of the XENON100 experiment by several orders of magnitude for WIMP masses below $7\,\mathrm{GeV}$, excluding for example a WIMP-nucleon cross section of $1.4 \times 10^{-41}\,\mathrm{cm}^2$ at a WIMP mass of $6\,\mathrm{GeV}$. Furthermore, we also falsified the low-mass WIMP claim by the DAMA-LIBRA experiment.

To conclude, in this thesis we used the XENON100 data to constrain the parameter space where WIMPs can hide. Hopefully, the XENON1T experiment or the next-generation experiments will give us more hints on the nature of WIMPs and Dark Matter.

Samenvatting

Astronomische waarnemingen laten zien dat 26% van het heelal bestaat uit donkere materie. Donkere materie straalt geen licht uit, maar heeft een zichtbare uitwerking op de zwaartekracht van het heelal. De aard van de donkere materie is echter nog niet duidelijk.

In dit proefschrift wordt verondersteld dat het gedeelte van het heelal dat bestaat uit de donkere materie te verklaren is door de WIMP-hypothese (Engels acroniem voor Weakly Interacting Massive Particle). De WIMP is een nieuw subatomair deeltje dat alleen aan de zwaartekracht en zwakke wisselwerking deelneemt. Alhoewel er vele manieren zijn waarop je een WIMP kunt waarnemen, concentreert dit proefschrift zich op de directe waarneming. Als WIMPs een zwakke wisselwerking hebben, bestaat er een kleine kans op een elastische verstrooiing aan een atoomkern. In de afgelopen dertig jaar zijn er verschillende experimenten uitgevoerd om deze WIMP-nucleusverstrooiing waar te nemen. Voor deze experimenten is de beperking van achergrondruis van groot belang. Daarom vinden ze plaats in ondergrondse laboratoria. Voor de bouw van de experimenten wordt verder ook materiaal gebruikt dat weinig radioactieve stoffen bevat.

Het XENON100-experiment, dat zich in het ondergrondse laboratorium van Gran Sasso bevindt, staat in dit proefschrift centraal. Het experiment is een twee-fase xenon-tijdprojectiekamer (TPC). Het kenmerkende aan deze technologie is dat een interactie van een deeltje zowel scintillatie (fotonen) als ionisatie (vrije elektronen) produceert. Beide signalen worden als lichtflitsen door zeer gevoelige lichtdetectoren - fotomultipliers (PMT's) - geregistreerd. Deze twee signalen kunnen worden gebruikt om achtergrondruis verder te beperken. Ten eerste kan de plaats van de interactie driedimensionaal worden gereconstrueerd. De interactie in het midden van de TPC kan veroorzaakt worden door een WIMP-interactie; de interactie aan de randen van de TPC komt waarschijnlijk voort uit de resterende radioactiviteit die zich in het bouwmateriaal van de XENON100-detector bevindt. Ten tweede zijn de verhoudingen van de signalen

van de ionisatie en de scintillatie-signalen verschillend voor de terugslag van het elektron - die voornamelijk worden veroorzaakt door de achtergrondruis - en de nucleaire terugslag die waarschijnlijk wordt voortgebracht door WIMPs.

In dit proefschrift wordt de energie die in de interactie wordt overgedragen gemeten aan de hand van de twee signalen. Het spectrum van de overgedragen energie is van groot belang om een WIMP te kunnen vaststellen als er een ontdekking is gedaan. Tot op heden hebben de XENON-experimenten geen signalen van WIMPs waargenomen en zijn er alleen limieten gesteld aan de maximale interactiesterkte van WIMPs. De data-analyse is sterk afhankelijk van een nauwkeurige en correcte beschrijving van de achtergrondruis. In dit proefschrift wordt er een nieuwe stelling aangedragen dat er zich onbekende achtergrondruis in de data bevindt. Op deze manier kan er een sterkere limiet worden gesteld aan de maximale interactiesterkte van WIMPs met een massa tussen 7 en 1000 GeV, met een minimum van 2.05×10^{-45} cm^2 voor een WIMP van 50 GeV. De grens neemt hierdoor met factor 2 af ten opzichte van [3] waarin wordt aangenomen dat de achtergrondruis geheel doorgrond en verrekend is.

Vervolgens is er onderzocht of enkele controversiële waarnemingen van WIMPs met een relatief lage massa opgehelderd kunnen worden. Het gebruik van scintillatie-signalen om de maximale interactie-sterkte van een WIMP te berekenen, resulteert in een verminderde gevoeligheid voor WIMPs met een lage massa door de relatief hoge signaaldrempel die derhalve een relatief hoge energiedrempel vormt. Om deze reden hebben wij een analyse ontwikkeld die alleen gebruikmaakt van het door ionisatie geproduceerde signaal om de interactie-energie te berekenen. Dit resulteert in een significante vermindering van de energiedrempel van de detector en een verbetering van de gevoeligheid van het XENON100-experiment voor WIMPs met een massa onder 7 GeV. Hierdoor wordt bijvoorbeeld een WIMP-nucleus-interactiesterkte van 1.4×10^{-41} cm^2 bij een WIMP-massa van 6 GeV uitgesloten. Daarnaast hebben wij kunnen uitsluiten dat de detectie in het DAMA-LIBRA-experiment het gevolg is van WIMPs met een lage massa, zoals eerder werd verondersteld.

Samenvattend wordt in dit proefschrift XENON100-data gebruikt om de parameterruimte waarin de WIMPs zich kunnen bevinden verder af te bakenen. Hopelijk leveren de resultaten van het XENON1T-experiment of experimenten van de volgende generaties meer aanwijzingen op over de aard van WIMPs en donkere materie.

Acknowledgements

If I have managed to complete this PhD thesis, it is because of the support and help from several people. I will try to thank all the people that were with me during this long journey.

Firstly, I would like to thank my promotor Prof. Frank Linde. Frank, thank you for your comments that really improved my dissertation. Thank you also for our useful discussions, that showed me how deeply you can go in the investigation of a subject. I hope to bring this attitude with me during my work life. Then, I would like to thank my co-promotor Prof. Auke-Pieter Colijn. Auke, thank you for reading the thesis from the first moments, giving feedback, helping structuring the manuscript and many other valuable comments. You spent really a lot of time on my thesis, so thank you! I would like to thank also Prof. Patrick Decowski for hiring me and giving me the opportunity to conduct my PhD research in the Dark Matter group. And of course, thank you for all our useful discussions about Dark Matter, and in general for all your support during these years. I would also like to thank all the members of the committee for reading and improving the dissertation and for being part of the doctorate committee.

During my PhD I had the luck to work with very smart people. Among the people of the Dark Matter group, a special thank goes to Dr. Andrew Brown and Dr. Christopher Tunnell. Andrew, thank you very much for helping me in the last period of my thesis giving useful comments and suggestions. I really appreciated it. Chris, thanks a lot for our useful discussions and your guidance during the years of my PhD. I really enjoyed working with you, and I hope to collaborate with you again in the future. I would like also to thank Erik, Matteo, Jelle and Sander for the useful discussions and various help along my PhD path.

During the years of my PhD I met a lot of people which I would like to thank for the various support that they gave me. I would like to thank all the PhD students (and not PhD students) that I met at Nikhef and supported me during these years, in particular Djuaheri, Pierfrancesco, Ed, Emilia, Ivan, Ivano, the young Melini, Stergios, Panos,

Afroditi and sorry if I forget somebody. I would like to thank also all the people that I met here in Amsterdam during these years, in particular Adythia (for beating me at tennis table), Agata, Cristina, Felix, Jenny, Luca from Utrecht and many other people. I would like also to thank my friend Antonio for being first a good tennis partner and last but not least a very good friend during the years of my PhD. I would like to thank Jacopo and Michele for the hospitality at Levantkade, the tennis table, the parties and the marathon (Michele only in this case!).

Then, I would like to thank the city of Porto Recanati which is always in my heart and all my old friends from Porto Recanati. It would be very long to mention them all, but of course it is important to thank Alessandro, Francesco, Marco, Marco, and Simone for being there since a long time. It's very important to thank my family as well, in particular my father, my mother, my brothers and my aunt. Thanks for being here in Amsterdam in the day of my defence, and thank you for your incredible support during these years (the same acknowledgement goes also to all my friends).

Now, I'm close to the end. I would like to thank Fabio and Luca to share with me not only the house but a very long friendship. A friendship that meant a lot to me during the years of the Bachelor and the Master and during the years of the PhD. Thanks a lot for your support during the PhD and I hope that you will also finish the PhD soon!

Finally, but only because you wanted to be the last one, I would like to thank Marcella, my girlfriend. I met you during the last part of my PhD, which was the most stressful period. Nevertheless, you amazingly supported me and the greatest acknowledgement goes to you. I hope to share a long period of my life with you.